Spatial Fringe Analysis Methods and their Application to Holographic Interferometry and Fringe Projection Techniques

THÈSE N^O 4799 (2010)

PAR

Sai Siva GORTHI

EPFL

ÉCOLE POLYTECHNIQUE
FÉDÉRALE DE LAUSANNE

Suisse
2010

Abstract

To date, no fringe analysis technique has the capability to provide simultaneous and direct estimation of the continuous distributions corresponding to the interference phase and its first and second-order derivatives within the framework of a single interferometric configuration. Achieving this task would provide a significant advancement in the field of optical metrology as it allows for the measurement of displacement, strain, and curvature of a deformed object and avoids the necessity of using filtering and unwrapping procedures, multiple analysis techniques, and multiple interferometric configurations. Developing such a spatial fringe analysis method with the added advantage of having less computational complexity would open up avenues for making real-time measurements such as in the study of temporal evolution of deformation and/or strain.

This thesis presents a novel approach based on *piecewise polynomial phase approximation* as an elegant all-in-one solution to the problems mentioned above. This approach has given birth to several advanced fringe analysis methods such as discrete-chirp-Fourier transform method, high-order instantaneous moments method, and cubic-phase function method. Significant advancements brought in the field by these methods are made evident by both theoretical analysis (simulation results) and by experimental demonstrations such as the measurement of displacement, strain and curvature in *digital holographic interferometry* and the measurement of 3D shape, temporal evolution of deformation and/or strain in *fringe projection techniques*.

Keywords: Optical metrology, Holography interferometry, Fringe projection techniques, Fringe analysis, Filtering, Phase unwrapping, Strain estimation, Time evolution studies

Résumé

De nos jours, aucune technique d'analyse de frange n'est capable de donner une estimation simultanée et directe des distributions continues correspondantes à la phase d'interférence et ses première et deuxième dérivées dans le cadre d'une configuration interférométrique individuelle. Atteindre cet objectif permettrait une avancée majeure dans le domaine de la métrologie optique en tant que mesure de déplacements, des déformations et des courbures d'un objet déformé, et permettrait d'éviter l'utilisation de procédures telles que le filtrage et le déroulement des phases, des techniques basées sur des analyses multiples ou encore sur celles basées sur des configurations multiples en interférométrie. Développer une telle méthode d'analyse spatiale de frange avec l'avantage d'avoir une complexité computationnelle faible, ouvrirait une voie prometteuse pour les mesures en temps réel, comme dans l'étude de l'évolution temporelle des déplacements et/ou des déformations.

Cette thèse présente une nouvelle approche qui se base sur la *piecewise polynomial phase approximation*, qui est une solution élégante et unique à tous les problèmes décrits précédemment. Cette approche a donné naissance à plusieurs méthodes d'analyse de frange avancées, comme par exemple les méthodes faisant appel à la *discrete-chirp-Fourier transform*, au *high-order instantaneous moments* et à la *cubic-phase function*. Les avancées significatives dans le domaine qui découlent de ces méthodes sont mises en évidence par l'analyse théorique (résultats de la simulation) et par les démonstrations expérimentales comme celles des mesures de déplacements, de déformations et de courbure par l'interférométrie holographique digitale et les mesures de forme en 3D, l'évolution temporelle de déplacements et/ou des déformations par les techniques de projection de frange.

Mots clés: Métrologie optique, interférométrie, technique de projection de frange, analyse de frange, estimation de la déformation, études de l'évolution en fonction du temps.

Acknowledgements

I would like to express my deep gratitude to Prof. Pramod Rastogi for giving me the opportunity to do PhD under his esteemed guidance. His encouragement played a crucial role in accomplishing the objectives that we had set for this thesis. My sincere thanks are due to him for providing me freedom and opportunities to expand my research horizons. I am also grateful to his family members Mrs. Vandana Rastogi, Swalp, Swati and David for their moral support.

I take this opportunity to thank Prof. Ian Smith and Dr. Pierino Lestuzzi for their support during my stay at IMAC. I would also like to thank all my colleges at IMAC for the friendly atmosphere that they created and for the wonderful time that we have spent together for over the last four years. I acknowledge the excellent skills of Patrice Gallay, mechanical technician, for his great help in designing the experimental systems in the laboratory. My thanks also go to Sylvian Demierre for his cheerful assistance while ordering equipments for the laboratory work. I am indebted to my colleague Rajshekhar Gannavarpu for both the technical and general discussions, and which I must say have been meaningful, relishing and motivational.

I am grateful to my former teachers: Mr. Sravana Kumar of Palakollu, Prof. M. Suryaprakash Rao and Mr. Venu Gopal from Adams Engineering College; and Prof. R.M. Vasu from Indian Institute of Science (IISc) Bangalore. I am ever indebted to Dr. L. Kameswara Rao of Instrumentation Department, IISc, for his exceptional guidance during my Master's studies. If it was not for his training, I could have never imagined myself to become a researcher.

My thanks are also due to Dr. Abhijit Patil for having stood out as a role model for me by making his PhD thesis work exceptionally well. His accomplishments have served as a source of inspiration for me. I am also thankful to Dr. Chandrasekhar Seelamantula

Published Articles

The work presented in various chapters of this thesis has appeared in peer-reviewed journals during the last two years or has been submitted for publication.

(1) S. S. Gorthi and P. Rastogi, "Piecewise polynomial phase approximation approach for the analysis of reconstructed interference fields in digital holographic interferometry", **Journal of Optics A: Pure and Applied Optics** 11(065405),1-6 (2009).

(2) S. S. Gorthi and P. Rastogi, "Discrete chirp Fourier transform based analysis of reconstructed interference fields in digital holographic interferometry", **Journal of Modern Optics** 56(12), 1317–1322 (2009).

(3) S. S. Gorthi and P. Rastogi, "Estimation of phase derivatives using discrete chirp-Fourier-transform based method", **Optics Letters** 34, 2396–2398 (2009).

(4) S. S. Gorthi and P. Rastogi, "Analysis of reconstructed interference fields in digital holographic interferometry using the polynomial phase transform", **Measurement Science and Technology** 20(075307), (2009).

(5) S. S. Gorthi and P. Rastogi, "Windowed high-order ambiguity function method for fringe analysis", **Review of Scientific Instruments** 80(7), 073109 (2009).

(6) S. S. Gorthi and P. Rastogi, "Improved high-order ambiguity-function method for the estimation of phase from interferometric fringes", **Optics Letters** 34(17), 2575–2577 (2009).

(7) S. S. Gorthi, G. Rajshekhar and P. Rastogi, "Investigations to realize a computationally efficient implementation of the high-order instantaneous moments based fringe analysis method", **Optical Engineering**, 49(065802), 1-4 (2010).

(8) S. S. Gorthi, G. Rajshekhar, and P. Rastogi, "Strain estimation in digital holographic interferometry using piecewise polynomial phase approximation based method", **Optics Express** 18(2), 560–565 (2010).

(9) S. S. Gorthi and P. Rastogi, "Phase estimation in digital holographic interferometry using cubic phase function based method", **Journal of Modern Optics**, 57(7), 595-600 (2010).

(10) S. S. Gorthi and P. Rastogi, "Simultaneous measurement of displacement, strain and curvature in digital holographic interferometry using high-order instantaneous moments", **Optics Express** 17(20), 784–791 (2009).

(11) S. S. Gorthi and P. Rastogi, "Numerical analysis of fringe patterns recorded in holographic interferometry using high-order ambiguity function", **Journal of Modern Optics** 56(8), 949–954 (2009).

(12) S.S. Gorthi and P. Rastogi, "Fringe projection techniques: whither we are?", **Optics and Lasers in Engineering** 48(2), 133–140 (2010).

(13) S.S. Gorthi, G. Rajshekhar and P. Rastogi, "Three dimensional shape measurement using high-order instantaneous moments based fringe projection method", **Optics and Laser Technology**, 43(1), 40-44 (2011).

Table of Contents

List of Figures

List of Tables

Chapter 1

Spatial Fringe Analysis Methods

1.1 Introduction

Optical measurement techniques such as interferometry and fringe projection profilometry have become indispensable tools in many areas of science and engineering. The whole-field, non-contact characteristics and highly accurate measurement capability are among the potential features of these techniques. These techniques encode the information on the measurand in the phase of a two-dimensional fringe pattern. The accuracy of measurements carried out by these optical techniques is thus strongly dependent on the accuracy with which the underlying phase distribution of the recorded fringe patterns is estimated. During the last three decades several fringe analysis methods (such as those based on Fourier transform [1], wavelet transform [2], windowed Fourier transform [3], regularized phase tracking [4] and many more based on phase-shifting [5]) have been developed to accomplish this task.

Most of the fringe analysis methods (both temporal and spatial methods) produces a *noisy wrapped phase map* as the end output. Thus in order to clean (remove the noise from) the noisy wrapped phase maps, several filtering algorithms such as Fourier transform based filter [6], sine and cosine transformation based filter [7], adaptive filter [8], iterative anisotropic sine/cosine average filter [9], and local histogram-data-orientated filter [10] have been proposed. Further, to obtain a continuous phase distribution several unwrapping algorithms, such as Goldstein's unwrapping algorithm [11], region growing phase unwrapping [12], local histogram based phase unwrapping [13], improved noise immune phase unwrapping [14], regularized phase tracking [15], flood fill [16], multilevel quality guided phase unwrapping algorithm [17], have also been developed. It is not an easy task for a non-expert in the field to choose the best combination of these algorithms (fringe analysis, filtering and phase unwrapping) for obtaining satisfactory final measurement results, in view of the requirements on the accuracy and time of computation. *It is thus highly desirable to have a fringe analysis method that can provide an accurate and direct estimation of the continuous phase distribution without the necessity of using additional filtering and unwrapping algorithms.*

In addition, in certain applications such as in non-destructive testing, it is the derivative of the phase map that is of primary interest (rather than phase), as it provides the

information on the strain distribution. Few analysis methods [18, 20, 53] have been proposed in literature to address this issue, but they again require postprocessing operations such as filtering and/or unwrapping. An alternative approach for measuring strain is to use a specific interferometric configuration such as shearography and moiré based, which provides directly the displacement derivative fringes [21–27]. In this case, one can use any fringe analysis method, that is commonly used for phase estimation, to obtain information about strain. But if one would like to get information corresponding to say, displacement also, one has to change the interferometric configuration and make another measurement. For example the interferometric configurations proposed in [28–32] allow the measurement of curvature alone. This procedure is having an associated disadvantage that it is not possible to get all the information in a single measurement. In reality it is difficult to unload the object and identically reload it multiple times. Thus efforts have been made to measure all the three quantities of interest (displacement, strain, and curvature) in a single digital holographic interferometric configuration [33–38] by using digital shearing approach. However, to have good sensitivity, the amount of shift that has to be introduced is more, and it results in the loss of resolution and some times gross errors due to the rapid variations in the phase or its derivative. Moreover, this procedure further requires the use of cumbersome and error prone filtering and phase unwrapping procedures. *It is thus highly desirable to have an analysis method that can provide an accurate and direct estimation of the continuous distributions of phase and its first- and second- order derivatives from only one fringe pattern recorded in a single interferometric configuration.*

Finally, in dynamic applications where studying the transient phenomenon in real-time is of vital importance, only one image (fringe pattern) in each state of the object can be recorded. For processing such recorded fringe patterns, several methods such as windowed Fourier transform [39] have been proposed. But as their computational time is more, results cannot be visualized in real-time. The processing of the captured stack of images is thus performed in off-line. To have the analysis done in real-time and visualize the deformation or strain at the same time, the analysis algorithm must be computationally very efficient; in addition to not requiring any filtering and phase unwrapping procedures. It is worth noting that if the analysis algorithm directly provides continuous phase distribution after processing each slice of the recorded fringe movie, there will be no necessity for employing a sophisticated three-dimensional phase unwrapping algorithm. *Thus in dynamic applications it is highly desirable to have an analysis method that can provide results in a computationally efficient manner from only one fringe pattern.*

This thesis addresses all the above issues by providing potential solutions and demonstrating their practical applicability in holographic interferometry and fringe projection techniques. Section 1.2. presents the state-of-the art on each of the aforementioned domains. Section 1.3. summarizes the research objectives of the thesis followed by a brief description on the structure of the thesis in Section 1.4.

1.2 State-of-the Art

1.2.1 Spatial Fringe Analysis Methods for the Estimation of Phase

Fringe analysis has been an active area of interest in optical metrology. Last two decades have seen much activity in the development of new analysis techniques, which can provide an estimation of the underlying phase distribution of the fringe pattern in an automated manner. The most simple and widely used technique for the spatial analysis of carrier fringe patterns is the Fourier transform method, proposed by Takeda et al. [1]. Fourier transform is well suited for the analysis of a signal composed of sinusoidal components as long as the frequency, amplitude and phase of each sinusoidal component are slowly varying or space-invariant. However, in practice the parameters of most of the interferometric fringe patterns that we deal with are space-varying. These patterns represent non-stationary signals and analysis of such signals by simple Fourier transform may provide results with non-negligible errors. During recent years, this realization has motivated researchers to propose the use of advanced spatial analysis methods (for accurate phase estimation) such as those based on regularized phase tracking [4], windowed Fourier transform or Gabor transform [3,40], dilating Gabor transform [41], 1D and 2D wavelet transforms [2,42–49] and Wigner-Ville distribution with a smoothing Gaussian kernel [50].

It has been shown that, instead of using a global Fourier transform, the use of windowed Fourier transform or Gabor transform provides more accurate results [3,40]. But the width of the window is fixed in conventional Gabor transform analyses. It is well known that as the width of the window decreases the space resolution increases and the frequency resolution decreases. Hence for low frequency components it is advisable to use a longer window, while for high frequency components the use of a shorter window is more suitable. Since Gabor transform has invariable resolution in the space or frequency domain, it shows limitations when applied to the analysis of non-stationary signals.

On the other hand, dilating Gabor transform is introduced by using a changeable window of Gaussian function in a conventional Gabor transform. The dilating Gabor transform analysis is shown to provide more accurate results than that obtained by the Fourier transform and Gabor transform analysis methods [41]. The one dimensional continuous wavelet transform technique has also been applied for the phase estimation from a single fringe pattern. Compared to other techniques, this method has the advantage that it needs neither the phase unwrapping nor the introduction of the carrier. However, its success depends on the *a priori* knowledge of well-determined boundary conditions. In addition, it fails in the neighborhood of the null phase gradients or along pixel paths that have slow phase variations. Although Paul wavelet based algorithm [45] is shown to successfully determine the phase distribution from a single image, it requires the introduction of carrier fringes. The use of two-dimensional continuous fan wavelet transform has also been proposed and it has been shown that it not only outperforms its one-dimensional counterpart based method but is also more immune to noise [48].

Federico and Kaufmann have proposed the use of Wigner-Ville distribution with a smoothing Gaussian kernel for fringe pattern analysis that does not require the use of phase

unwrapping and is shown to provide more accurate results than the methods based on continuous wavelet transform [50]. However, this method too requires *a priori* knowledge of the boundary conditions and the sign of the first derivative of the phase over a set of points that permit the integration of the gradients. In addition, the results of this method are highly sensitive to speckle noise which necessitates pre-processing of patterns to reduce noise before the analysis. Above all, it is a well known fact in signal processing that conventional power spectrum analysis is ineffective for analyzing this kind of signals and even the Wigner-Ville distribution fails to process polynomial phase signals having a polynomial of degree more than 2. On the other hand, for the analysis of similar non-stationary signals encountered in communication systems, methods based on High-order ambiguity function have received considerable attention over all the methods mentioned in the preceding paragraphs [51].

It is clear that there is an imperative need for the development of a fringe analysis method that provides, from a single frame, an accurate and direct estimation of the unwrapped phase distribution. To meet this demand this thesis introduces several promising fringe analysis techniques based largely on discrete-chirp Fourier transform, high-order ambiguity function and cubic phase function.

1.2.2 Fringe Analysis Methods for the Direct Estimation of Phase Derivative

In application areas like non-destructive testing (NDT), experimental mechanics, reliability analysis etc. measurement of the derivative of the interference phase is of primary importance. This is because, for an object subjected to loading in certain optical interferometric set-ups such as holography, the information about the object deformation is encoded in the interference phase whereas the first order derivative of phase provides information about the strain distribution.

Special efforts have been devoted for the development of analysis methods having the potential to produce direct estimation of the phase derivative distribution; because the obvious approach of phase estimation and subsequent differentiation is error-prone [52,53].

Gopalakrishna Bhat proposed a method for the estimation of phase derivative using Fourier transform [18]; However, it inherits the basic limitations imposed by the global nature of the transform as in the case of phase estimation. Sciammarella et al. proposed a Wigner-Ville distribution based method [54] for phase derivative estimation but the method's performance is limited by the interference terms that arises due to the nature of the distribution. Qian Kemao proposed a Windowed Fourier transform based method [19,55] for direct phase derivative estimation but its accuracy depends on the size of the window selected, on top of being computationally expensive.

1.2.3 Methods for the Estimation of Strain, Curvature and/or Twist

Determining first and second-order derivatives of the interference phase is of profound importance in NDT with applications in reliability assessment, quality control, safety mon-

itoring, material characterization etc. as they provide information about the slope/strain and curvature/twist pertaining to a deformed object. Last two decades have witnessed an ever increasing interest in the measurement of slopes and curvatures as evident from the development of various optical interferometric techniques [21–32], processing algorithms [18–20, 55], and their widespread applications [56–64]. Interferometric techniques employed for this task include shearography, digital holographic interferometry (DHI), and various interferometers based on Moiré. Being able to directly provide fringe maps corresponding to the slope information can be ascribed to be among the main reason behind the prominence of shearography in NDT.

In the light of some of the unique advantages associated with DHI (such as allowing digital recording of holograms and facilitating numerical reconstruction), efforts have been made during recent years [33–38] to extend its use to the measurement of slopes and curvatures. The fact that digital holography directly provides the complex amplitude of the reconstructed object wave field, and that digital shifting and multiplying with a conjugated version of a complex amplitude equivalently differentiates its phase have been exploited in the above methods. However, as the first and second-order derivatives calculated in this manner are observed to be contaminated with severe noise (in addition to being wrapped), different filtering schemes such as those based on average filter, sine/cosine transform and short-time Fourier transform have been proposed [37, 38]. However, the iterative filtering operations are computationally demanding and need to be carefully implemented so as not to smear dense fringes. This thesis introduces an elegant solution for accurate and simultaneous determination of phase and its derivatives by approaching the problem all together from a different perspective.

1.3 Thesis Objectives

The first objective of this thesis is to develop new analysis methods that caters to the following needs:

- providing accurate estimation of the interference phase from a *single record* of the interference pattern

- not requiring any pre *filtering* operation

- not requiring the use of a complicated *2D phase unwrapping* algorithm

- providing the direct estimation of the *phase derivative* without the necessity of employing a different analysis tool

- providing *second-order derivatives* of the phase (curvature and twist information) without employing a different optical interferometric configuration

- providing the results in *highly computationally efficient* manner - thereby allowing to perform real-time measurements

5

The second objective of the thesis is to demonstrate the potential utility of the above developed analysis methods in performing the following measurements:

- *out-of-plane displacement* measurement using both classical and digital holographic interferometry techniques

- *whole-field strain distribution* measurement using digital holographic interferometry

- simultaneous measurement of *displacement, strain and curvature* using digital holographic interferometry

- *Three-dimensional shape* measurement using fringe projection techniques

- *real-time deformation* monitoring using fringe projection techniques

- *real-time whole-field strain evolution* monitoring using fringe projection techniques

1.4 Outline of the Thesis

The outline of the thesis is as follows:

Chapter 2 introduces the piecewise polynomial phase approximation approach and proposes maximum likelihood estimation based realization.

Chapter 3 presents discrete-chirp Fourier transform based method that performs as good as maximum likelihood estimation method and at the same time provides a faster implementation scheme. Overlapping windowing concept and the direct estimation of phase derivative using discrete-chirp Fourier transform are also presented.

Chapter 4 introduces an elegant method based on high-order ambiguity function method that allow approximation of the data, in each piece, as a polynomial of order greater than two and in a computationally efficient manner. Few variants of the basic method (such as windowed high-order ambiguity function method, improved high-order ambiguity function method) applied to fringe analysis are also presented. Investigations carried out to realize a computationally efficient implementation of this method are also presented. The final version of this method named as high-order instantaneous moments method standouts to be an unsurpassable method both in accuracy and computational efficiency at medium levels of signal-to-noise ratios.

Chapter 5 presents a robust cubic phase function method having the capability to provide accurate results even at very high-levels of noise. It outperforms many of its competitors at low signal-to-noise ratios. Estimation of phase derivative using cubic phase function is also presented along with the simulation and experimental results.

Chapter 6 shows the application of these new analysis methods in holographic interferometry for carrying out several important measurements. Specifically, out-of-plane displacement measurements in both classical and digital holographic interferometry with the high-order instantaneous moments method are presented. Simultaneous measurement of displacement, strain, and curvature in digital holographic interferometry are also demonstrated.

Chapter 7 presents the application of these new analysis methods in fringe projection techniques for measuring 3D shape of objects, for real-time monitoring of the deformation, and for the study of whole-field strain evolution.

Chapter 8 summarizes the contributions reported in this thesis. Scope for the future work is also presented.

Chapter 2

Maximum Likelihood Estimation Method

2.1 Introduction

This chapter introduces a new approach which is conceived to have the potential of giving birth to several fringe analysis methods which would have the capability to address the issues mentioned in the previous chapter. The details of the new approach are introduced here within the framework of digital holographic interferometry (DHI). Its applicability to other optical techniques such as classical holographic interferometry and fringe projection techniques is dealt in later chapters. A detailed description of the measurement procedure involved with DHI is presented in chapter 6. This chapter thus provides only a brief overview of the formation of reconstructed interference fields in DHI, followed by a description of the new approach and its realization using maximum likelihood estimation.

2.2 Piecewise Polynomial Phase Approximation Approach

In phase-based techniques in optical metrology, the information on the measurand is encoded in the phase of the recorded interferogram or the fringe pattern. Unlike in classical holographic interferometry, digital holography is known to directly provide the complex amplitude of the reconstructed object wave field. Therefore, usually no separate analysis method is employed for estimating phase in digital holographic interferometry [65]. It is simply calculated using the arctan function from the reconstructed interference field. However, phase calculated in this manner is always wrapped and often noisy, making it mandatory to employ filtering and 2-D phase unwrapping procedures as mentioned in the introduction chapter. These reasons motivated researchers to develop different strategies or new analysis techniques [40, 66–68].

On the other hand, in many technological applications such as radar, sonar and communications, commonly used signals are often modeled as one-dimensional polynomial

9

phase signals (PPS). During the last two decades, many tools have been developed for the analysis of PPS [51]. Unfortunately they are neither directly useful nor have they been applied for phase estimation in digital holographic interferometry. The approach presented in this thesis has opened up avenues for the application of signal processing tools (which were originally developed for the analysis of a particular class of 1-D time signals) to the phase estimation problem in digital holographic interferometry.

The fringe analysis methods that are developed based on this approach possess the feature of providing directly an accurate estimation of the continuous phase distribution from a single record of the interference field. It involves dividing each row of the reconstructed interference field into few non-overlapping segments and modeling the data in each segment as a finite-order polynomial phase signal with constant (or slowly varying) amplitude, embedded in additive complex white Gaussian noise (ACWGN). This approach is accordingly named as piecewise polynomial phase approximation approach (PPPAA/**P3A2**).

In order to compute the polynomial phase coefficients, maximum likelihood estimation (MLE) algorithm can be used as is explained in the next section.

Numerical reconstruction of a digital hologram by Fresnel transform results in the direct recovery of the object wave field, which, in general, is represented as [65]:

$$\Gamma(x, y) = a(x, y) \exp[j\phi(x, y)] \tag{2.1}$$

where $a(x, y)$ is the amplitude and $\phi(x, y)$ is the estimated phase of the object wave field. In DHI two digital holograms, one for each state of the object, are recorded (before and after deformation). These holograms are reconstructed separately. From the resulting complex amplitudes, $\Gamma_1(x, y)$ and $\Gamma_2(x, y)$, the interference phase can be calculated by forming the *reconstructed interference field* as:

$$
\begin{aligned}
A(x, y) &= \Gamma_2(x, y) \times \Gamma_1^*(x, y) \\
&= a_1(x, y) a_2(x, y) \exp\left\{ j\left[\phi_2(x, y) - \phi_1(x, y)\right] \right\} \\
&= b(x, y) \exp\left[j\Delta\phi(x, y) \right]
\end{aligned}
\tag{2.2}
$$

where $\phi_1(x, y)$ and $\phi_2(x, y)$ are respectively the phases of the object waves before and after deformation. The complex amplitude of the reconstructed interference field in real-world conditions can be expressed as:

$$A(x, y) = A_0(x, y) + \eta(x, y) \tag{2.3}$$

where $A_0(x, y)$ represents the complex amplitude of the *noise-free interference field* and η represents the noise term. Our aim is to estimate the phase of the actual interference field in equation(2.3) using P3A2. We propose to divide the reconstructed interference field signal into N_w number of non-overlapping segments along each row. Without loss of generality, the problem of interference phase estimation can then be considered as the phase estimation of the following segment of the 1-D signal:

$$A_{yi} = b_{yi} \exp(j\phi_{yi}) + \eta_{yi} \tag{2.4}$$

where y, i and η represent the index of the row, the index of the segment and the ACWGN with zero-mean and σ^2 variance, respectively; y, i take values from 1 to N and 1 to N_w, respectively. For a given row, A_i is defined as:

$$A_i = \{A(x)\} \quad \text{for } [(i-1) \times N_s + 1] \leq x \leq i \times N_s \tag{2.5}$$

where $N_s = N/N_w$. Since the interference phase to be estimated in DHI is, in general, a continuous function of the spatial coordinates, it can be approximated arbitrarily closely, in accordance to Weierstras approximation theorem [69], by a polynomial of a sufficiently high order. Normally, in presence of rapid variations in phase, the order of the polynomial required for accurate representation of $\phi(x)$ will be high. However, by conceiving the phase as a piecewise polynomial signal, modeling the phase *locally* even by a second-order polynomial can provide quite accurate results. In what follows we represent each segment of the interference field with a second order PPS. Thus the signal to be analyzed can be represented in a simplified form as:

$$g(x) = b(x) \exp\left[j(a_0 + a_1 x + a_2 x^2)\right] + \eta(x) \tag{2.6}$$

The problem of estimating the phase from the noisy observation in equation(2.3), thus, basically amounts to estimating the parameters like polynomial coefficients $\{a_0, a_1, a_2\}$ for each segment. In this chapter we use the maximum likelihood (ML) estimation, an optimal parametric estimation method, for estimating the polynomial coefficients.

2.3 Maximum Likelihood Estimation

The following are the ML estimators [70] for the parameters of the signal in equation(2.6):

$$(\hat{a}_1, \hat{a}_2) = \arg\max_{a_1, a_2} \left| \sum_{x=1}^{N_s} g(x) \exp\left[-j(a_1 x + a_2 x^2)\right] \right| \tag{2.7}$$

$$\hat{a}_0 = angle\left\{ \sum_{x=1}^{N_s} g(x) \exp\left[-j(\hat{a}_1 x + \hat{a}_2 x^2)\right] \right\} \tag{2.8}$$

$$\hat{b}(x) = Re\left\{ g(x) \exp\left[-j(\hat{a}_0 + \hat{a}_1 x + \hat{a}_2 x^2)\right] \right\} \tag{2.9}$$

where $\hat{a}_0, \hat{a}_1, \hat{a}_2$, and $\hat{b}$ are the ML estimates of a_0, a_1, a_2 and b respectively.

Equation(2.7) indicates that one has to perform a 2-D maximization for implementing the ML algorithm. The estimation is performed in two steps; first, a coarse search, followed by a fine search. Coarse search is done by performing an exhaustive 2-D grid search to find the vicinity of the global maximum. Once this vicinity is found, Nelder-Mead simplex search optimization algorithm [71] is used for refinement. Note that for the 2-D grid search, a_1 is varied from 0 to 2π in steps proportional to $1/N_s$, and a_2 is varied
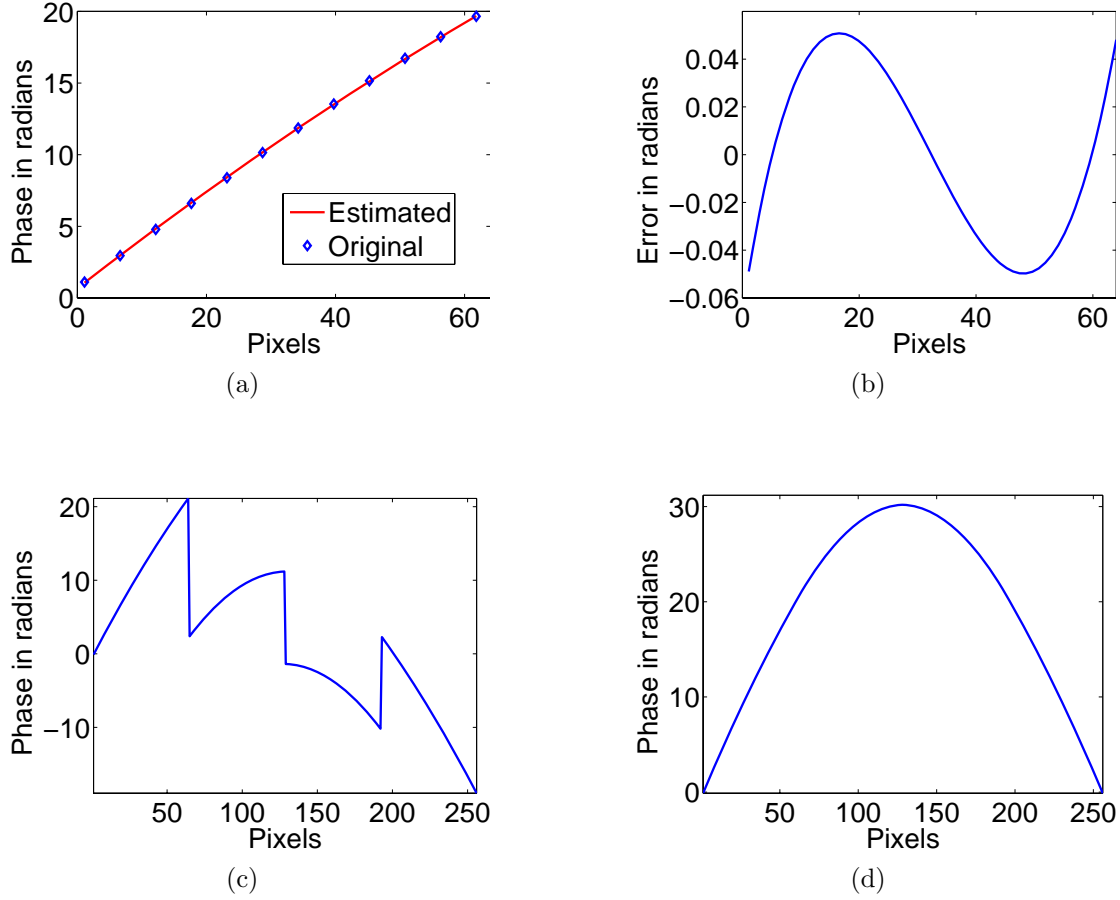
Fig. 2.1: (a) Estimated phase over a segment using MLE at *SNR* of $30\,dB$ (b) Error in estimation (c) Estimated phase of the whole signal when $\hat{a}_0$ is calculated using equation(2.8)($Nw = 4$), (d) Estimated phase of the same signal when $\hat{a}_0$ is calculated using equation(2.10).

from 0 to $+2\pi/N_s$ in steps proportional to $1/N_s^2$. The fine search algorithm is built using the 'FMINSEARCH' function of MATLAB, which performs multi-dimensional unconstrained nonlinear minimization by implementing Nelder-Mead simplex search algorithm.

Estimating the coefficient $\hat{a}_0$ using equation(2.8) involves the use of *angle* function, which will result in wrapping, causing discontinuities at the boundaries of each segment. This can be avoided if $\hat{a}_0$ is calculated, for all segments except for the first one, in the following manner:

$$\hat{a}_{0(i+1)} = \hat{a}_{0i} + \hat{a}_{1i}N_s + \hat{a}_{2i}N_s^2 \tag{2.10}$$

This modified estimation directly provides the unwrapped phase distribution over the entire row, not just over the individual segments. Figure 2.1a shows the phase estimated over a segment using the ML estimation procedure; error in estimation is shown in figure 2.1b. If $\hat{a}_0$ is calculated over all segments using equation(2.8), the resulting estimated phase of the whole signal is shown in figure 2.1c. Figure 2.1d shows the phase of the same

signal obtained by calculating $\hat{a}_0$ using equation(2.10). Although the phase estimated along individual rows is unwrapped, to obtain a continuous 2-D phase distribution one additional operation of the type needed to weave all the rows to fall in line one after the other is required. We refer to this operation as phase stitching; this task is as easy as 1-D unwrapping of an ideal wrapped phase map. More detailed discussion on this is included in chapter 4.

2.4 Simulation and Experimental Results

In order to test the ability of the proposed analysis methods, various fringe patterns having arbitrary phase distributions are simulated (using MATLAB)throughout the thesis. Figure 2.2a shows the simulated fringe pattern of dimensions 256×256 pixels at an *SNR* of 30 *dB*. The nature of the phase distribution simulated in this case corresponds to the slope distribution of a centrally loaded square plate clamped along its edges. Phase estimated along the middle row using P3A2 with MLE is shown in figure 2.2b. In these simulations the signal is divided into four segments ($N_w = 4$). The estimation procedure is repeated for all rows. Figure 2.2c shows the 3-D plot of the estimated phase distribution over the entire image.

Regularized phase tracking (RPT) of Servin [67] and windowed Fourier ridge (WFR) of Kemao [40,68] are among the well noted methods in literature which can provide accurate phase estimation from the exponential phase fields. In [72] Kemao et al. have provided an elegant comparative analysis of five effective wrapped phase filtering techniques which included RPT and WFR. Thus here we compare the results of the P3A2 with WFR. Figure 2.3 shows 3-D mesh plots of error distributions when continuous phase distribution corresponding to the pattern shown in figure 2.2a is estimated with both the methods. Root mean square errors (RMSE) produced by WFR method (window size of 5×5 pixels) and P3A2 are given by 0.1325 and 0.0367, respectively.

Please note that the analysis of interferograms by fitting specific types of polynomials (such as Zernike polynomials) or combinations of them is an old idea and many reports have appeared [73–77]. But it has met with limited success as it was possible only to address specific problems since, in general, representing experimentally obtained data by polynomials is a difficult mathematical problem. Nevertheless, the approach presented in this thesis overcomes this limitation by approximating the interference phase with a piecewise polynomial signal model and adopts several efficient parametric estimation techniques for its realization. To illustrate the potential implication of the piecewise polynomial phase approximation, the fringe pattern shown in figure 2.4a is analyzed as explained in the preceding paragraphs and the estimated phase distribution is shown in figure 2.4b. Error in phase estimation is shown in figure 2.4c. Even more accurate results can be obtained if over each segment instead of second-order polynomial approximation, fourth-order approximation is used. figure 2.4d shows the error in estimation if such a method is used (more details on the practical methods for realizing a higher-order polynomial approximation are presented in later chapters). This example confirms the ability of piecewise polynomial approximation in accurately representing even complex phase

(a)

(b)

(c)
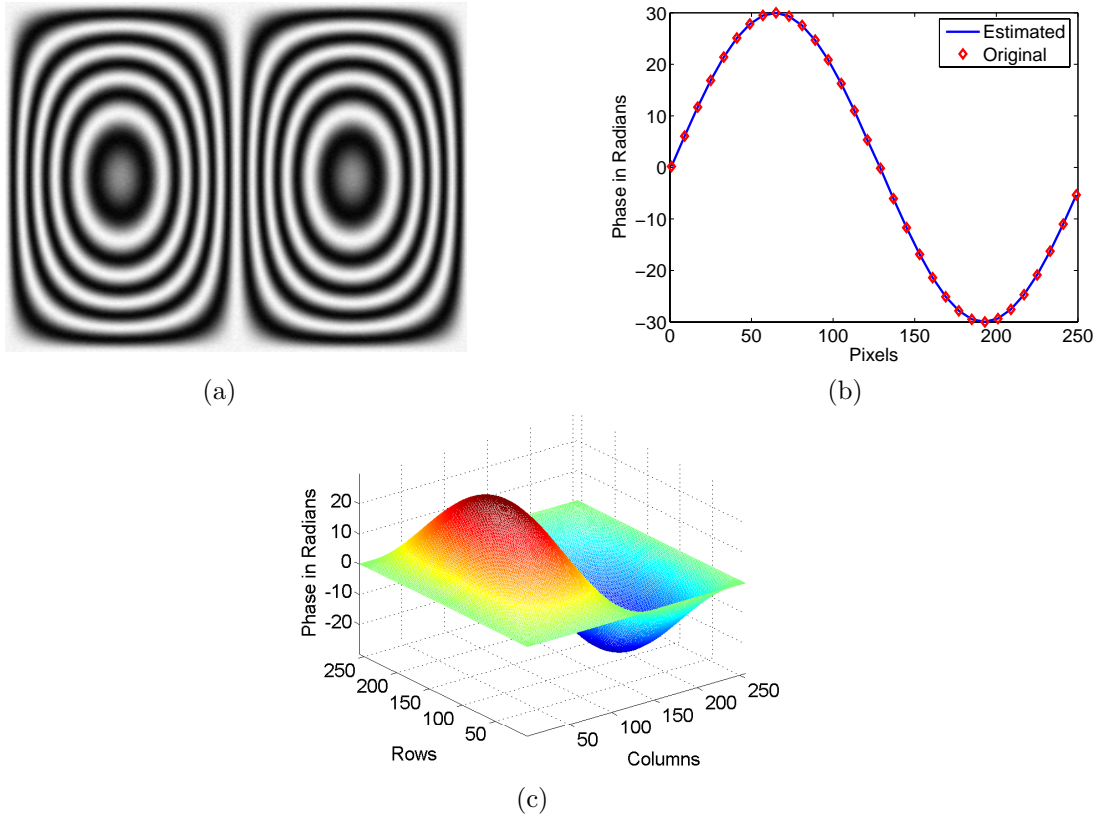
Fig. 2.2: (a) Simulated fringe pattern at SNR of $30\,dB$ (b) Phase estimated along the middle row using P3A2 ($N_w = 4$) (c) 3-D plot of the estimated phase over the whole image

(a)

(b)
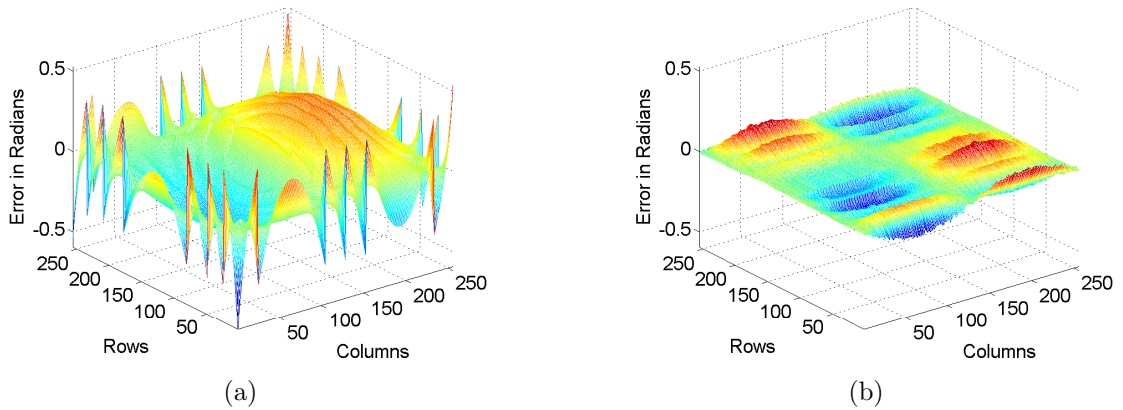
Fig. 2.3: Error plots when continuous phase distribution of figure 2.2a is estimated with (a) WFR method (b) P3A2-MLE method ($N_w = 4$).
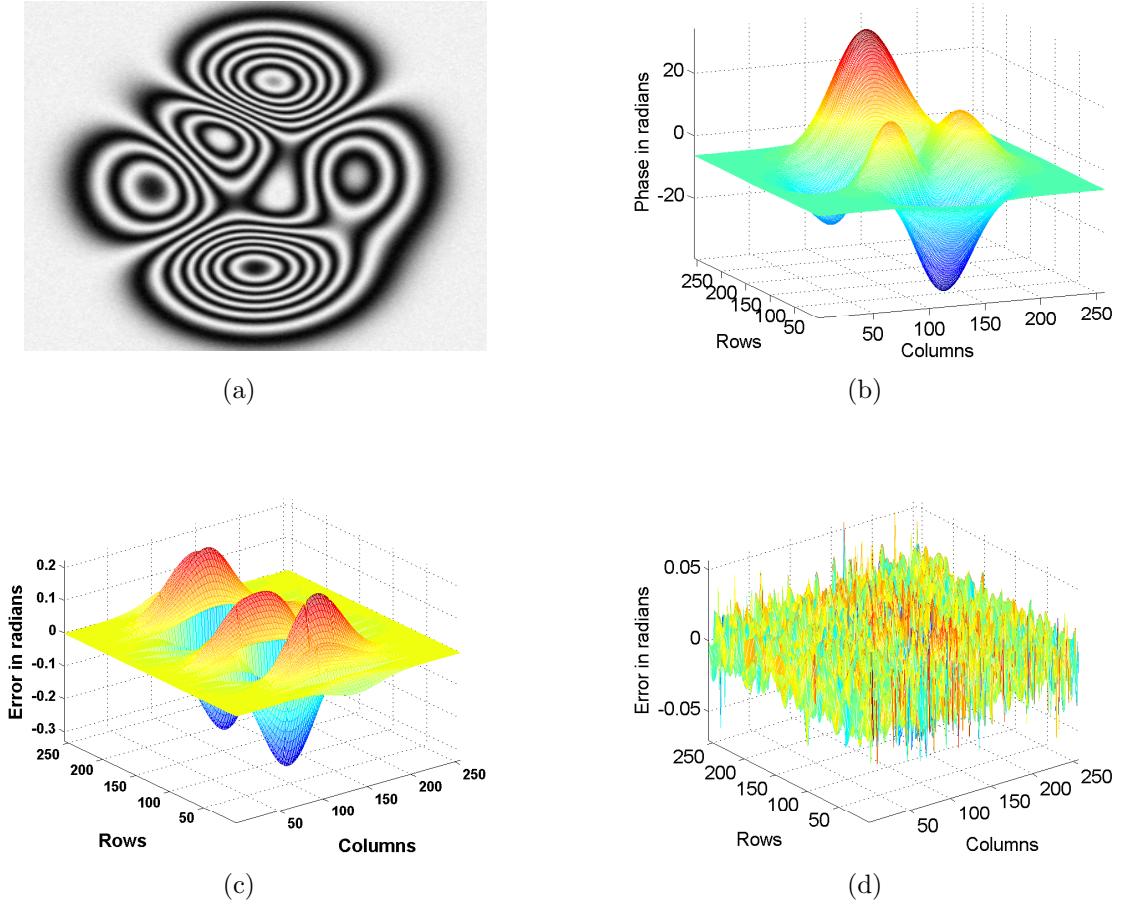
Fig. 2.4: (a) Simulated fringe pattern using the peaks function in MATLAB ($SNR = 30\ dB$, 256×256), (b) 3D mesh plot of the estimated phase distribution using MLE method (c) Error in phase estimation with MLE method (d) Error in phase estimation when fourth-order approximation is used

distributions (not limiting to polynomial signals) and thereby extending its applicability to wide range of applications. It is worth noting that if a typical row/column (say middle column) of the pattern shown in figure 2.4a is to be represented with a polynomial phase signal, polynomial of order 20 or higher is needed to achieve the accuracy shown in figure 2.4d. Practically, it is not feasible to estimate those many coefficients by MLE or, for that matter, by any other method. On the other hand, dividing the signal into eight segments, and approximating the data in each segment with a second or fourth-order polynomial signal has enabled to accurately estimate the phase. The choice of the number of segments and the order of polynomial approximation in each segment depends on the type of experiment and the functional complexity of the measured deformation. Nevertheless, dividing each row/column into eight or sixteen segments and modeling data in each segment with a fourth or second order polynomial phase signal is found to provide accurate results for many distributions, which can be considered as a general guideline.

The experimental results shown in figure 2.5 substantiate the effectiveness of the P3A2-MLE method for the phase estimation in DHI. On the other hand, the phase map obtained

(a)

(b)
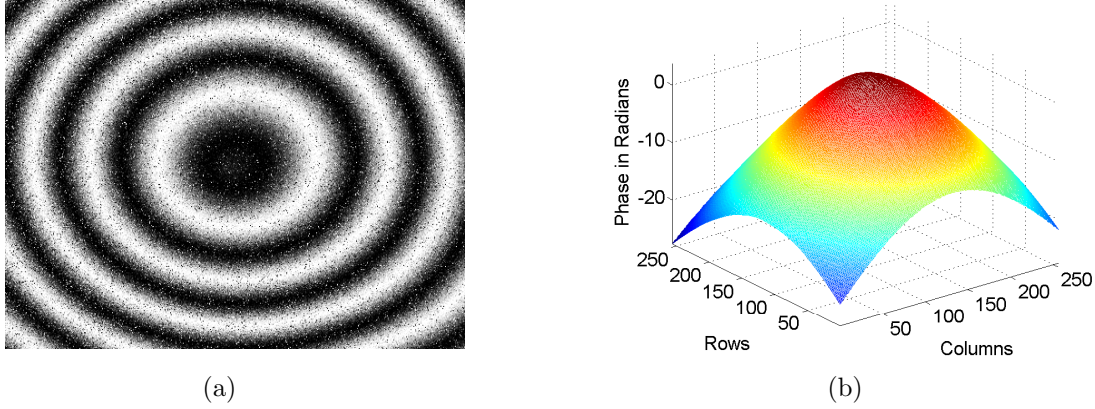
Fig. 2.5: (a) Experimentally recorded fringe pattern in DHI for a circularly clamped object with central loading (b) Phase calculated using the P3A2-MLE method ($N_w = 4$).

using the arctan function from the reconstructed interference field is shown in figure 2.6a. For the sake of comparison, the wrapped phase map generated from the continuous phase distribution obtained using the P3A2 method ($N_w = 4$) is shown in figure 2.6b. A notable improvement in the quality of the phase pattern obtained using the P3A2 method can be observed. Please note that these fringes appear to be elliptical rather than circular due to the non-unity aspect ratio of the displayed images. In order to verify the significance of the piecewise approximation, the wrapped phase map generated from the phase estimated with $N_w = 1$ (i.e., the entire row is considered as one segment) is shown in figure 2.6c. It is evident that the estimated phase in this case is having considerable deviation from the actual phase, as the actual phase can be accurately approximated with only 4th or higher order polynomial. This confirms that the P3A2 method, i.e., with $N_w > 1$, promises to provide accurate estimation even with the lower order polynomial approximation.

2.5   Discussion

An interesting feature of P3A2 is that its performance is unaffected by the absence or the presence of spatial carrier (be it local or global). In applications where the spatial frequency varies strongly within a single image, it only results in the increased value of the coefficient a_1 (See equation(2.6)). Therefore, this approach can effectively handle the situation without any modifications. But if there are rapid variations in the rate of phase modulation, taking more number of windows (i.e., segmenting the signal into higher number of pieces) will allow P3A2 to accurately approximate, within each segment, the phase of the signal with a polynomial of second-order. The price to be paid for this could be additional computational cost, depending on the method used for the estimation of polynomial coefficients. Nevertheless, by developing an adaptive windowing concept that will on-the-fly determine the window length depending on the rate of variations in phase of the data, will allow the presented approach to make an optimum trade-off between the computational time and the accuracy of estimation in an automated manner.
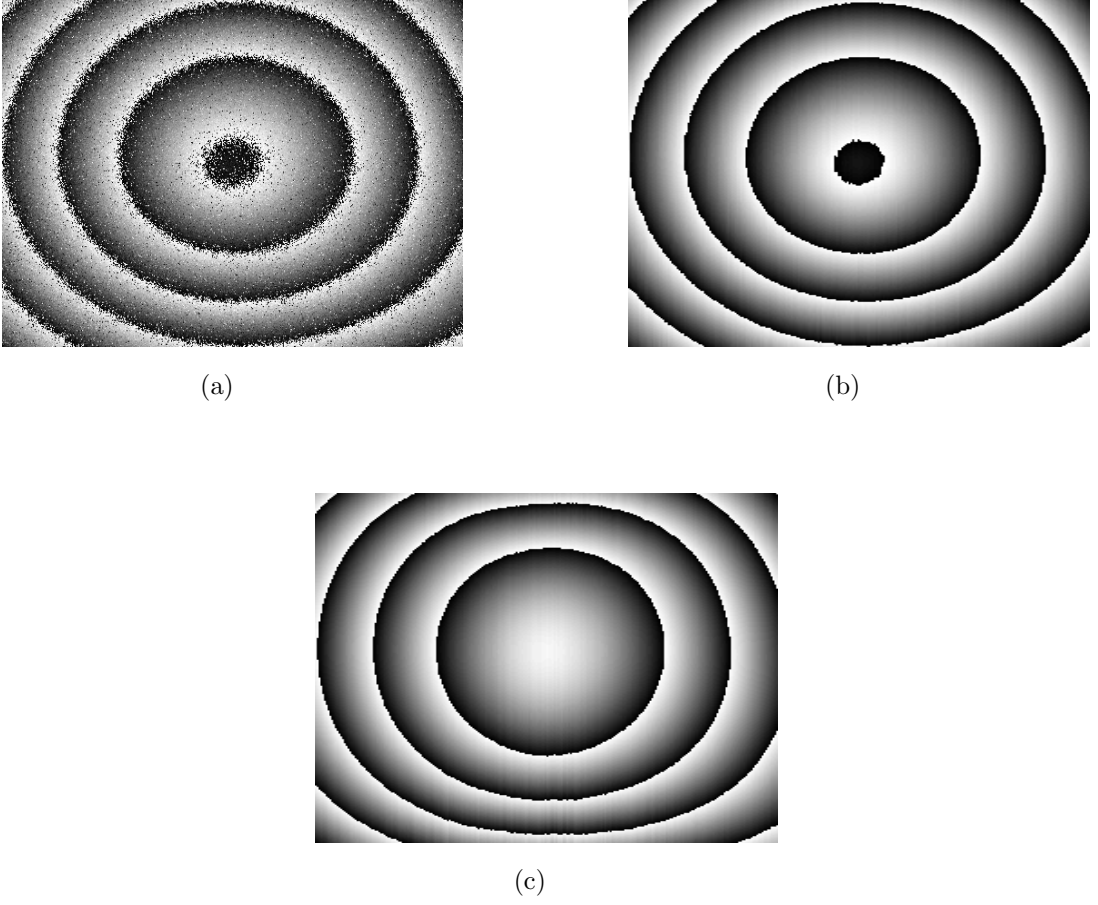
Fig. 2.6: (a) Phase calculated directly using the arctan function (b) Wrapped phase generated from figure 2.5b for the sake of comparison (c) Wrapped phase map generated from the estimated phase with $N_w = 1$.

2.6 Conclusions

This chapter presented a new approach for phase estimation in digital holographic interferometry. Simulation and experimental results have validated the ability of the proposed P3A2 coupled with the MLE in providing an accurate estimation of the continuous phase from a single record of the reconstructed interference field. Further, it neither requires 2D phase unwrapping nor any filtering steps. In this chapter the implementation of P3A2 is realized with MLE; but in principle any other parametric PPS analysis method can be adapted to expedite the processing as will be shown in later chapters. Thus, the proposed approach has paved the way to adapt well-established PPS analysis tools available in the signal processing literature for the phase estimation in digital holographic interferometry.

Chapter 3

Discrete-chirp Fourier Transform Method

3.1   Introduction

Previous chapter has introduced the piecewise polynomial phase approximation approach (P3A2) for the analysis of reconstructed interference fields in DHI. The evaluation of polynomial coefficients was performed using maximum likelihood estimation method. However, as MLE involves an exhaustive two-dimensional grid search, it could be computationally very demanding especially if the dimensions of the image are higher (512×512 or so). In this chapter we introduce discrete chirp-Fourier transform (DCFT) based estimation, which is shown to provide exactly the same results as that obtained by MLE in terms of estimation accuracy but at a reduced computational time. In addition, direct estimation of phase derivative using the DCFT method is also presented in this chapter.

3.2   Discrete Chirp-Fourier Transform Method

In the last chapter we have seen that, in P3A2 the problem of phase estimation from the reconstructed interference field (equation 2.3) has been recast into the problem of estimating the parameters of equation 2.6 which is rewritten here for convenience:

$$g(x) = b(x) \exp\left[j(a_0 + a_1 x + a_2 x^2)\right] + \eta(x) \tag{3.1}$$

Here we use DCFT for the estimation of the parameters $\{a_1, a_2\}$.

DCFT of $g(x)$ is defined as [78, 79]:

$$G(k_1, k_2) = \sum_{x=0}^{N_s-1} g(x) \exp\left[-j(\alpha_{k_1} x + \beta_{k_2} x^2)\right] \tag{3.2}$$

$$G(k_1, k_2) = FFT\{g(x) \exp\left[-j\beta_{k_2} x^2\right]\} \tag{3.3}$$

$$\text{where} \quad \begin{aligned} \alpha_{k_1} &= \frac{2\pi}{N_s} k_1 & 0 \le k_1 \le N_s - 1 \\ \beta_{k_2} &= \frac{2\pi}{N_s^2} k_2 & -N_s + 1 \le k_2 \le N_s - 1 \end{aligned}$$

k_1 and k_2 are integers whose limits are specified as above, $N_s = N/N_w$ represents the number of samples present in a segment and $FFT\{\cdot\}$ denotes the fast Fourier transform operation.

Just as the location of a peak in the Fourier transform domain of a single-tone provides information on a signal's frequency, the location of a peak in the DCFT-domain of a chirp-signal provides, simultaneously, information on the constant frequency and the chirp rate. In other words, the magnitude of DCFT achieves maximum when the values of α_{k_1} and β_{k_2} match respectively with the actual coefficients a_1 and a_2 of the signal's phase. Making use of this property of the DCFT, figure 3.1 illustrates its application in determining the polynomial phase coefficients.

Figure 3.1a shows the plot of the real part of the signal $g(x)$ (see equation 3.1) synthesized with the polynomial coefficients $\{a_0 = -0.4702, a_1 = 0.9791, a_2 = -0.0076\}$, amplitude $b(x) = 1$, and SNR of 20 dB. Magnitude of DCFT for $g(x)$ is shown in figure 3.1b; a dominant peak is clearly visible. Corresponding values of α_{k_1} and β_{k_2} at which the peak is appearing are 0.9817 and -0.0077 respectively.

Computation of DCFT using fast Fourier transform (FFT) implementation (see equation 3.3) makes it computationally very efficient. For the signal shown above computing DCFT took approximately 0.32 seconds. However, given the limited resolution (i.e., the step size used while generating α_{k_1} and β_{k_2}), the estimates are gross and need further refinement. One option for obtaining accurate estimates is to increase the resolution (by decreasing the step size) while computing DCFT at the cost of more computational time. Instead, for further refinement we propose to use these gross estimates obtained using DCFT as the initial guess for the Nealder-Mead simplex search optimization [71].

The following set of equations summarizes the implementation details of the proposed method:

$$(\hat{a}_{1g}, \hat{a}_{2g}) = \arg \max_{\alpha_{k_1}, \beta_{k_2}} |G(k_1, k_2)| \tag{3.4}$$

$$(\hat{a}_1, \hat{a}_2) = Optimization(g, [\hat{a}_{1g}, \hat{a}_{2g}]) \tag{3.5}$$

$$\hat{a}_0 = angle \left\{ \sum_{x=1}^{N_s} g(x) \exp\left[-j(\hat{a}_1 x + \hat{a}_2 x^2)\right] \right\} \tag{3.6}$$

where $(\hat{a}_{1g}, \hat{a}_{2g})$ are the gross estimates of (a_1, a_2) obtained using DCFT and $(\hat{a}_1, \hat{a}_2)$ are the refined/accurate estimates obtained after optimization.

The optimization routine is built using the 'FMINSEARCH' function in the MATLAB, which performs multi-dimensional unconstrained nonlinear minimization by implementing Nelder-Mead simplex search algorithm. For the ease of implementation following lines

(a)

(b)

(c)

(d)
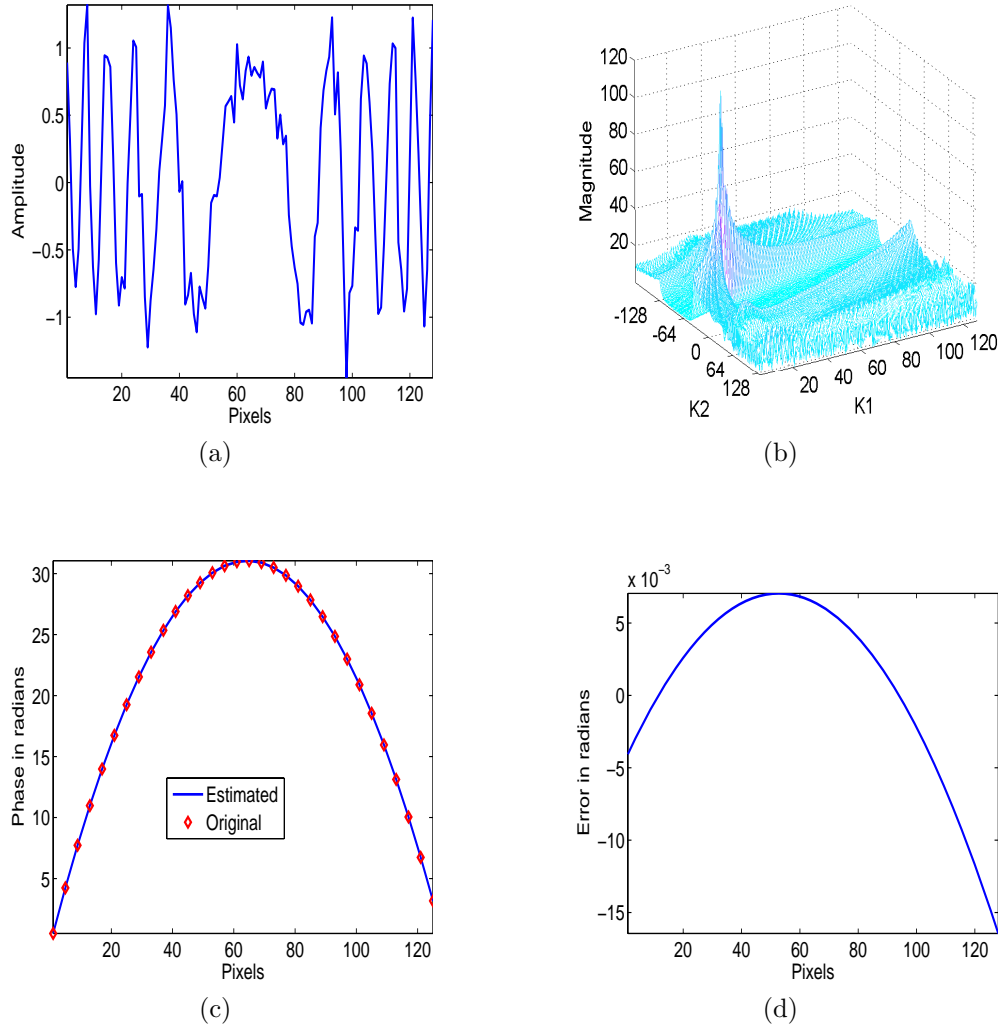
Fig. 3.1: (a) Plot of the real part of $g(x)$, (b) Magnitude of DCFT of $g(x)$, (c) Estimated phase of $g(x)$ after optimization, (d) Error in phase estimation.

of code are provided:

$opt = optimset('fminsearch');$

$opt = optimset(opt,' Display',' off',' TolX', sqrt(eps),' MaxIter', 200);$

$\hat{a} = fminsearch(@(\hat{a}) \ chirpopt(\hat{a}, g), [\hat{a}_{1g}, \hat{a}_{2g}], opt);$

where $\hat{a} = [\hat{a}_1, \hat{a}_2]$ and *chirpopt* is the objective function that we define for optimization.

Phase estimated by this process for the signal shown in figure 3.1a at SNR of 20 dB is shown in figure 3.1c. Error in phase estimation is shown in figure 3.1d. It is worth noting that the magnitude of error in estimation by this method primarily depends on the local slope of the signal's phase being approximated. Since the signal is approximated with

21

a second-order polynomial phase signal, error will be more in regions where the slope is high. However, either by increasing the order of polynomial approximation, or by using the same order approximation but in a piecewise manner, error in estimation can be reduced considerably. In this chapter we consider the latter approach.

When analyzing the reconstructed interference fields, phase within each window of the segmented signal can be calculated by constructing the polynomial with the estimated co-efficients $\hat{a}_0, \hat{a}_1, \hat{a}_2$, obtained by following the aforementioned procedure, in the respective windows. However, for the reasons explained in the last chapter, $\hat{a}_0$ is calculated, except for the first window, using equation 2.10.

Though the error of the estimated phase remains quite small within each window, its tendency to change rapidly towards the edges of the windows causes the overall error (of the whole row) to increase. This is shown in figure 3.2a. This type of error can be significantly reduced by taking a fifty-percent overlapping windowing scheme (see figure 3.2a). Since, as illustrated in figure 3.2a, the error changes rapidly near the boundaries of the windows, we can use a scheme of two layers of windows to create fifty-percent overlapping between them. The reconstructed data from these two layers is considered in a way to keep the error to the minimum (see figure 3.2b).

3.3   Simulation and Experimental Results

Figure 3.3a shows the simulated fringe pattern (corresponding to the simulated reconstructed interference field) at SNR of 10 dB. Figure 3.3b shows the estimated phase profile along a column using DCFT followed by optimization in each of the eight windows of the segmented signal. The estimation procedure is repeated for all columns. Figure 3.3c shows the 3-D plot of the estimated phase distribution over the entire image. Error in the phase estimation using the DCFT based analysis method is shown in figure 3.3d.

Results shown in figure 3.3 are obtained using overlapping windowing concept and by dividing the signal along each column into eight segments ($N_w = 8$). Depending on the
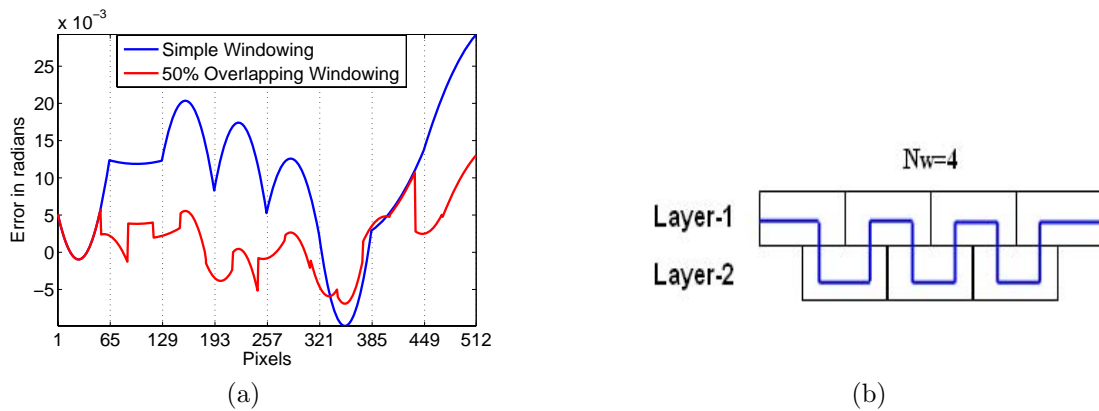
Fig. 3.2: (a) Comparison of error plots when simple windowing and overlapping windowing concepts are used, (b) Fifty-percent overlapping windowing scheme.

(a)

(b)

(c)

(d)
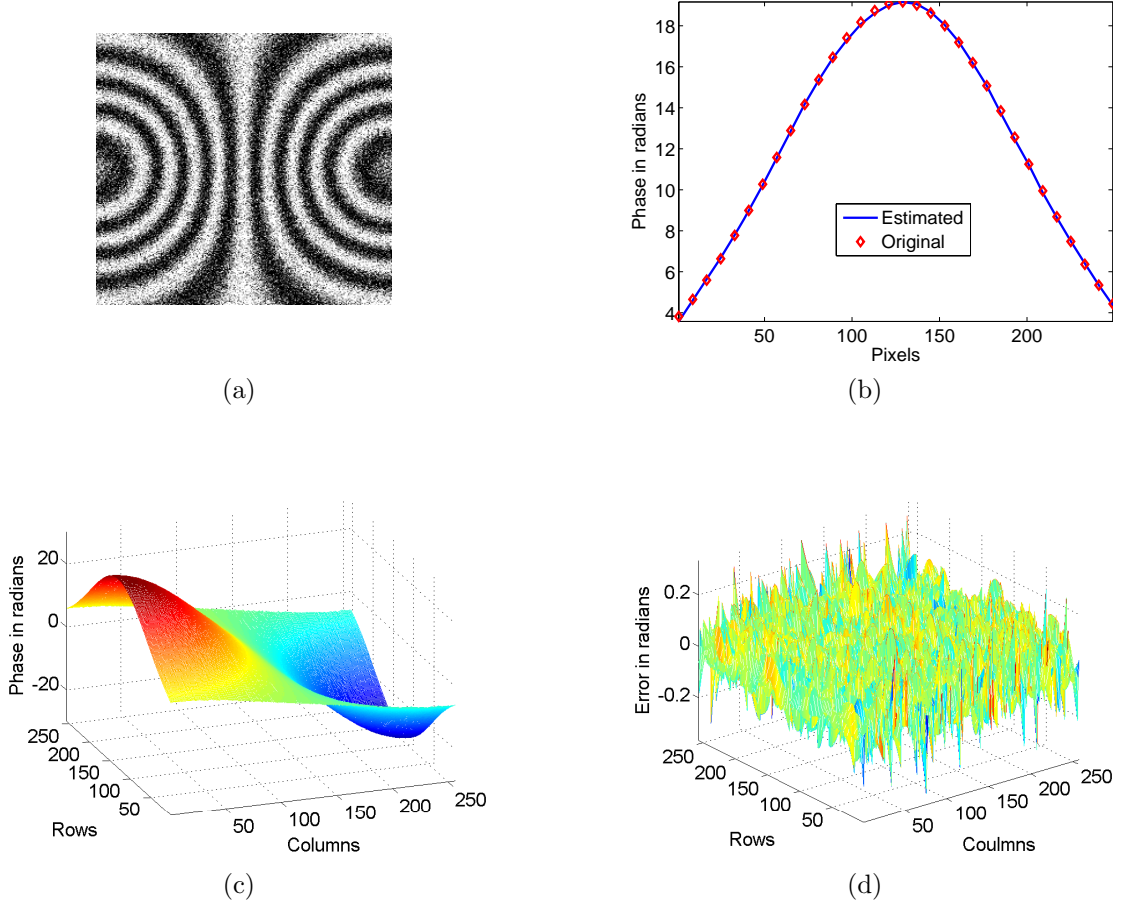
Fig. 3.3: (a) Simulated fringe pattern at SNR of 10 dB (256×256) (b) Plot of estimated phase along 64th column using the DCFT method (c) 3-D plot of the estimated phase along all the columns (d) Error in phase estimation.

requirements on the accuracy of measurement and the computation time, one can chose appropriate value for N_w. Table 3.1 indicates the impact of increasing N_w on the accuracy and on the computational time in analyzing the pattern shown in figure 3.3a at SNR of 30 dB. Table 3.2 evaluates the performance of the DCFT method at different SNR levels for both simple windowing and overlapping windowing concepts. It is evident that the DCFT method provides quite accurate results when applied with overlapping windowing concept.

Figure 3.4 shows the application of DCFT for phase estimation from a reconstructed interference field obtained in a digital holographic interferometry experiment. Figure 3.4a shows the real part of the reconstructed interference field corresponding to the central loading of a circularly clamped object. Figure 3.4b shows the 3-D mesh plot of the estimated phase distribution using the DCFT method. On the other hand, phase map calculated directly from the reconstructed interference field using the arctan function is shown in figure 3.5a. For the purpose of illustration, wrapped phase map generated from the continuous phase distribution estimated by the DCFT method is also shown in figure 3.5b. Though the same results can also be obtained using the maximum likeli-

23

<div align="center">(a)   (b)</div>

Fig. 3.4: (a) Recorded fringe pattern corresponding to the central loading of a circularly clamped object in a DHI experiment, (b) 3-D plot of the estimated phase distribution using the DCFT method.

<div align="center">(a)   (b)</div>
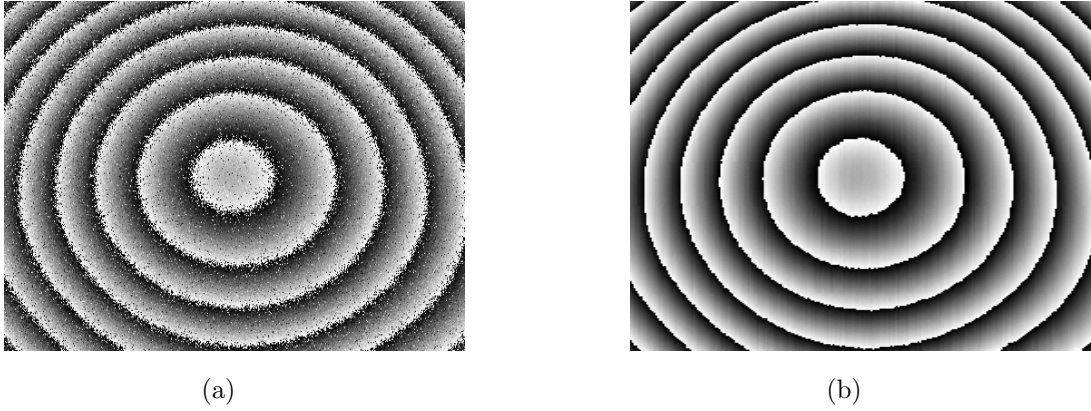
Fig. 3.5: (a) Phase calculated using the arctan function directly from the reconstructed interference filed, (b) Wrapped phase map generated from the estimated continuous phase in figure 3.4b for the purpose of illustration.

<div align="center">Tab. 3.1: Impact of increasing number of windows</div>

N_w	RMSE values	Time in minutes
4	0.0344	0.5635
8	0.0121	0.8833
16	0.0085	1.7397

Tab. 3.2: Performance evaluation of DCFT method ($N_w = 8$) with respect to noise in estimating phase

Type of windowing	RMSE values at SNR of			Computational time (in minutes)
	10 dB	20 dB	30dB	
Simple	0.2949	0.1031	0.0598	0.4727
Overlapping	**0.0597**	**0.0216**	**0.0121**	0.8833

Tab. 3.3: Comparison of computation times between the MLE and the DCFT methods

Image dimensions	Computation time in minutes	
	MLE-P3A2	DCFT
256 x 256	2.65	**0.88**
512 x 512	30.00	**2.53**

hood estimation based method presented in the previous chapter, it is worth emphasizing that DCFT is computationally relatively very efficient, especially as the image dimension increases. This is evident from the computational times listed in Table 3.3.

3.4 Phase Derivative Estimation using DCFT

From equation 3.1, it is evident that the derivative of interference phase can be estimated by calculating the phase derivative over each segment of the signal according to the following equation:

$$\frac{\partial \phi}{\partial x} = a_1 + 2a_2 x \qquad (3.7)$$

Therefore, by simply estimating the polynomial coefficients $\hat{a}_1, \hat{a}_2$ for all segments using DCFT as explained in the previous sections, one can obtain an accurate and direct estimation of the phase derivative distribution. Note that, phase derivative thus computed does not require any phase stitching as it does not contain $\hat{a}_0$ term.

If the measurement application also requires the estimation of the phase distribution, it can be obtained by integrating the phase derivative map. Phase estimated in this manner, however, requires an offset correction as the constant of integration is unknown. The offset can be calculated by employing the same estimation procedure along a representative column/row. This way of estimating phase directly provides the unwrapped phase distribution. Note that this is an alternative approach to compute phase distribution. However, it is found that, phase obtained in this manner (i.e., by integrating the derivative map) is a bit less accurate than that is calculated as explained in the previous section.

Figure 3.6a shows a simulated fringe pattern (corresponding to a simulated reconstructed interference field) of dimensions 256×256 at an *SNR* of 10 *dB*. Figures 3.6b, 3.6c show
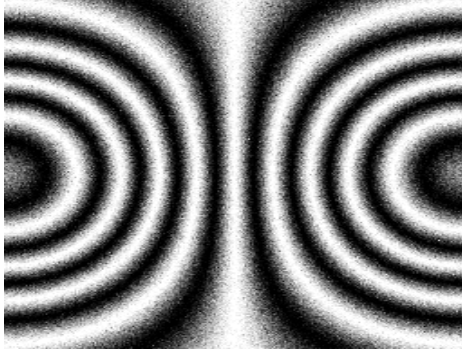
(a)

(b)
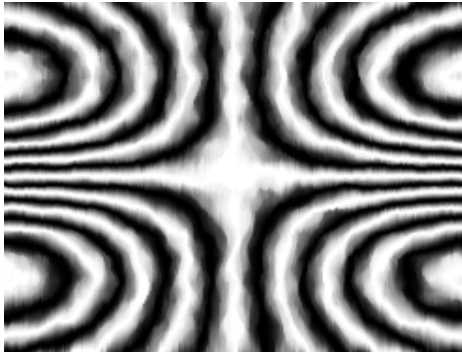
(c)
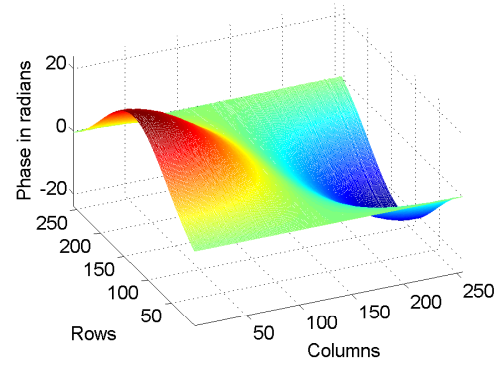
(d)
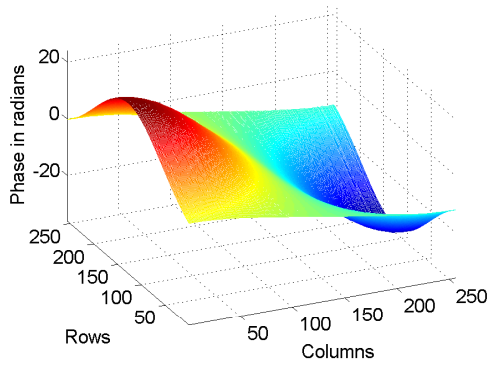
(e)
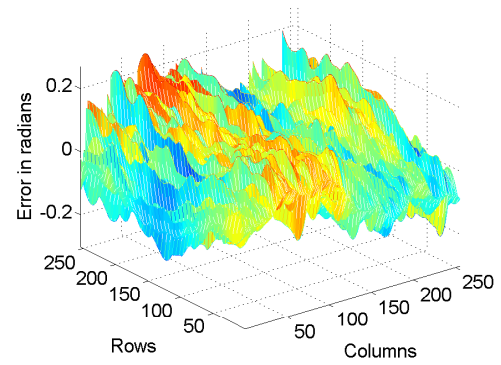
(f)

Fig. 3.6: (a) Simulated fringe pattern at SNR of 10 *dB* (256 × 256), (b) Estimated phase derivative along y-axis using the DCFT method, (c) cosine of the phase derivative along y-axis (for illustration), (d) Phase obtained by the numerical integration of the derivative map shown in b, (e) Phase map after offset correction, (f) Error in phase estimation.

Tab. 3.4: Performance evaluation of DCFT method ($N_w = 8$) with respect to noise in estimating phase derivative

SNR	RMSE values	
	Simple Windowing	Overlapping Windowing
30 dB	0.0027	**0.0017**
20 dB	0.0041	**0.0028**
10 dB	0.0109	**0.0076**

respectively the estimated phase derivative map along y-axis obtained using the proposed DCFT method, and its *cosine* generated for the purpose of illustration. Phase distribution calculated using the numerical integration of the derivative map is shown in figure 3.6d. It needs an offset correction as the phase distribution of all columns starts from zero. Figure 3.6e shows the resulting phase after offset correction. Error in phase estimation is shown in figure 3.6f.

Results shown in figure 3.6 are obtained using overlapping windowing concept and by dividing each column of the pattern into eight segments ($N_w = 8$). Table 3.4 shows the performance of the DCFT method in estimating the phase derivative of the fringe distribution shown in figure 3.6a at different SNR levels for both simple windowing and overlapping windowing concepts. It is evident that the DCFT method provides quite accurate estimation of the phase derivative when applied with overlapping windowing concept.

Experimental results shown in figure 3.7 substantiate the effectiveness of the DCFT method for the estimation of phase and its derivative in DHI.

3.5 Conclusions

This chapter presented discrete chirp Fourier transform based method for the analysis of reconstructed interference fields in DHI. It is found to be an effective analysis method for providing an accurate and direct estimation of the unwrapped phase distribution. Simulation and experimental results confirm that the DCFT method with overlapping windowing scheme provides accurate results in a computationally efficient way when compared to maximum likelihood estimation. Procedure for the direct estimation of the first-order derivative of the interference phase distribution using DCFT is also presented.
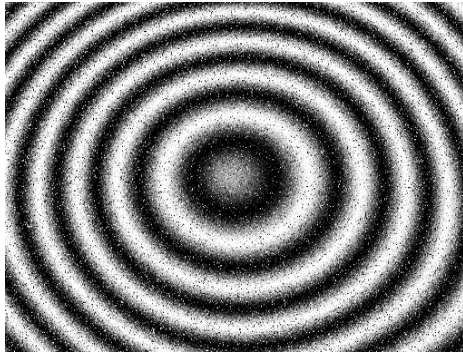
(a)

(b)
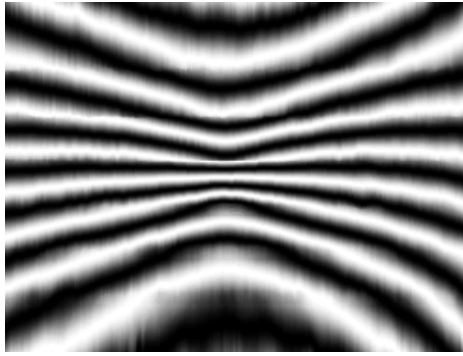
(c)
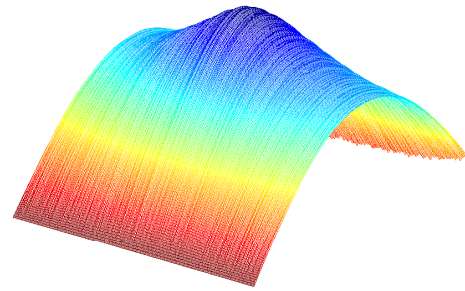
(d)
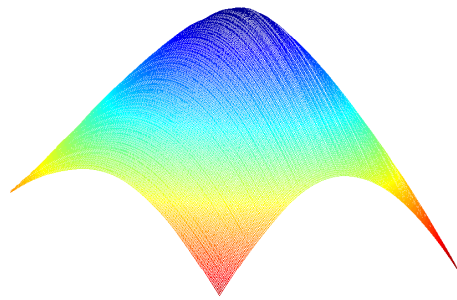
(e)
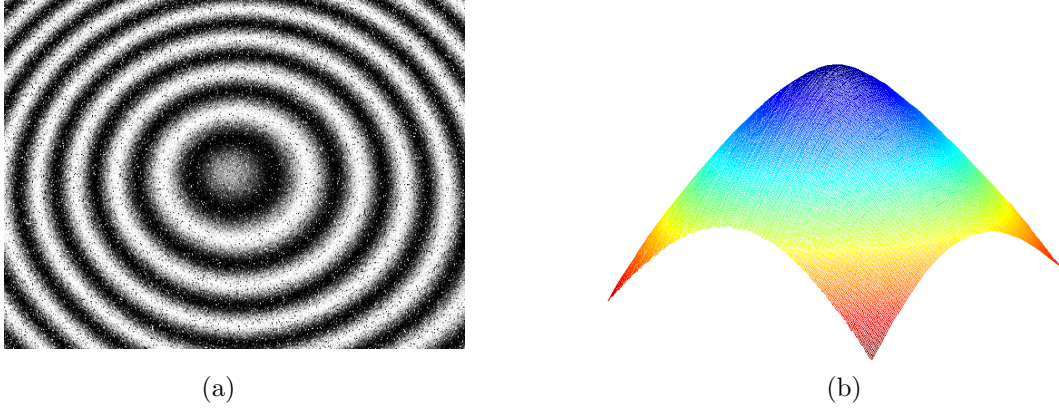
Fig. 3.7: (a) Recorded fringe pattern corresponding to the central loading of a circularly clamped object in a DHI experiment, (b) Phase derivative map along y-axis, (c) cosine of the phase derivative along y-axis (for illustration), (d) Phase distribution obtained by numerical integration of the derivative map shown in b, (e) Phase map after offset correction.

Chapter 4

High-order Instantaneous Moments Method

4.1 Introduction

In the last two chapters, we have seen that P3A2 is an elegant approach for accurate and direct estimation of the unwrapped distributions corresponding to both phase and its first-order derivative. However, with both MLE and DCFT methods we can approximate the data with up to a second-order polynomial phase signal only. In this chapter we introduce high-order ambiguity function (HAF) based method with which it is possible to make higher order approximations (for example with a fourth-order polynomial phase signal), that too in a computationally efficient manner. This feature of HAF allows for the simultaneous estimation of phase and its higher-order derivatives in a computationally efficient manner; thereby allowing for the simultaneous measurement of displacement, strain and curvature of a deformed object in DHI, as will be shown in Chapter 6. Section 4.2 introduces the HAF method by modeling the entire row/column of the reconstructed interference field as an Mth order polynomial phase signal. Performance of the HAF method is compared with the benchmark methods. Section 4.3 presents windowed-HAF method which is suitable for a wide range of applications. Section 4.4 introduces improved-HAF method, which is shown to provide highly accurate results at a tremendously reduced computational time as compared to the contemporary benchmark methods. Simulation and experimental results are presented throughout for substantiating the potentiality of the presented methods.

4.2 High-order Ambiguity Function Method

The reconstructed interference field represented in equation 2.3 can be rewritten as:

$$A_y(x) = b_y(x) \exp\left[j\Delta\phi_y(x)\right] + \eta_y(x) \quad \text{for } x, y = 1, \ldots, N \tag{4.1}$$

where y denotes the index of the row, $b_y(x)$ the amplitude of the yth row, $\eta_y(x)$ the ACWGN with zero-mean and σ^2 variance, and $N \times N$ is the dimension of the fringe

pattern. Since the interference phase to be estimated in DHI is, in general, a continuous function of the spatial coordinates, it can be approximated arbitrarily closely, in accordance to Weierstras approximation theorem [69], by a polynomial of a sufficiently high order. Thus the above equation can be rewritten as:

$$A(x) = b(x) \exp\left[j\left(\sum_{q=0}^{M} a_q x^q\right)\right] + \eta(x) \tag{4.2}$$

where q is an integer and M is the degree of the polynomial. The subscript y is dropped for the sake of simplicity. The problem of estimating the interference phase from the noisy observations of $A(x)$ basically amounts to estimating the parameters like polynomial coefficients $\{a_q\}$ from $A(x)$. In order to estimate the polynomial coefficients from $A(x)$, an operator $PT_M[A, \omega, \tau]$, known as high-order ambiguity function (HAF) [51] is used.

The high-order ambiguity function, $PT_M[A, \omega, \tau]$, is defined as the discrete Fourier transform of another operator, $P_M[A(x), \tau]$, known as high-order instantaneous moments (HIM):

$$PT_M[A, \omega, \tau] = \sum_{x=(M-1)\tau}^{N} P_M[A(x), \tau] \exp(-j\omega x) \tag{4.3}$$

where the HIM operator $P_M[A(x), \tau]$ is defined as:

$$P_M[A(x), \tau] = \prod_{q=0}^{M-1} \left[A^{\dagger q}(x - q\tau)\right]^{\binom{M-1}{q}} \tag{4.4}$$

where $A^{\dagger q}(x) = \begin{cases} A(x) & \text{if } q \text{ is even} \\ A^*(x) & \text{if } q \text{ is odd} \end{cases}$

$(\cdot)^*$ denotes complex-conjugation, τ is a positive real number and $\binom{x}{y} = \dfrac{x!}{(x-y)!\, y!}$.

The properties of the HAF imply that applying the HIM operator P_M on the signal $A(x)$ (which is an Mth order polynomial phase signal), transforms the signal into a single-tone whose frequency, say $\omega_0(\tau)$, is directly proportional to the highest-order polynomial coefficient a_M:

$$a_M = \frac{\omega_0(\tau)}{M!\, \tau^{M-1}} \quad \text{for all } \tau > 0 \tag{4.5}$$

Based on this, the following procedure can be used to estimate the polynomial coefficients $\{a_q\}$: First, P_M of the signal $A(x)$ is computed; which produces a single-tone signal. By calculating its frequency, say by identifying the peak in the FFT spectrum, the highest-order polynomial coefficient a_M can be estimated using the relation in equation 4.5; let $\hat{a}_M$ denote the estimate of a_M. The effect of the highest-order phase term is then removed by "peeling-off" the signal as $A'(x) = A(x) \cdot \exp\left(-j\hat{a}_M x^M\right)$. The new signal $A'(x)$ thus formed is a polynomial phase signal of the order $(M-1)$. Computing P_{M-1} of

$A'(x)$ results in a single-tone signal whose frequency is directly proportional to a_{M-1}. This process of estimating the highest-order coefficient in each iteration and peeling-off the signal to reduce its polynomial phase order is repeated until all the coefficients are estimated. Constructing a polynomial with these estimated coefficients results in the direct estimation of the unwrapped phase. Although the phase estimated along individual rows in this manner is unwrapped, to obtain a continuous 2-D phase distribution phase stitching is needed to weave all the rows to fall in line one after the other. It ordinarily requires determining the off-set phase to be added along the middle column, to make it continuous, and then adding the same to all the columns; this task is as easy as 1D unwrapping of an ideal wrapped phase.

4.2.1 HAF Algorithm

To make the implementation easy, the properties of HAF and the associated procedure for the estimation of polynomial coefficients are provided below in an algorithmic fashion [80]: The basic properties of HAF, PT_M, are:

1. $PT_M[A, \omega, \tau]$ has a global maximum at $\omega = M! \, \tau^{M-1} \, a_M$.

   i.e., $\arg \max_{\omega} |PT_M[A, \omega, \tau]| = M! \, \tau^{M-1} a_M$.

2. $P_M[A(x), \tau]$ is a single tone of frequency $\omega_0(\tau)$ $(\neq 0)$

   i.e., $P_M[A(x), \tau] = B \exp \{j \, [\omega_0(\tau)x + \phi_0(\tau)]\}$,

   where B is a constant or a slowly varying funtion of x.

Therefore $a_M = \dfrac{\omega_0(\tau)}{M! \, \tau^{M-1}}$ for all $\tau > 0$.

HAF-based estimation algorithm proceeds as follows:

1. Initialization: let $m = M$ and $A_x^{(m)} = A_x,$ $\qquad 1 \leq x \leq N$

2. Choose a positive integer τ (which may vary for different values of m)
   Compute $\hat{a}_m$ by

   $\hat{a}_m = \frac{1}{m! \, \tau^{m-1}} \arg \max_{\omega} \left\{ \left| PT_M \left[A_x^{(m)}, \omega, \tau \right] \right| \right\}$

3. Let $A_x^{(m-1)} = A_x^m \cdot e^{-j \hat{a}_m x^m}$ $\qquad 1 \leq x \leq N$

   set $m \leftarrow (m-1)$

4. If $m \geq 1$, go back to step 2. Else go to step 5

5. Estimate a_0 from $A_x^{(0)}$ using the formula

$$\hat{a}_0 = Im \left\{ \log \left[\sum_{x=1}^{N} A_x^{(0)} \right] \right\}$$

Note that in signal processing literature HAF is also referred to as polynomial phase transform (PPT) [51].

In the above process, the choice of τ affects the accuracy of estimated coefficients. It is shown in [81] that, mean square error of a_M achieves a minimum at $\tau = \frac{N}{M}$ for $M = 2, 3$ and $\tau = \frac{N}{M+2}$ for $M \geq 4$.

4.2.2   Simulation and Experimental Results

Figure 4.1 shows the simulation results of phase estimation and error plots. In these simulations, accurate phase estimation is accomplished by modeling the interference field with a fourth-order polynomial phase signal. Figure 4.1a shows the simulated fringe pattern at SNR of 30 dB. This noisy pattern of dimensions 512×512 pixels is generated using AWGN function in MATLAB, which adds additive white Gaussian noise of a specified level to the actual signal. Figure 4.1b shows the profile of the estimated phase with the HAF method along the middle row. Figure 4.1c shows the error plot. 3D plot of the estimated phase over all the rows is shown in figure 4.1d. As is clear from the previous figure, phase stitching is needed to obtain a continuous 2-D phase distribution. Figure 4.1e shows the 3D plot of the interference phase estimated with the HAF method after phase stitching. Error in estimation is shown in figure 4.1f.

The results of this HAF-based method are compared with two commonly used unwrapping algorithms, Goldstein's unwrapping algorithm and ZπM unwrapping algorithm [82–85]. The results are also compared with one of the best performing phase estimation methods, windowed Fourier ridge (WFR) algorithm [40,68,72]. Figure 4.2 shows 3-D mesh plots of error distributions when continuous phase distribution of the pattern shown in figure 4.1a is estimated with all the four methods. WFR method produces results with relatively large errors near the edges of the image. Although the HAF method shows to an extent a similar tendency, it produces relatively small errors. For example, if all pixels of the fringe pattern are considered the root mean square errors (RMSE) produced by WFR and HAF methods are given by 0.0670 and 0.0142, respectively. For this reason, 20 rows and 20 columns on all the four boundaries of the pattern are not considered (size of the window used in WFR algorithm is 10×10) either while calculating the RMSE values listed in Table 4.1 or displaying the error plots in figure 4.2. The RMSE and computational cost for all four methods are listed in Table 4.1. These tests are run on a Windows PC with Intel Core 2 Duo processor of 2.66 GHz, 3.24 GB of RAM and with MATLAB 7.0.4. version. It is evident that the HAF method provides accurate results with relatively less computational time. However, the main strength of this method lies in directly providing the unwrapped phase distribution from a noisy reconstructed interference field.

Figure. 4.3a shows the comparison of error plots when the phase along a row is estimated with the HAF method by approximating the phase of the reconstructed interference field
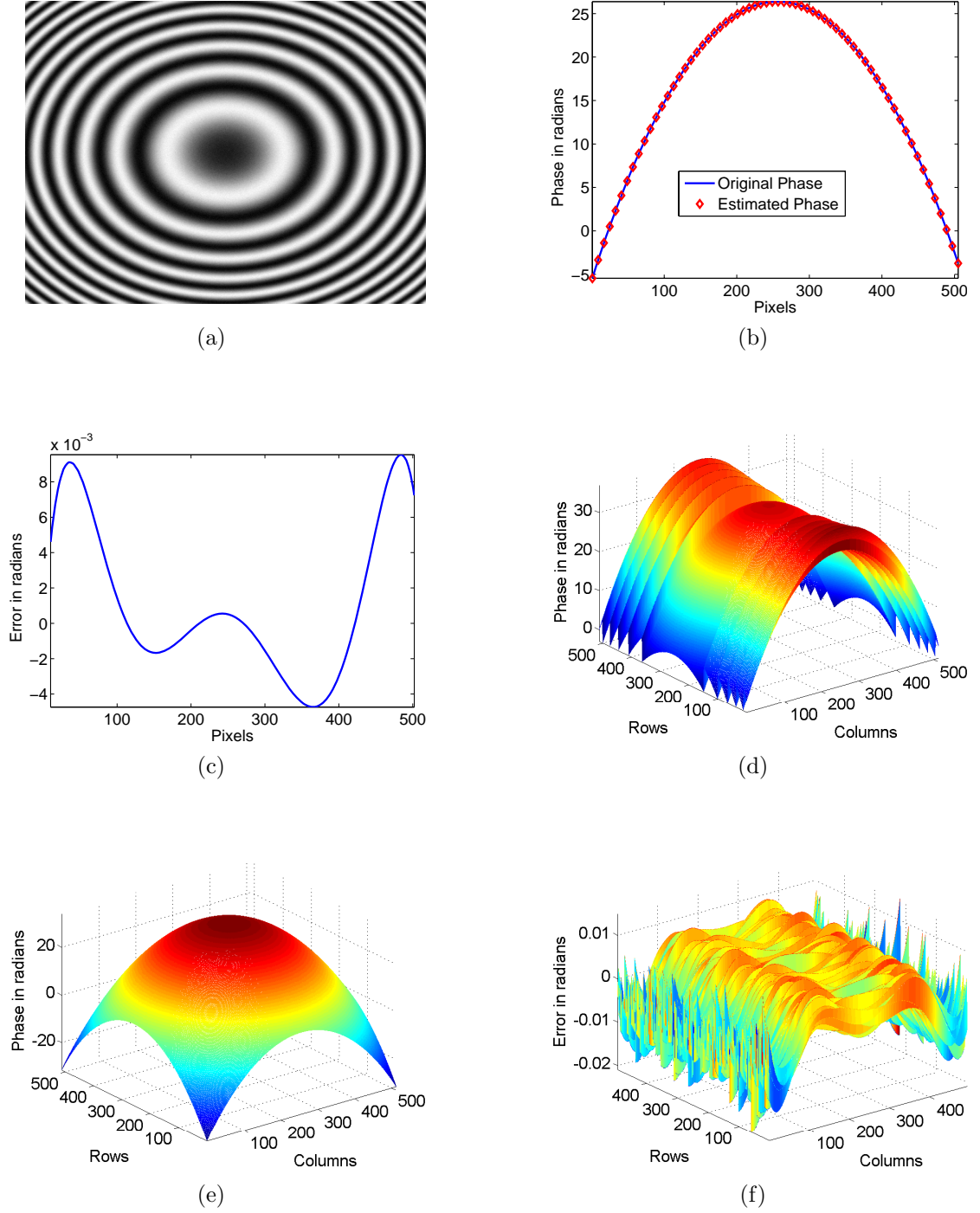
Fig. 4.1: (a) Simulated fringe pattern at $SNR = 30dB$ (512×512) (b) Phase estimated using the HAF-based analysis method along the middle row (c) Error plot, (d) 3D plot of the estimated phase along all rows (e) 3D plot of the resulting phase map after phase stitching, (f) 3-D plot of the error distribution.
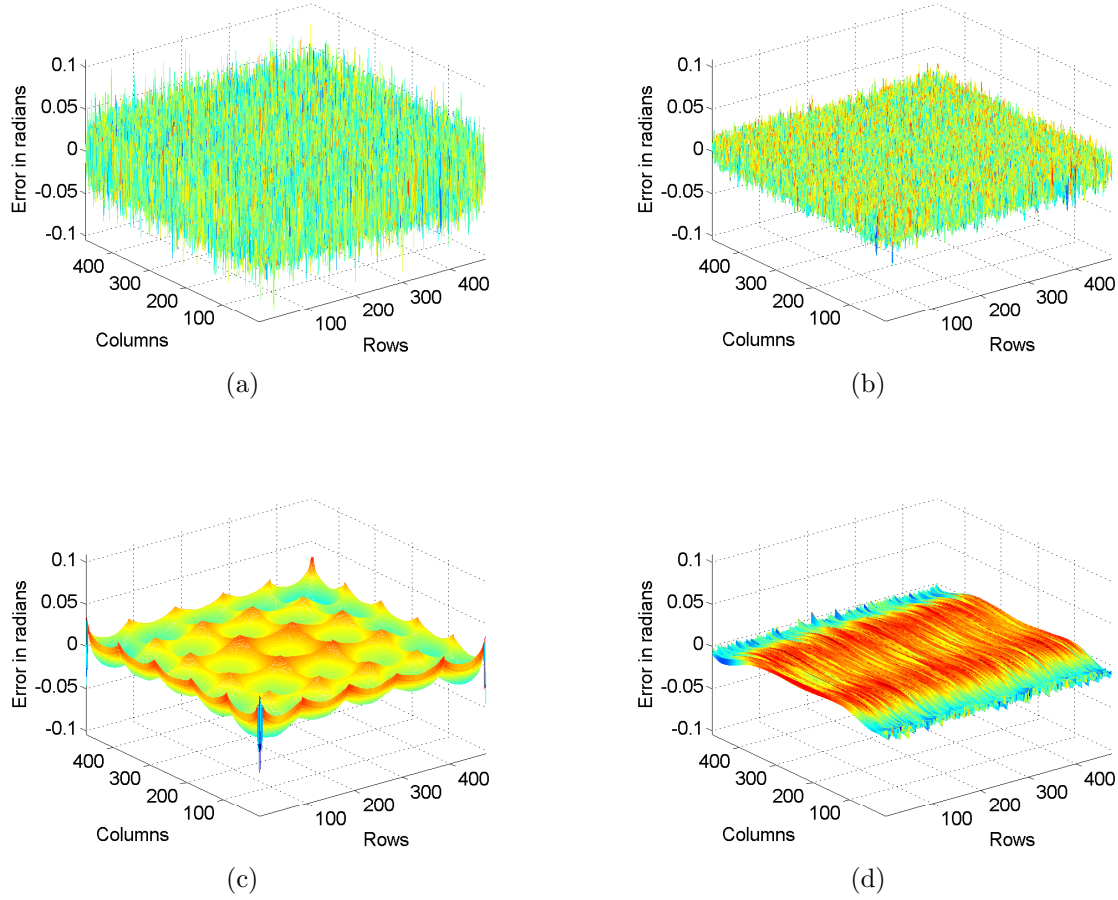
Fig. 4.2: Error plots when continuous phase distribution of figure 4.1a is obtained with (a) Goldstein's unwrapping method (b) ZπM unwrapping method (c) WFR method (d) HAF method

with polynomials of different orders (at SNR=30 dB). These results indicate that if the order of the polynomial used in the approximation is 4 or more, the error (in radians) in the estimation of phase is of the order of 10^{-3}. We have performed error analysis at different SNRs, results of which are shown in figure. 4.3b. This method has the potential to provide an accurate and direct estimation of the continuous phase distribution, with only second-order or third-order polynomial approximations, even if the interference phase is rapidly varying, when applied on different segments of the whole signal. Thus the piecewise polynomial phase approximation approach realized with the HAF method leads to a promising and computationally efficient analysis tool as we will see in the next section.

The experimental results shown in figure. 4.4 substantiate the applicability of the HAF method for the phase estimation in digital holographic interferometry. Figure 4.4a shows the fringe pattern. Figures 4.4b and 4.4c, respectively, show the 3-D mesh plots of the estimated phase distribution using the HAF method before and after phase stitching.

Tab. 4.1: Performance comparison of HAF, WFR, Goldstein's unwrapping, and ZpiM unwrapping algorithms

Method	RMSE	Time (in Sec)
Goldstein	0.0224	46
ZpiM	0.0103	219
WFR	0.0077	400
HAF	0.0047	15

(a)

(b)
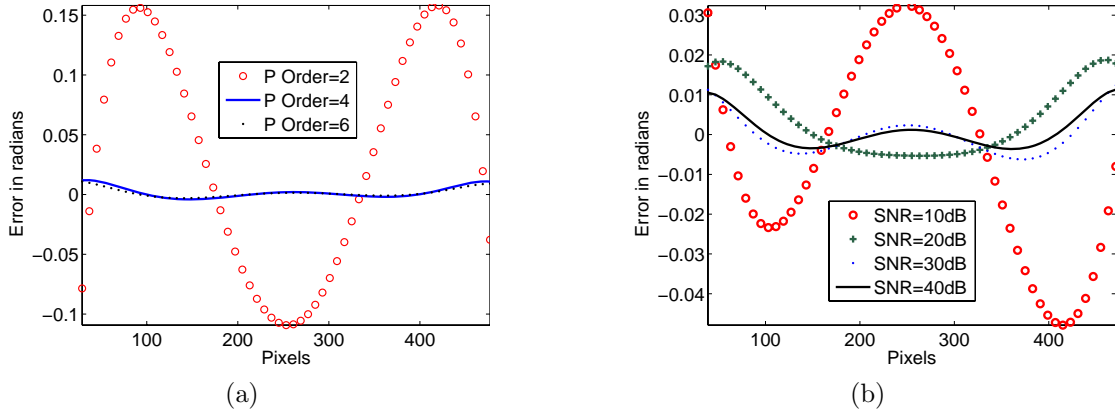
Fig. 4.3: Error plots when (a) Approximated with different orders of polynomials at SNR=30 dB (b) approximated with a 4th order polynomial at different levels of SNR

4.3 Windowed High-order Ambiguity Function Method

In the previous section HAF method is used for modeling the entire row/column of the reconstructed interference field as an Mth order polynomial phase signal. In this section we use the HAF method for realizing P3A2 like in the last two chapters, so that each segment of the data itself is approximated with an Mth order polynomial phase signal.

Figure 4.5a shows the simulated fringe pattern (corresponding to the simulated reconstructed interference field) with an *SNR* of 15 *dB*. This pattern is generated with the peaks function in MATLAB and is chosen to simulate rapid variations in phase. Figure 4.5b

Tab. 4.2: Performance evaluation of WHAF method

Method		RMSE				Time	
WHAF		SNR=15 dB		SNR=30 dB		(in minutes)	
N_w	M	SW	OW	SW	OW	SW	OW
8	4	0.2651	**0.0467**	0.0481	**0.0078**	1.60	**3.04**
8	2	0.2428	**0.0821**	0.2182	**0.0734**	0.79	**1.51**
4	4	0.4094	**0.0638**	0.3876	**0.0459**	0.81	**1.43**

(a)

(b)

(c)
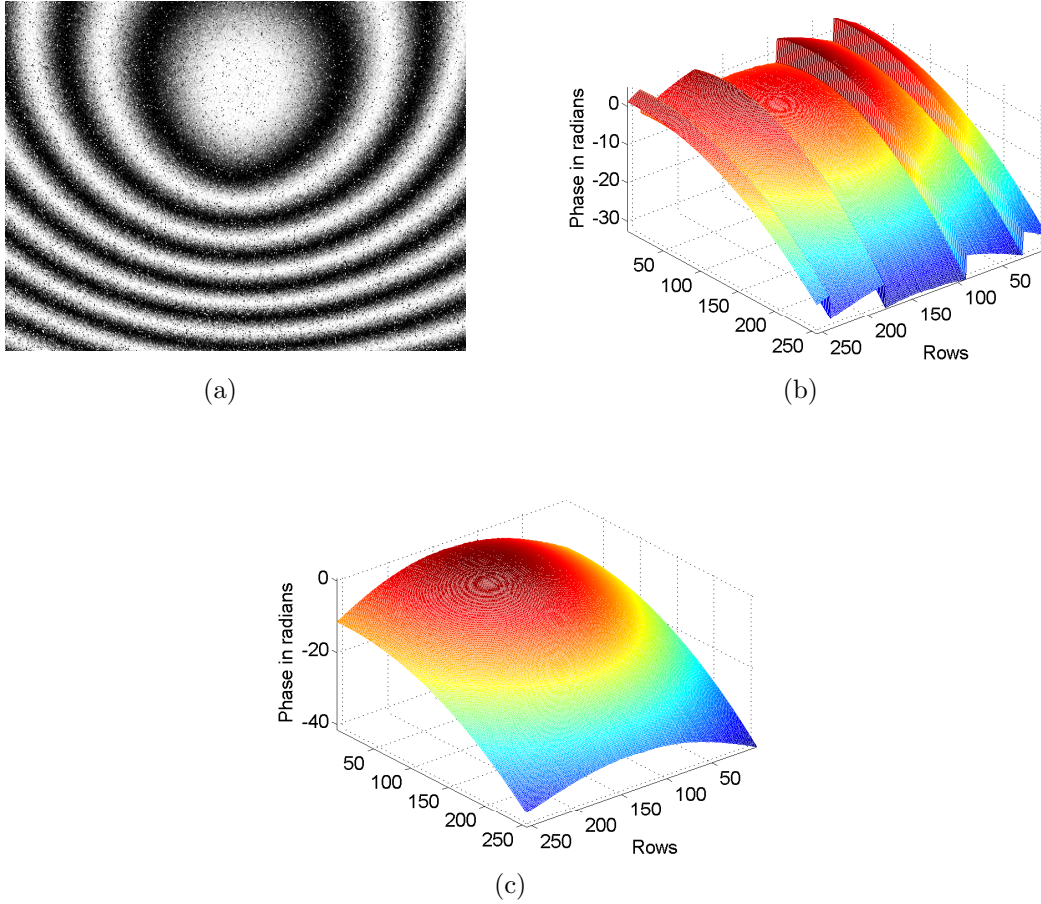
Fig. 4.4: (a) Experimentally recorded fringe pattern corresponding to the loading of a circularly clamped object (b),(c) Estimated phase using the HAF method before and after phase stitching.

shows the estimated phase along the middle column using WHAF. In these simulations the signal is divided into eight segments ($N_w = 8$) and is approximated with a fourth-order polynomial phase signal ($M = 4$) in each window. The estimation procedure is repeated for all columns. Figure 4.5c shows the 3-D plot of the estimated phase distribution over the entire image. Error in phase estimation is shown in figure 4.5d. The number of windows (N_w) and the model order (M) can be chosen depending on the requirements on accuracy and the computational time. Table 4.2 shows the computational time and RMSE values for few such combinations. In the table SW and OW stands for simple windowing and overlapping windowing respectively.

The experimental results are shown in figure 4.6. Figure. 4.6a shows the fringe pattern and figure. 4.6b shows the 3-D mesh plot of the estimated phase distribution using the WHAF method. The pattern shown in figure 4.6a is analyzed also with the maximum likelihood estimation method presented in chapter 2 and the computational times for both the methods are compared in Table 4.3. The WHAF method shows a significant gain in the computational time with respect to the MLE-P3A2 with the increase in the image dimensions.

(a)

(b)

(c)

(d)
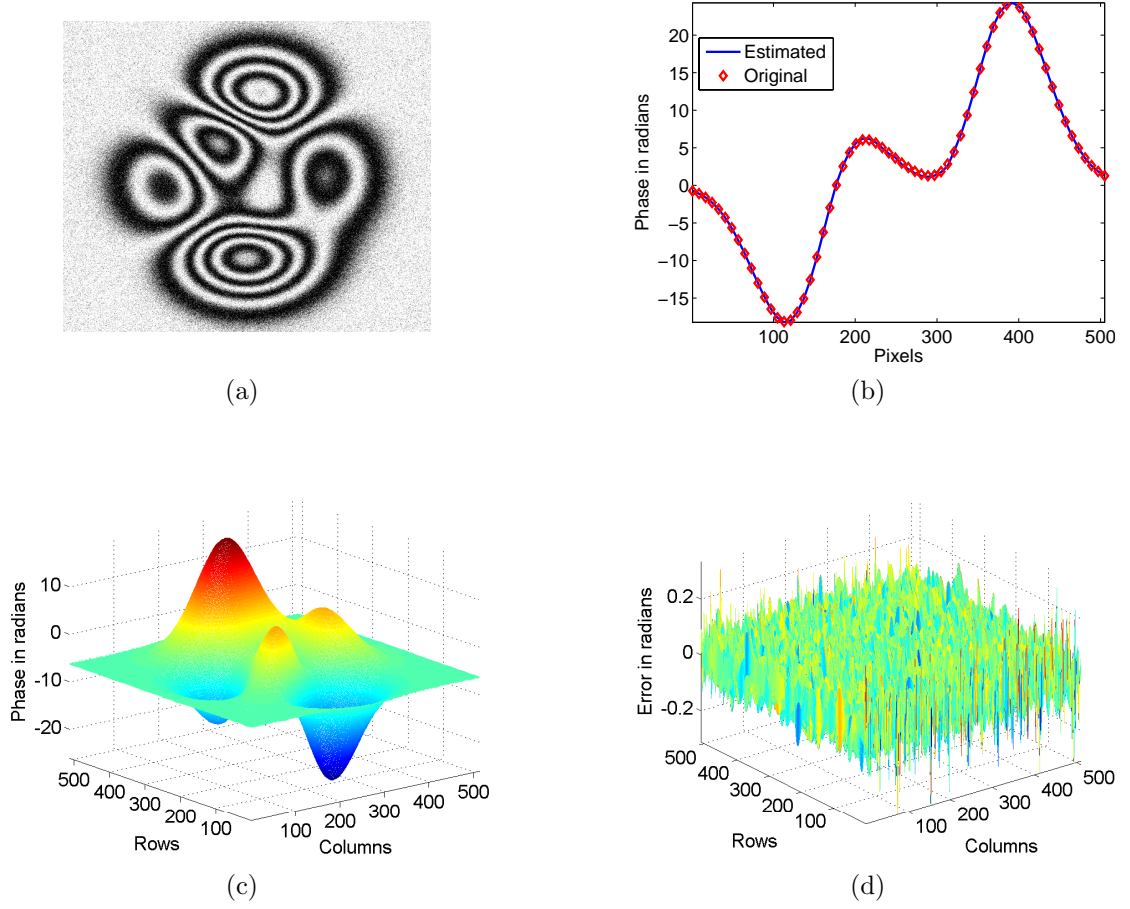
Fig. 4.5: (a) Simulated fringe pattern at SNR of $15\,dB$ (512 x 512), (b) Estimated phase along the middle column using WHAF method ($N_w = 8, M = 4$), (c) 3-D plot of the estimated phase over the whole image, (d) Error in phase estimation.

(a)

(b)
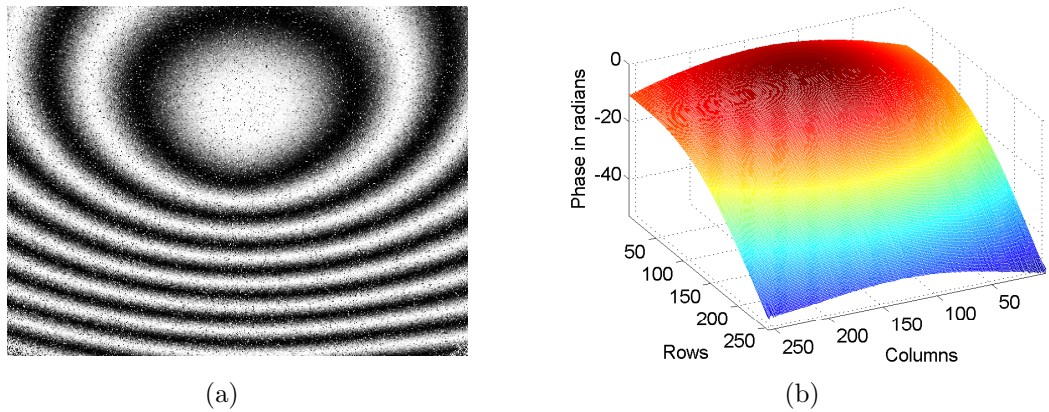
Fig. 4.6: (a) Fringe pattern obtained in a DHI experiment corresponding to the loading of a circularly clamped object, (b) 3D mesh plots of the phase distributions estimated using the WHAF method ($N_w = 8, M = 2$).

Tab. 4.3: Comparison of computational times of WHAF and MLE methods

Parameters		Time (in minutes)			
		256 x 256 image		512 x 512 image	
N_w	M	MLE-P3A2	WHAF	MLE-P3A2	WHAF
4	2	7	**0.5**	103	**0.7**
8	2	3	**0.7**	30	**1.5**

4.4 Improved High-order Ambiguity Function Method

Two important driving factors behind the development of various fringe analysis method during last two decades are to achieve higher accuracy of estimation and less computational time requirements. Thus in this section we further seek to improve the WHAF method so as to reduce its computational time and improve its performance in terms of accuracy of estimation. The resulting method is named as improved HAF method.

A careful study of the HAF method reveals that the overall accuracy of the estimated phase and associated computational cost with it primarily depends on two factors: firstly, on the ability of the P_M operator to transform the signal into a single-tone of proper frequency and secondly, on the accuracy and speed with which the frequency of the single-tone is estimated in each iteration. In this section we try to investigate for the potential solution for the above two issues.

To address the first issue, instead of the conventional HIM operator, a modified HIM operator P_M is used which is defined as:

$$P_M\left[A_i(x), \tau_q\right] = \prod_{q=0}^{M-1} \left[A_i^{\dagger q}(x - q\,\tau_q)\right]^{\binom{M-1}{q}} \tag{4.6}$$

where $A_i^{\dagger q}(x) = \begin{cases} A_i(x) & \text{if } q \text{ is even} \\ A_i^*(x) & \text{if } q \text{ is odd} \end{cases}$

$(\cdot)^*$ denotes complex-conjugation, $\tau_1, \tau_2, .., \tau_{M-1}$ are the set of delay parameters and $\binom{x}{y} = \dfrac{x!}{(x-y)!\,y!}$. Note that the P_M operator of the original HAF uses single delay parameter, τ, which boils down to imposing equal values to all $M-1$ delay parameters. But by considering $M-1$ different delay parameters (see Table 4.4) as in Eq.(4.6), all of which are chosen to minimize the mean square error of the estimated coefficients [86], a considerable improvement in the accuracy of estimation can be observed, especially when the order of the polynomial approximation is three or greater.

The next step is to estimate the frequency of the single-tone signal resulted after applying the operator P_M. Let ω_{i0} be the estimated frequency. The highest order coefficient a_M of a given segment i can then be calculated as:

$$\hat{a}_{iM} = \frac{\omega_{i0}}{M!\,\gamma} \tag{4.7}$$

Tab. 4.4: Optimal set of delay parameters of IHAF as fractions of number of samples (N) present in the signal

M	$(\tau_1, \tau_2, .., \tau_{M-1})$ as fractions of N
2	0.5
3	0.12, 0.44
4	0.08, 0.18, 0.37
5	0.07, 0.19, 0.24, 0.31

where $\gamma = \prod\limits_{q=1}^{M-1} \tau_q$ and $\hat{a}_{iM}$ denote the estimate of a_{iM}. The effect of the highest-order phase term can then be removed by 'peeling-off' the signal as $A_i'(x) = A_i(x) \cdot \exp\left(-j\hat{a}_{iM}x^M\right)$. The new signal $A_i'(x)$ thus formed is a polynomial phase signal of the order $(M-1)$. Computing P_{M-1} of $A_i'(x)$ again results in a single-tone signal whose frequency is directly proportional to $a_{i(M-1)}$. This process of estimating the highest-order coefficient in each iteration and peeling-off the signal to reduce its polynomial phase order is repeated until all the coefficients are estimated.

Thus it is also important to investigate on the proper choice of the method that can be employed to estimate the frequency of the single tone in each iteration, as it can have a significant influence on the accuracy of the estimated coefficients as well as on the overall computational investment required.

A popular approach for single-tone frequency estimation is the Fourier transform. But since it usually gives gross estimates, the estimation accuracy needs to be further improved using an optimization routine. Other important single-tone frequency estimation techniques are estimation of signal parameters by rotational invariance technique (ESPRIT) [87], multiple signal classification (MUSIC) [88] and iterative frequency estimation by interpolation on Fourier coefficients (IFEIF) [89]. Now our aim is to test the performance of these different techniques under various noise levels for phase estimation and find the optimal technique that provides minimal estimation error with the least computational burden.

Different fringe patterns (size 512×512) were simulated at different SNRs of 15, 20, 25

Tab. 4.5: Performance comparison of various single-tone frequency estimation techniques for phase estimation at different SNRs

Technique	RMSE in radians				Time in seconds
	SNR 15 dB	SNR 20 dB	SNR 25 dB	SNR 30 dB	
FT with optimization	0.0446	0.0245	0.0144	0.0090	261.514
MUSIC	0.0597	0.0311	0.0173	0.0105	32.061
ESPRIT	0.0585	0.0303	0.0170	0.0104	14.974
IFEIF	0.0427	0.0232	0.0135	0.0078	5.882

and 30 dB using MATLAB 'peaks' function as the interference phase. The WHAF method with the modified HIM operator is used for phase estimation by applying different single-tone frequency estimation techniques like Fourier transform (FT) followed by optimization using 'FMINBND' function of MATLAB, MUSIC, ESPRIT and IFEIF. For the analysis, we used $N_w = 8$ and $M = 4$. For the implementation of the ESPRIT and MUSIC techniques, we took the values of the model order and the order of the covariance matrix [90] as 1 and 9 respectively. The RMSE values for the phase estimation and the computational time taken in seconds on a 2.66 GHz Intel Core 2 Quad Processor machine with 3.23 GB RAM for these methods at various SNRs are shown in Table 4.5. From the table, it is clear that the IFEIF technique exhibits the optimum performance in terms of estimation accuracy and computational efficiency.

Note that, with these modifications, now we are no longer calculating the HAF (which is the Fourier transform of HIM) but only applying the modified HIM operator (see equation 4.6) and determining the frequency of the resulting single-tone with the IFEIF method. Thus the modified method here onwards is referred to high-order instantaneous moments based method or simply HIM method.

(a)

(b)

(c)
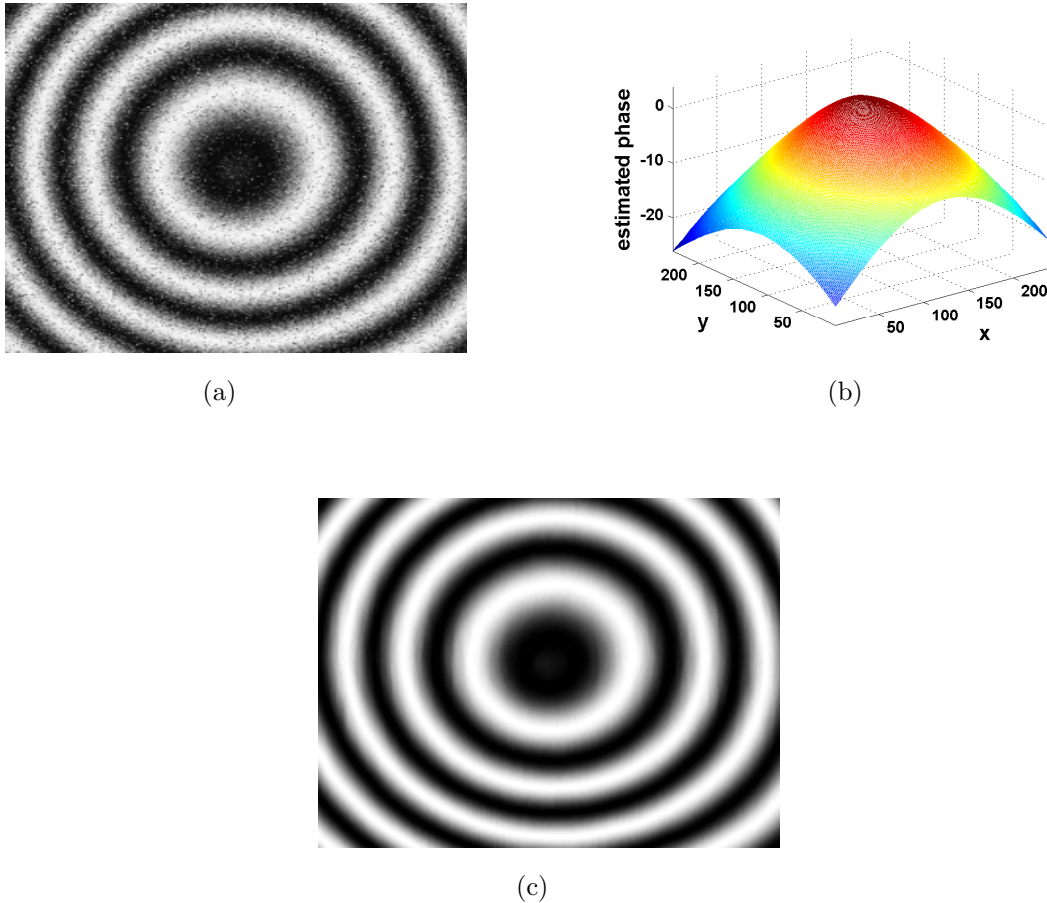
Fig. 4.7: (a) Experimental fringe pattern at (256 x 256), (b) Estimated phase in radians using the HIM method ($N_w = 8, M = 3$), (c) Cosine fringes of the estimated phase.

To verify the practical utility in using the IFEIF technique with the HIM method, an experimental fringe pattern obtained in DHI shown in figure 4.7a was taken for analysis. The estimated phase in radians obtained using the IFEIF technique based method and subsequent median filtering is shown in figure 4.7b. We used $N_w = 8$ and $M = 3$ for the analysis. The cosine fringes of the estimated phase are shown in figure 4.7c. It has taken only 1.786 seconds for the analysis of this pattern.

4.5 Conclusions

This chapter has developed high-order ambiguity function based method for the estimation of interference phase in DHI. The HAF possess an exceptional ability to approximate the data with a higher-order polynomial signal (4th order or so) with relatively less computational requirements. After developing the basic method, its performance is compared with the benchmark methods and is found to be very promising with its unique advantages. In the later sections, efforts are made to bring further improvements in the method by performing a careful study. Two important issues/factors are identified, that are found to be responsible for the overall phase estimation accuracy and the required computational time. Investigations are carried out to provide optimal solutions for those two issues.

Firstly, the use of an optimal set of $M - 1$ delay parameters while applying P_M operator is suggested to obtain accurate estimates. The other modification consists of using IFEIF method for the task of single-tone frequency estimation. These modifications provide a robust solution to implementing a fringe analysis tool for a direct estimation of the unwrapped phase distribution in a computationally highly efficient manner. The resulting method is referred to as improved high-order ambiguity function (IHAF) or high-order instantaneous moments (HIM) method.

Chapter 5

Cubic Phase Function Method

5.1   Introduction

Previous chapter has presented an effective fringe analysis method based on high-order instantaneous moments calculation. As it allows for higher-order polynomial approximation ($M > 2$), that too in a computationally efficient manner, it will find its place in many metrological applications. However, it is worth noting that the performance of HIM is interlinked with other parameters such as signal-to-noise ratio, number of samples and the model order [51]. Our experience confirms that HIM method can perform well as long as signal-to-noise ratio is greater than 10 dB. In applications where the recorded fringe patterns are expected to have heavy noise, HIM method is thus prone to provide phase estimation with non-negligible errors. To address this concern, a robust cubic phase function (CPF) based method, which provides accurate results even at very low signal-to-noise ratio levels, is introduced in this chapter. This method makes a cubic phase approximation (i.e. third-order polynomial phase approximation) over each segment of the reconstructed interference field, and the computation of polynomial coefficients is achieved in an efficient manner by making use of the properties of the cubic phase function [91].

5.2   Cubic Phase Function Method

In this method, data in each segment of the reconstructed interference field is modeled as a third-order polynomial phase signal:

$$g(x) = b(x) \exp\left[j(a_0 + a_1 x + a_2 x^2 + a_3 x^3)\right] + \eta(x) \tag{5.1}$$

The polynomial coefficients in the above equation are estimated by computing the cubic phase function [91] as:

$$CPF(x, \Omega) = \sum_{\tau=0}^{(N_s-1)/2} g(x+\tau)g(x-\tau)exp(-j\Omega\tau^2) \tag{5.2}$$

The CPF has an important property that its peak always corresponds to the second-order derivative of phase which is also referred to, in signal processing, as instantaneous

frequency rate (IFR). Here we denote the second-order derivative of phase as $IFR(x)$. So we have

$$IFR(x) = \frac{\partial^2 \phi(x)}{\partial x^2} \tag{5.3}$$

and using equation 5.1, we have

$$IFR(x) = 2a_2 + 6a_3x \tag{5.4}$$

Since the maxima of the CPF is associated with the second-order derivative of phase i.e. $IFR(x)$, we have

$$IFR(x) = \arg\max_{\Omega} |CPF(x, \Omega)| \tag{5.5}$$

Equation 5.4 represents a linear equation in x where $IFR(x)$ depends on the polynomial coefficients a_2 and a_3. To estimate a_2 and a_3, $IFR(x)$ is evaluated using equation 5.5 for two positions of x, say x_1 and x_2, yielding $IFR(x_1)$ and $IFR(x_2)$. In other words, we have

$$IFR(x_1) = 2a_2 + 6a_3x_1 \tag{5.6}$$

$$IFR(x_2) = 2a_2 + 6a_3x_2 \tag{5.7}$$

So we have two equations in two variables which can be solved to obtain the estimates $[\hat{a}_2, \hat{a}_3]$. The optimal values of x_1 and x_2 for minimal estimation errors are 0 and $0.11N_s$ [92]. Once $\hat{a}_2$ and $\hat{a}_3$ are evaluated, the polynomial coefficient a_1 is estimated using a dechirping operation given by

$$g'(x) = g(x)exp[-j(\hat{a}_2x^2 + \hat{a}_3x^3)] \tag{5.8}$$

In equation 5.8, the dechirping operation peels off or removes the contribution of quadratic and cubic terms from the polynomial phase effectively yielding $g'(x)$ as a single-tone signal with frequency a_1. Since $g'(x)$ is a single-tone signal, the peak of the Fourier spectrum of $g'(x)$ obtained by the Fourier transform (FT) gives the estimate $\hat{a}_1$. So we have

$$U(\omega) = FT[g'(x)] \tag{5.9}$$

$$\hat{a}_1 = \arg\max_{\omega} |U(\omega)| \tag{5.10}$$

The single-tone frequency estimation procedure in the above equations is efficiently implemented using the fast Fourier transform (FFT) algorithm and the computationally efficient iterative frequency estimation by interpolation on Fourier coefficients (IFEIF) technique [89] is used to improve the estimation accuracy. After determining the estimate $\hat{a}_1$, the coefficient a_0 is estimated as

$$\hat{a}_0 = angle\left\{ \sum_{x=-(N_s-1)/2}^{(N_s-1)/2} g(x)exp[-j(\hat{a}_1x + \hat{a}_2x^2 + \hat{a}_3x^3)] \right\} \tag{5.11}$$

Once the polynomial coefficients estimates $[\hat{a}_0, \hat{a}_1, \hat{a}_2, \hat{a}_3]$ are known, phase $\phi(x)$ can be evaluated for that particular segment. The above procedure is subsequently performed for all N_w segments to give the phase estimate for a given row y. To keep the error minimum at the boundary of adjacent segments, as explained in chapter 3, a 50 % overlapping segment strategy is used. Finally, the above approach is repeated for all columns to give the overall phase estimate for the entire fringe pattern.

5.2.1 CPF Algorithm

To make the implementation easy, the properties of CPF and the associated procedure for the estimation of polynomial coefficients are provided below in an algorithmic fashion [92]:

$$CPF(x, \Omega) = \sum_{\tau=0}^{(N_s-1)/2} g(x+\tau)g(x-\tau)exp(-j\Omega\tau^2)$$

$$I\hat{F}R(x) = \arg\max_{\Omega} |CPF(x, \Omega)|$$

1. Estimate two IFRs $\hat{\Omega}_1$ and $\hat{\Omega}_2$, at locations, x_1 and x_2, respectively

$$\hat{\Omega}_1 = \arg\max_{\Omega} |CPF(x_1, \Omega)|$$

$$\hat{\Omega}_2 = \arg\max_{\Omega} |CPF(x_2, \Omega)|$$

   (Suggested values of x_1 and x_2 at which asymptotic mean square error of estimates is minimum are 0 and $0.11N$ respectively.)

2. Let $\hat{a} = [\hat{a}_2, \hat{a}_3]^T$, $\hat{R} = [\hat{\Omega}_1, \hat{\Omega}_2]^T$ and

$$X = \begin{bmatrix} 2 & 6x_1 \\ 2 & 6x_2 \end{bmatrix}$$

   Then compute $\hat{a}$ according to $\hat{a} = X^{-1}\hat{R}$

3. Estimate $\hat{a}_1$ by dechirping followed by single-tone frequency estimation:

$$\hat{a}_1 = \arg\max_{a_1} \left| \sum_{x=-(N_s-1)/2}^{(N_s-1)/2} g(x) \, e^{-j(a_1 x + \hat{a}_2 x^2 + \hat{a}_3 x^3)} \right|$$

4. Find $\hat{a}_0$ by evaluating

$$\hat{a}_0 = angle \left[\sum_{x=-(N_s-1)/2}^{(N_s-1)/2} g(x) \, e^{-j(\hat{a}_1 x + \hat{a}_2 x^2 + \hat{a}_3 x^3)} \right]$$
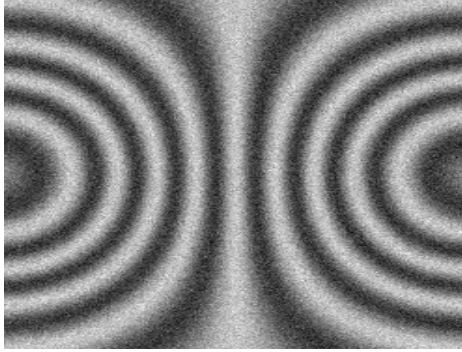
(a)
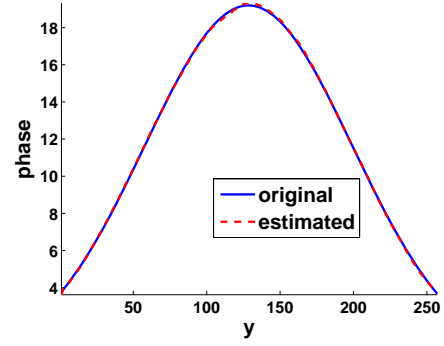
(b)
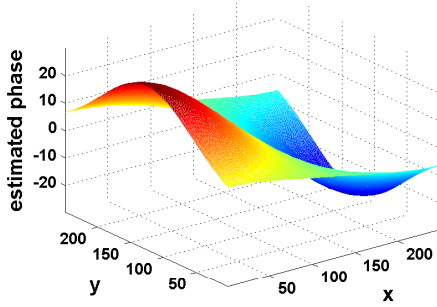
(c)
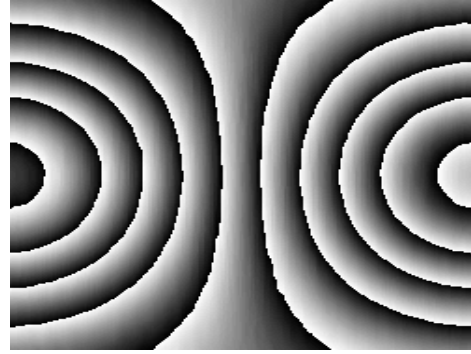
(d)
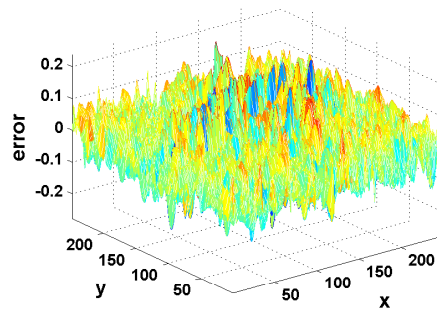
(e)

Fig. 5.1: (a) Simulated fringe pattern at SNR of 10 dB. (b) Original vs estimated phase in radians for column $x = 64$. (c) Estimated phase in radians for the entire fringe pattern. (d) Wrapped form of the estimated phase. (e) Error between the original and the estimated phase in radians

5.2.2 Simulation and experimental results

To test the method's validity, a 256×256 pixels fringe pattern (corresponding to reconstructed interference field) was simulated at SNR of 10 dB as shown in figure 5.1a. The original phase and estimated phase by the proposed method in radians for a particular column $x = 64$ are shown in figure 5.1b. The estimated phase in radians for the entire fringe pattern and the corresponding wrapped form are shown in figure 5.1c and figure 5.1d. $N_w = 8$ was used for the analysis. The error between the original and the estimated phase is shown in figure 5.1e. The RMSE for phase estimation was 0.0535 radians.

The CPF method's performance for the simulated fringe pattern under different SNRs is shown in Table 5.1. The RMSEs for phase estimation with the CPF method were evaluated for SNRs of 5, 10, 15 and 20 dB as shown in the table. The tabular results show that the proposed CPF method is robust for phase estimation even under the presence of high noise and low SNR.

A comparison between the HIM and CPF methods for phase estimation under low SNR is shown in figure 5.2. The simulated fringe pattern at SNR of 5 dB is shown in figure 5.2a. The wrapped form of the phase estimates obtained using the HIM and CPF methods are shown in figure 5.2b and figure 5.2c. Note that both the HIM and CPF methods directly provide the unwrapped phase estimate and the wrapped forms are shown here for the purpose of illustration only. The errors between the original and the estimated phases for the HIM and CPF methods are shown in figure 5.2d and figure 5.2e. The RMSEs for phase estimation by the HIM and CPF based methods were 2.1118 radians and 0.0910 radians. figure 5.2d and figure 5.2e show that the performance of the CPF based method is superior to that of the HIM method under severe noise conditions.

The method's practical applicability is tested by measuring the out of plane displacement of a circularly clamped object subjected to loading in a DHI experiment. The fringe pattern corresponding to the real part of reconstructed interference field is shown in figure 5.3a. The estimated phase distribution in radians obtained using the CPF method and after applying two dimensional median filtering is shown in figure 5.3b. The corresponding wrapped form of the estimated phase distribution is shown in figure 5.3c.

Tab. 5.1: Performance evaluation of CPF method with respect to noise in estimating phase

	SNR in dB	RMSE in radians
1	5	0.0910
2	10	0.0535
3	15	0.0327
4	20	0.0209
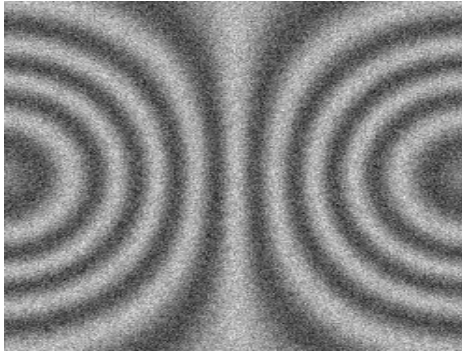
(a)
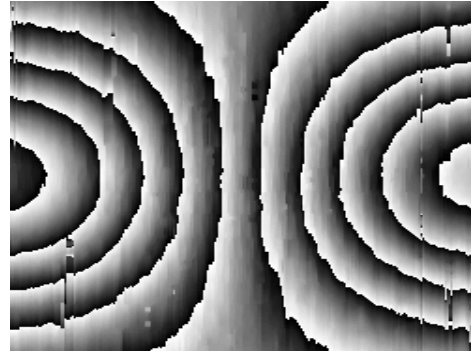
(b)
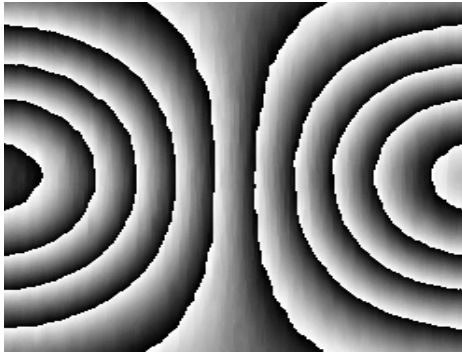
(c)
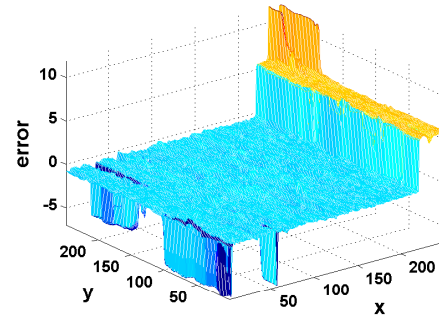
(d)
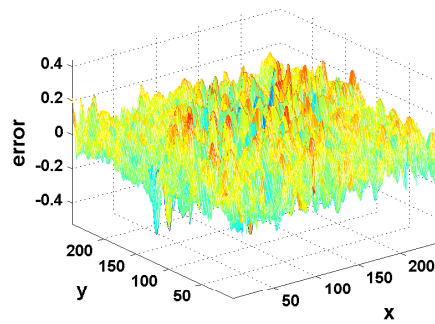
(e)

Fig. 5.2: (a) Simulated fringe pattern at SNR of 5 dB. (b) Wrapped form of the estimated phase using HIM method. (c) Wrapped form of the estimated phase using CPF method. Error between the original and the estimated phases in radians for the (d) HIM method, (e) CPF method.

(a)

(b)

(c)
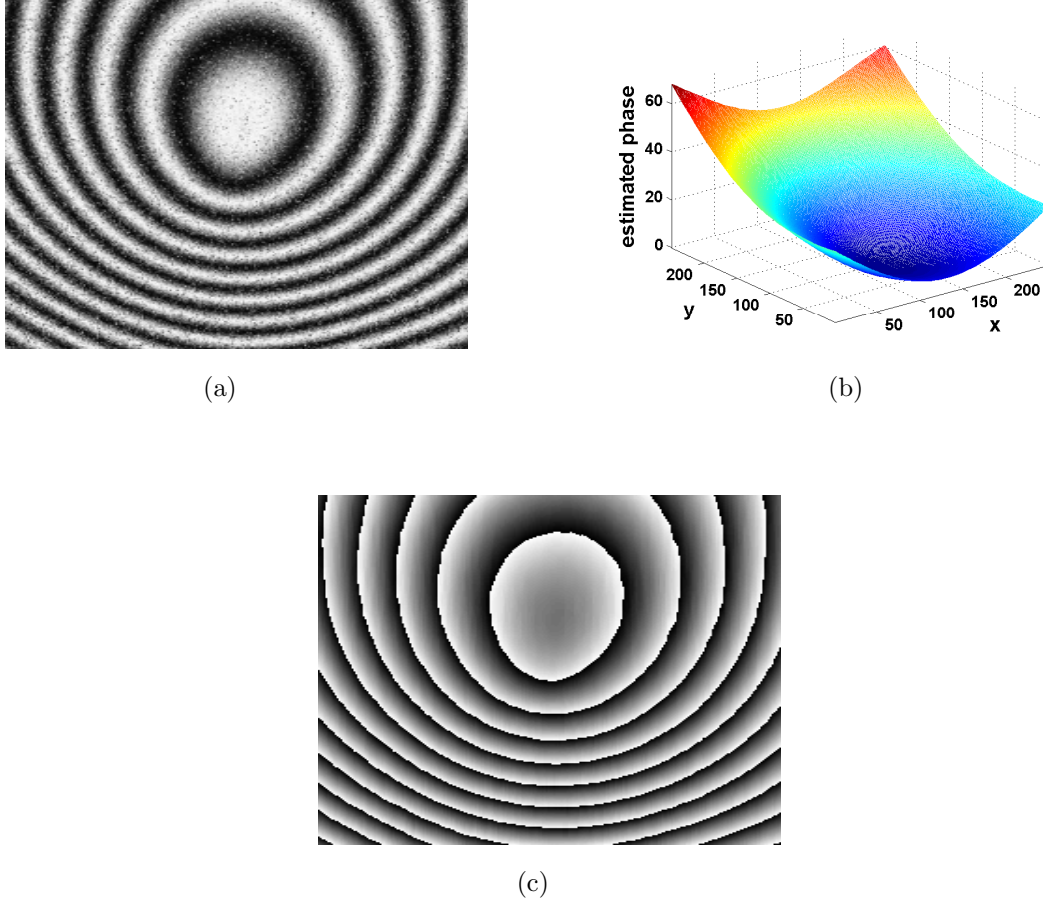
Fig. 5.3: (a)Experimental fringe pattern. (b) Estimated phase distribution in radians using the CPF method. (c) Wrapped form of the estimated phase

5.3 Phase Derivative Estimation using CPF

In chapter 3, the use of DCFT method is demonstrated for obtaining an accurate and direct estimation of the phase derivative from a fringe pattern. In this section we show the advantage of using CPF for phase derivative estimation. From equation 5.1, we can have:

$$\frac{\partial \phi}{\partial x} = a_1 + 2a_2x + 3a_3x^2 \tag{5.12}$$

Phase derivative can thus be estimated by computing the polynomial coefficients a_1, a_2, a_3 over all segments, using the CPF as explained in the previous section.

The major advantage of the CPF method is its inherent robustness to severe noise. To examine its performance for phase derivative estimation, we simulated a one dimensional signal at SNR of 5 dB, 10 dB and 15 dB. The obtained estimates are shown in figure 5.4a-5.4c. The absolute errors in phase derivative estimation for different SNRs are shown in figure 5.4d. It is clear from figure 5.4 that even for SNR as low as 5 dB, the CPF method works reasonably well for phase derivative estimation.
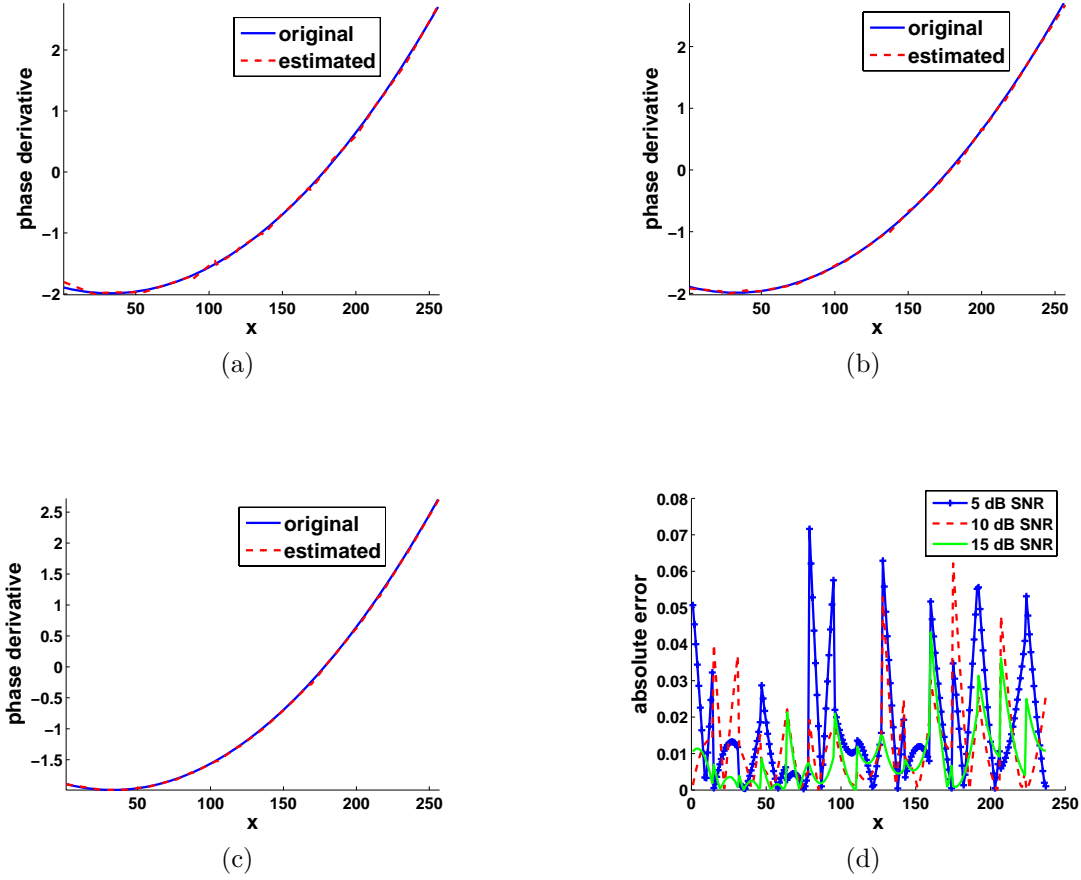
Fig. 5.4: Original vs estimated phase derivative in radians/pixel at SNR of (a) 5 dB, (b) 10 dB, (c) 15 dB. (d) Absolute error for phase derivative estimation

A simulated fringe pattern corresponding to the real part of the reconstructed interference field at SNR of 5 dB is shown in figure 5.5a. The original phase derivative along y direction in radians/pixel is shown in figure 5.5b. The phase derivative estimate $\omega_1(x, y)$ in radians/pixel obtained by applying the CPF method is shown in figure 5.5c. $N_w = 8$ is used for the analysis. Though the phase derivative obtained from the CPF method is unwrapped, the corresponding wrapped form is shown for illustration purpose only in figure 5.5d. The wrapped form was evaluated using $\arctan\{\text{Im}(exp[j\omega_1(x, y)])/\text{Re}(exp[j\omega_1(x, y)])\}$, where 'Im' and 'Re' denote the imaginary and real parts of a complex number. The RMSE value for phase derivative estimation was 0.0166 radians/pixel.

The practical applicability of the CPF method for phase derivative estimation is tested for a DHI experiment. The fringe pattern corresponding to a circularly clamped object subjected to central loading is shown in figure 5.6a. The estimated phase derivative along y direction using the CPF method and the corresponding wrapped form are shown in figure 5.6b and figure 5.6c. For the sake of comparison, the phase derivative was also estimated with the commonly used digital shearing method, where the sheared complex amplitude of the reconstructed wave was superimposed on the original complex amplitude to approximate the phase differentiation operation. The wrapped phase derivative

(a)

(b)

(c)

(d)
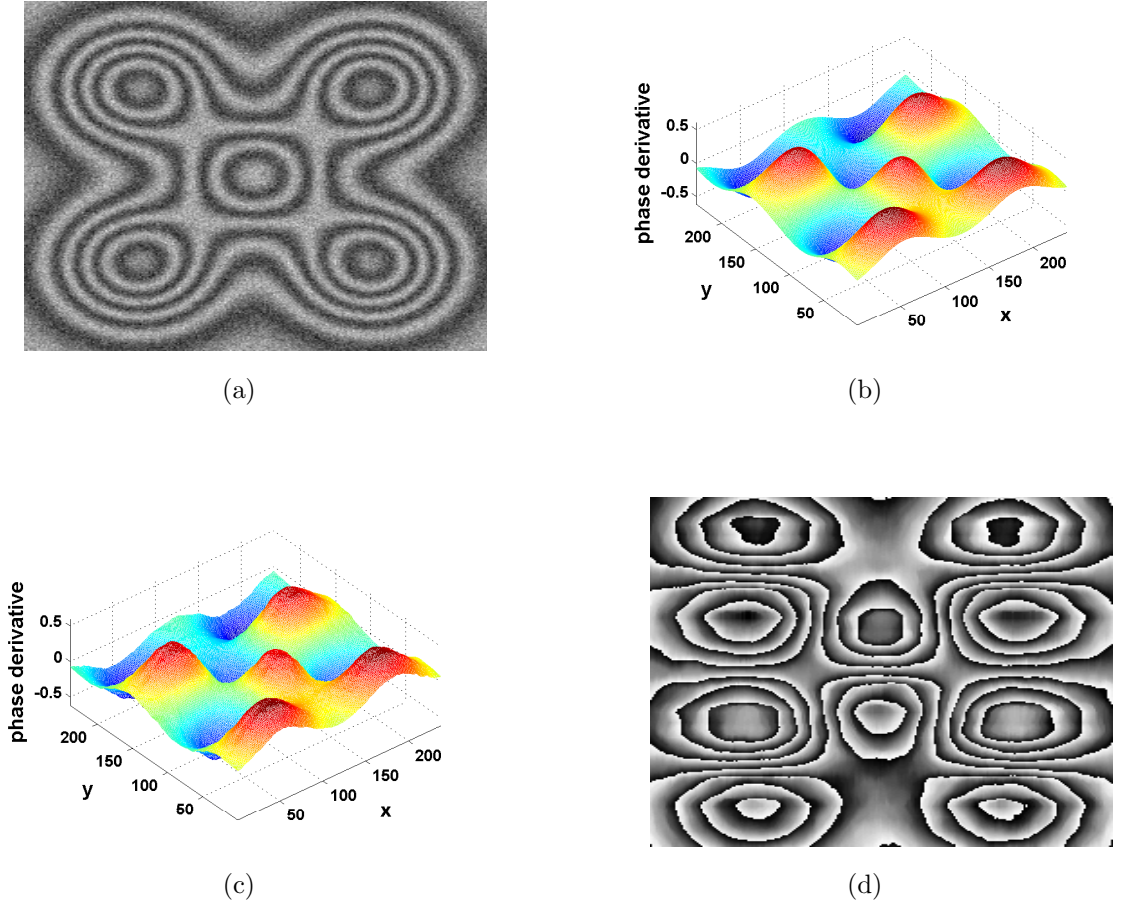
Fig. 5.5: (a) Simulated fringe pattern at SNR of 5 dB. (b) Original phase derivative in radians/pixel. (c) Estimated phase derivative in radians/pixel. (d) Wrapped form of the estimated phase derivative

estimate thus obtained is shown in figure 5.6d. It is clear from figure 5.6d that the digital shearing method is susceptible to noise besides requiring an unwrapping algorithm.

5.4 Conclusions

This chapter presented a CPF based method for the estimation of phase and its derivative in digital holographic interferometry. The method has the advantage of directly providing the unwrapped distributions and robustness against severe noise conditions.
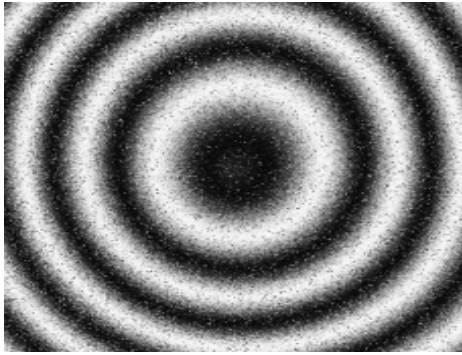
(a)
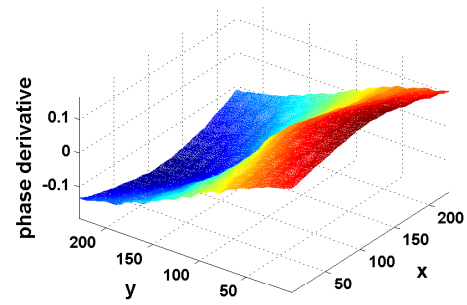
(b)
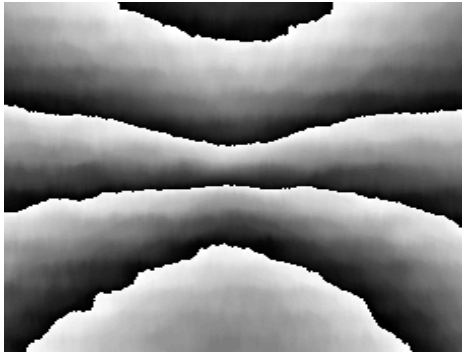
(c)
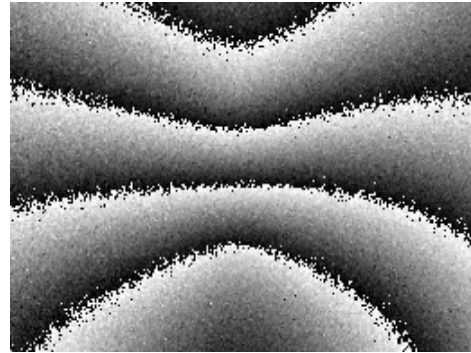
(d)

Fig. 5.6: (a) Fringe pattern obtained in a DHI experiment. (b) Estimated phase derivative in radians/pixel. (c) Wrapped form of the estimated phase derivative. (d) Wrapped phase derivative estimate obtained using digital shearing method.

Chapter 6

Applications in Holographic Interferometry

6.1 Introduction

In the preceding chapters, we have introduced a series of fringe analysis methods based piecewise polynomial phase approximation, where the estimation of polynomial coefficients is performed using tools such as MLE, DCFT, HIM, and CPF. In this chapter and the next one, the potential of P3A2 in real-life applications is demonstrated. In particular, the HIM method's applicability for various types of measurements in non-destructive testing and evaluation are presented in this chapter. The methods usefulness in both digital holographic interferometry and classical holographic interferometry is discussed.

6.2 Digital Holographic Interferometry

Digital holographic interferometry has emerged as a powerful non-invasive measurement and testing tool in diverse areas of science and engineering. Thanks to the high-resolution CCD camera, which has facilitated the direct digital recording of the holograms, the wet and time consuming chemical processing involved in the recording of holograms has been eliminated. The development of numerical hologram reconstruction methods based on Fresnel diffraction integral [93], Wavelet transform [94], Fresnelets [95], etc., has enabled obtaining the reconstruction of object wave fields in the computer. In DHI, the key parameter of interest is the phase of the reconstructed interference field, as the information on the measurand is encoded in it. Usually, it provides the information on the deformation or displacement.

As mentioned in the introduction chapter, in the light of some of the unique advantages associated with DHI, efforts have also been made during recent years [33–38] to extend its use to the measurement of slopes and curvatures. However, they have met with limited success, as the first and second-order derivatives calculated by their approach are observed to be contaminated with severe noise (in addition to being wrapped). Consequently, different filtering schemes such as those based on average filter, sine/cosine transform

and short-time Fourier transform have been proposed [37,38]. Nevertheless, the iterative filtering operations are computationally demanding and need to be carefully implemented so as not to smear the dense fringes.

In the following subsection, we show how the P3A2 provides an elegant solution for this problem. Here we briefly review the procedure involved in making measurements in DHI and provide the details of the experiments carried out in our lab.

Two digital holograms, one before and the other after loading the object, are recorded in an off-axis DHI configuration by illuminating the test object with a *Coherent Verdi* laser (532 nm). The schematic of the off-axis DHI and the experimental setup are shown in figures. 6.1 and 6.2, respectively. Figure. 6.3a shows the image of the digital hologram recorded before subjecting the object to loading. Discrete Fresnel transform [65] is used to perform the numerical reconstruction of the individual holograms. Figure. 6.3b shows the amplitude of the numerical reconstruction of the hologram shown in figure. 6.3a. Since these holograms are recorded in an off-axis configuration, the real and virtual reconstructions of the object and the undiffracted pattern are separated as shown in figure 6.3b. Figure. 6.3c shows the phase of the reconstructed object wave field, in the region marked in figure 6.3b as the area of inspection, before deformation. From the two reconstructed object wave fields obtained in this manner the reconstructed interference field is formed as explained below.

Let the numerically reconstructed object wave field be represented as:

$$\Gamma(x,y) = a(x,y) \exp[j\phi(x,y)] \tag{6.1}$$

where $a(x,y)$ is the amplitude and $\phi(x,y)$ is the estimated phase of the object wave field. Since we have the reconstructed object wave fields corresponding to the two states of the object, which we can represent as, $\Gamma_1(x,y)$ and $\Gamma_2(x,y)$, then the *reconstructed interference field* can be formed as:

$$
\begin{aligned}
A(x,y) &= \Gamma_2(x,y) \times \Gamma_1^*(x,y) \\
&= a_1(x,y)a_2(x,y) \exp\{j[\phi_2(x,y) - \phi_1(x,y)]\} \\
&= b(x,y) \exp[j\Delta\phi(x,y)]
\end{aligned}
\tag{6.2}
$$

where $\phi_1(x,y)$, $\phi_2(x,y)$ are the phases of the object waves before and after deformation, respectively.

Fig. 6.3d shows the real part of the reconstructed interference field corresponding to the loading of a circularly clamped object (of 6 cm in diameter), located at a distance of 110 cm from the CCD camera (SONY XCL-U1000, 1628×1236).

6.2.1 Simultaneous Measurement of Displacement, Strain, and Curvature

In chapters 2, 3, 4, and 5 it has been shown how to estimate the phase of the reconstructed interference fields (Eq. (6.2)) using, respectively, MLE, DCFT, HIM and CPF methods.
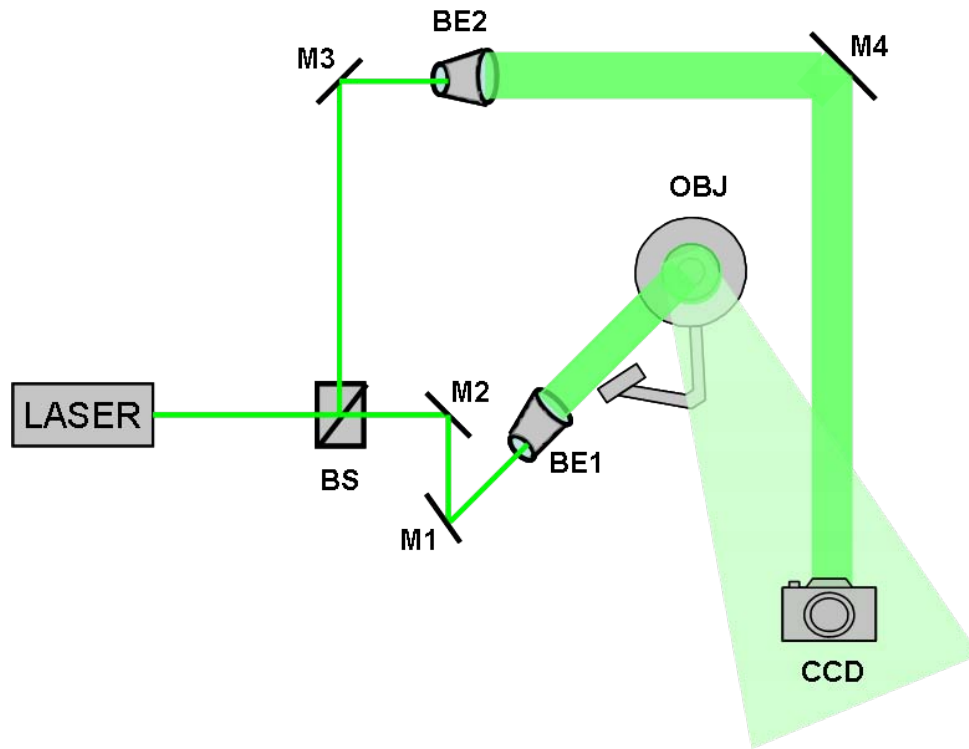
Fig. 6.1: Schematic of the experimental setup of an off-axis digital holographic interferometer (BS: Beam Splitter, BE: Beam Expander, M: Mirror, CCD: CCD Camera, OBJ: Object)
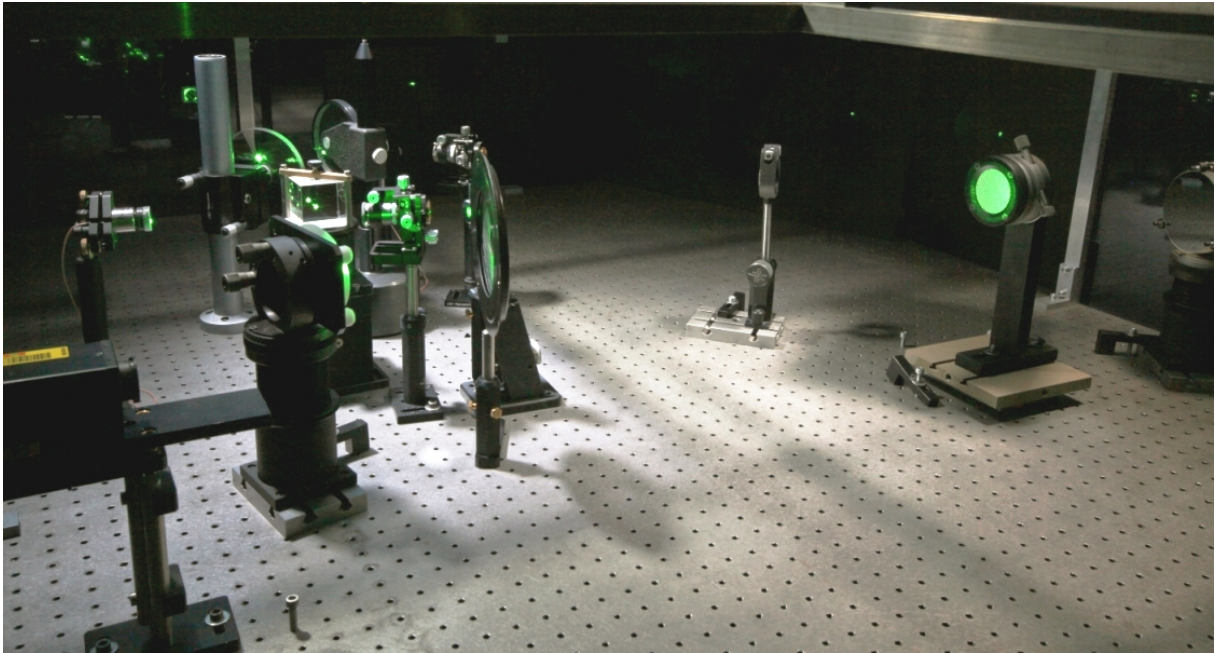
Fig. 6.2: Image of the experimental setup of an off-axis digital holographic interferometer in our laboratory

(a)

(b)

(c)

(d)
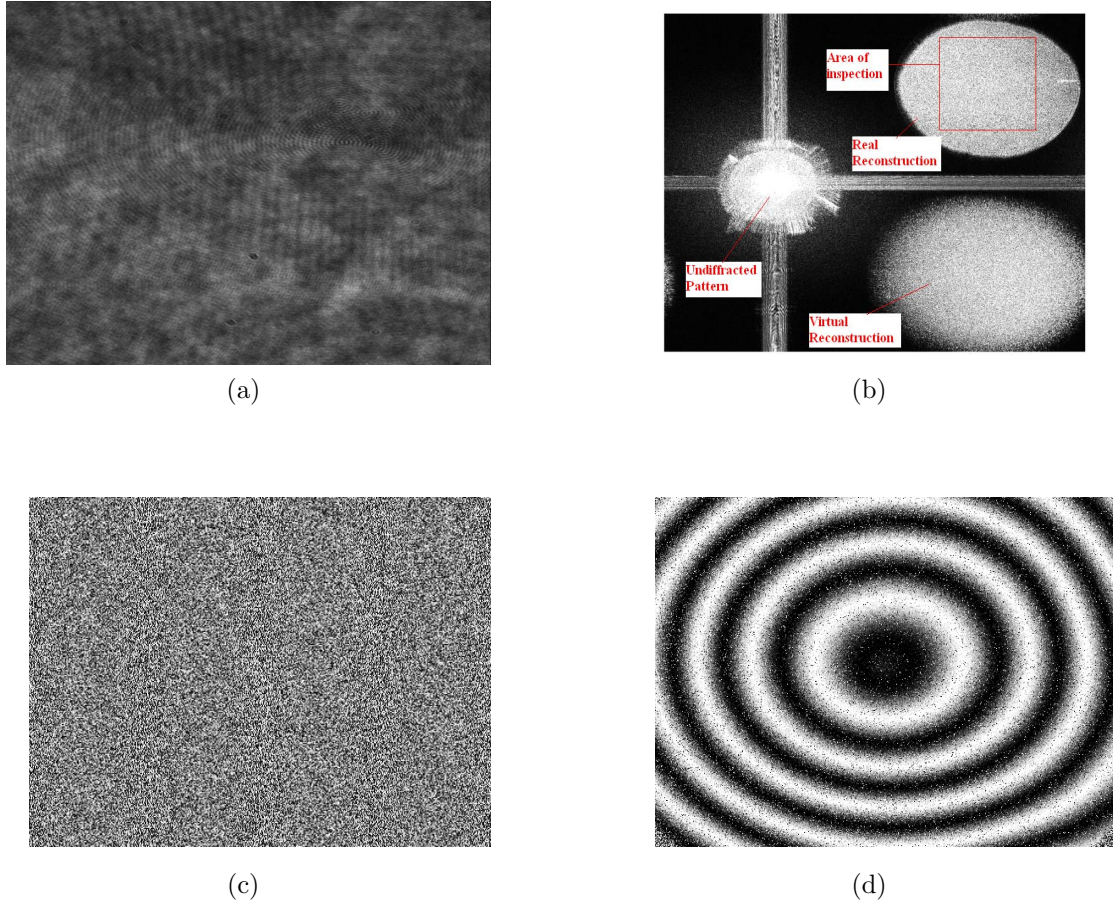
Fig. 6.3: (a) Experimentally recorded digital hologram in an off-axis configuration, (b) Amplitude of the numerically reconstructed hologram using discrete Fresnel transform, (c) Phase, in the area of inspection marked in Fig. 6.3b, of the reconstructed object wave field before deformation, (d) Real part of the reconstructed interference field, formed using equation (6.2), corresponding to the loading of a circularly clamped object,

Estimation of the first-order derivative of phase using DCFT and CPF have also been discussed in chapters 3 and 5 respectively. In holographic interferometry, the information on displacement, strain, and curvature are respectively carried in the interference phase, its first-order and second-order derivatives [24]. Here we use HIM method to compute simultaneously all the three quantities. In HIM method, the data in each segment of the reconstructed interference field is approximated with a polynomial phase signal of order M, then we have:

$$g(x) = b(x) \exp\left[j \left(\sum_{q=0}^{M} a_q x^q \right) \right] + \eta(x) \tag{6.3}$$

The interference phase and its derivatives within each segment can then be calculated as:

$$\Delta\phi(x) = \qquad a_0 + a_1 x + a_2 x^2 + ... + a_M x^M \tag{6.4}$$

$$\frac{\partial \Delta\phi}{\partial x} = \qquad a_1 + 2a_2 x + 3a_3 x^2 + ... + M a_M x^{M-1} \tag{6.5}$$

$$\frac{\partial^2 \Delta\phi}{\partial x^2} = \quad 2a_2 + 6a_3 x + 12a_4 x^2 + ... + M(M-1)a_M x^{M-2} \tag{6.6}$$

Equations (6.3)-(6.6) suggest that the problem of the estimation of phase and its derivatives from the reconstructed interference field is equivalent to the problem of estimating the parameters $\{a_q\}$ in Eq. (6.3). These parameters can be estimated as explained in chapter 4.

A simulated fringe pattern (corresponding to the simulated reconstructed interference field) with a signal-to-noise ratio (SNR) of 30 dB is shown in Fig. 6.4. This pattern of dimensions 256×256 pixels (i.e. N=256) is generated using the AWGN function in MATLAB, which adds additive white Gaussian noise of a specified level to the actual signal. Applying the HIMs based estimation procedure as explained in chapter 4, by segmenting each column of the signal into four pieces ($N_w = 4$) and approximating the data in each segment with a fourth-order polynomial phase signal ($M = 4$), interference phase and its first and second-order derivatives along y-axis are computed. We have used here the iterative frequency estimation by interpolation on Fourier coefficients (IFEIF) algorithm [89] for the estimation of single-tone signals' frequencies that are formed by the HIM operator.

Figs. 6.5a, 6.5c and 6.5e shows the 3-D mesh plots of the estimated continuous distributions of the interference phase and its first and second-order derivatives respectively. The corresponding wrapped distributions, generated for the purpose of illustration are shown in Figs. 6.5b, 6.5d and 6.5f respectively. In order to evaluate the performance of the proposed method in terms of the accuracy of estimation, the root mean square errors (RMSE) in the estimation of phase and its derivatives by the HIMs method are calculated. Since in simulation we know the actual noise-free phase distribution, its first and second order derivatives are calculated by numerical differentiation and this information is used
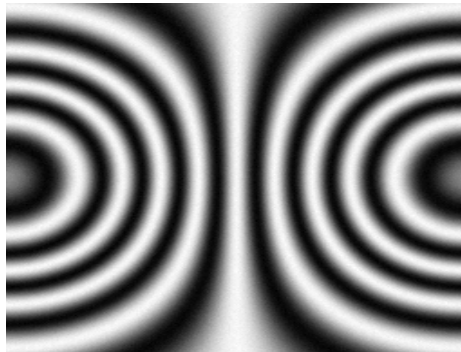
Fig. 6.4: Simulated fringe pattern ($SNR = 30\,dB$, 256×256).
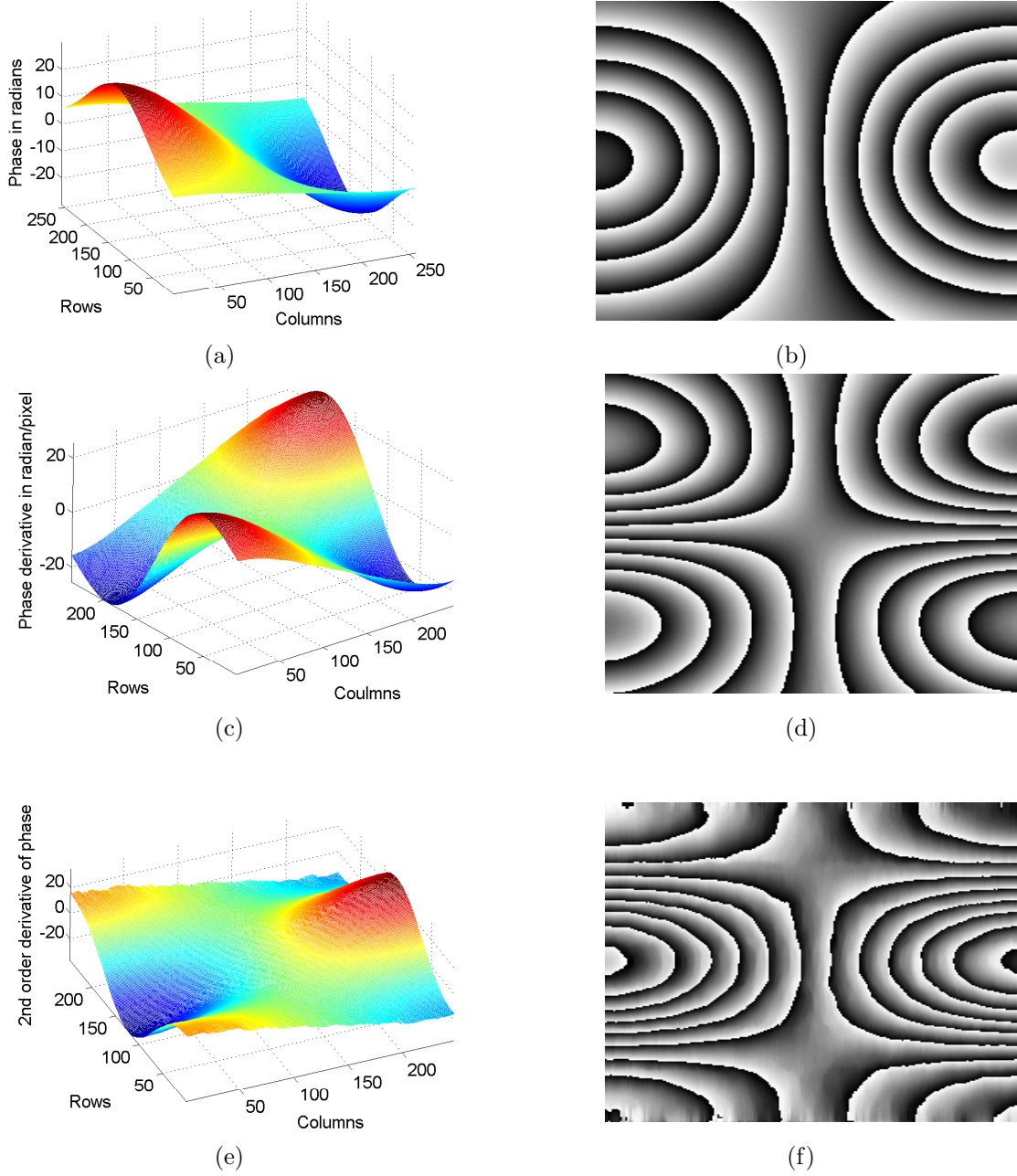
Fig. 6.5: 3D mesh plots of the estimated distributions from Fig. 6.4 with the HIM method corresponding to (a), (c), and (e) interference phase, first-order derivative of phase, and second-order derivative of phase, respectively. (b), (d), and (f) wrapped phase maps generated for the purpose of illustration corresponding to (a), (c) and (e) respectively.

to calculate RMSE values that are found to be $7.2 \times 10^{-3} radians$, $1.4 \times 10^{-3} radians/pixel$ and $1.3 \times 10^{-4} radians/pixel^2$ respectively.

(a)

(b)

(c)

(d)
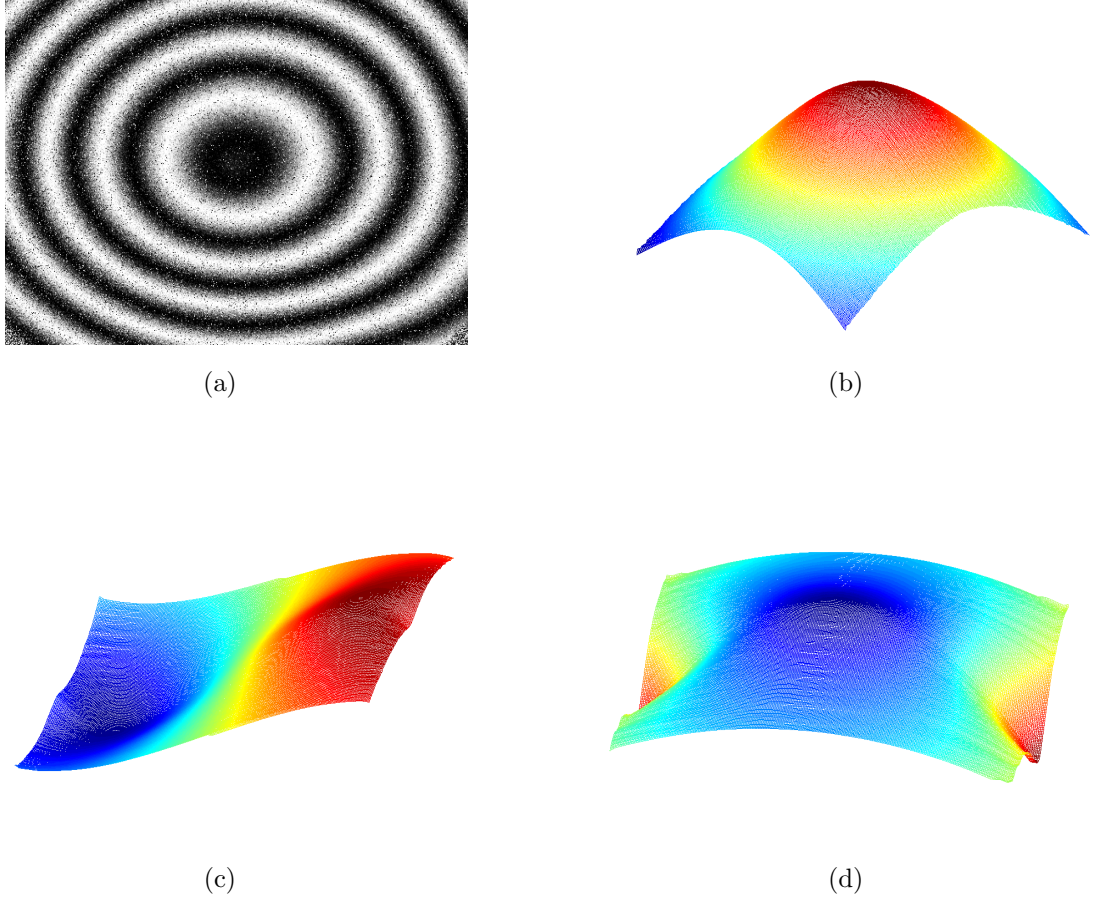
Fig. 6.6: (a) Fringe pattern obtained in a DHI experiment corresponding to the central loading of a circularly clamped object (256×256), (b), (c), and (d) 3D mesh plots of the estimated distributions from (a) with the HIM method corresponding to out-of-plane displacement, slope, and curvature, respectively.

Experimental results shown in Fig. 6.6 substantiate the potential utility of the HIM method for simultaneously estimating the displacement, slope and curvature in digital holographic interferometry. Fig. 6.6a shows the real part of the reconstructed interference field corresponding to the central loading of a circularly clamped object. Figs. 6.6b- 6.6d show the 3-D mesh plots of the estimated continuous distributions of the displacement, slope, and curvature, respectively. The corresponding wrapped phase maps generated for the purpose of illustration are shown in Figs. 6.7a, 6.7c and 6.7e respectively. It can be noticed that, since the method fits polynomials with the assumption that the phase distribution that is being estimated does not contain abrupt variations such as discontinuities, the estimated phase maps are always smooth and are free from noise/spurious jumps. For the sake of comparison, direct results obtained by the conventional procedure of digital shifting and conjugate multiplication are shown in Figs. 6.7b, 6.7d and 6.7f. As can be
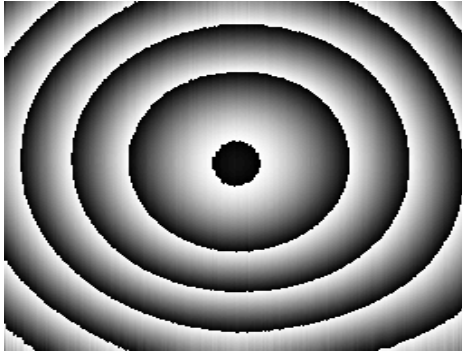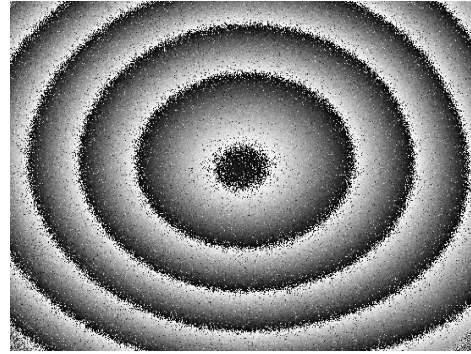
(a)   (b)
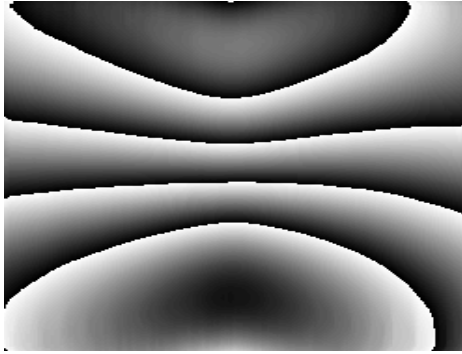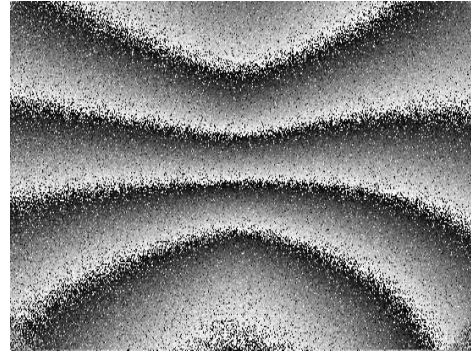
(c)   (d)
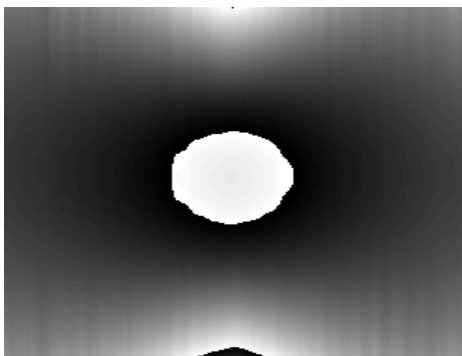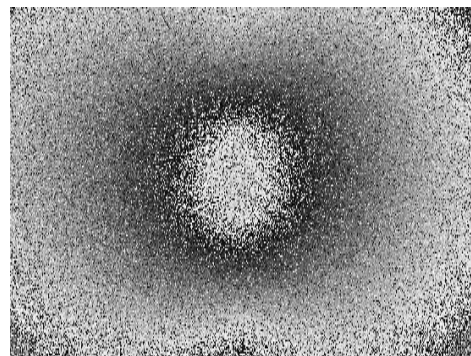
(e)   (f)

Fig. 6.7: (a), (c), (e) wrapped maps generated for the purpose of illustration corresponding to Fig. 6.6b, 6.6c and 6.6d respectively, (b), (d), and (f) phase and its derivatives calculated using conventional direct differentiation approach shown for the purpose of comparison.

seen from the figures, the direct calculation method provides noisy wrapped phase maps and thereby necessitates filtering and unwrapping procedures to get continuous distributions whereas the HIM method directly provides the unwrapped estimates. It has taken only 0.8 seconds for computing all the three distributions.

Note that this way of computing strain and curvature in DHI using HIM method has several important and unique advantages. As mentioned in the introduction chapter, most commonly followed ways of measuring strain are: (1) Using the specific interferometric configuration such as shearography and moiré based, which provides directly the displacement derivative fringes [21–32]. In this case, one can use any fringe analysis method, that is commonly used for phase estimation, to obtain information about strain. But if one would like to get information corresponding to displacement or curvature - one has to change the interferometric configuration and make another measurement. This procedure is having an associated disadvantage that it is not possible to get all the information in a single measurement. In reality it is difficult to unload the object and identically reload it multiple times. (2) An alternative approach is to use the same interferometric configuration which produces fringe patterns whose phase carries information on displacement but adopting a specialized fringe analysis method [18–20, 55]. These specialized methods directly provide an estimation of the phase derivative. In this case, one has to change the analysis method that is used for obtaining different quantities of interest. It means that, one has to apply multiple analysis methods for obtaining information on displacement, strain and curvature. (3) Another most commonly followed approach, at least while using DHI, is to approximate the phase differentiation operation with that of digital shifting and multiplying with a conjugated version of a complex amplitude of the reconstructed interference field [33–38]. However, to have good sensitivity, the amount of shifting has to be more and it results in the reduction of resolution and some times gross errors due the rapid variations in phase or its derivative. Moreover, the first and second-order derivatives calculated in this manner are usually contaminated with severe noise (in addition to being wrapped), thereby necessitating the application of different filtering schemes such as those based on average filter, sine/cosine transform and short-time Fourier transform have been proposed [37, 38]. But the iterative filtering operations are computationally demanding and need to be carefully implemented so as not to smear dense fringes.

In view of the drawbacks/difficulties associated with the above approaches, HIM method possess a salient feature of being able to provide simultaneously information of all the three quantities in a single interferometric configuration. That too, at no cost of resolution and additional computational complexity. In addition, there is no necessity of using any filtering and complicated unwrapping algorithms.

6.3 Classical Holographic Interferometry

Until now all the methods presented in this thesis have been introduced in the context of the analysis of reconstructed interference fields in DHI. Here we show how these methods can be applied in classical holographic interferometry and the advantages that they provide in comparison with the benchmark methods. A simple mathematical representation

of the recorded holographic interference fringe pattern is given by

$$I(x, y) = I_0 \left\{ 1 + \gamma(x, y) \cos \left[\phi(x, y) \right] \right\} \tag{6.7}$$

where I, I_0, γ and ϕ represent the recorded intensity, background intensity, fringe visibility and the phase term respectively, at the pixel (x, y). While employing spatial analysis techniques, the phase in the argument of the cosine function is commonly expressed as $\phi(x, y) = \phi_c(x, y) + \phi_d(x, y)$ where $\phi_c(x, y)$ corresponds to the phase of the carrier added and $\phi_d(x, y)$ represents the deformation phase or the interference phase to be estimated. Even when the spatial carrier is added, it is not uncommon to be confronted with the fringe patterns similar to the one shown in Fig. 6.8a. This kind of a pattern represents a non-stationary signal in which the parameters associated with it, especially the frequency, vary considerably from one location to the other. As mentioned in introduction chapter, conventional analysis techniques are not best suited to be applied for accurate phase estimation of these patterns. The analytic version of this kind of signals is referred to as polynomial phase signals, and parametric estimation based on HIM can provide accurate results. Eliminating the d.c. term from Eq.(6.7) using high-pass filtering results in:

$$I'(x, y) = a(x, y) \cos \left[\phi(x, y) \right] \tag{6.8}$$

Note that with the help of any of the fringe normalization techniques [96–98], from Eq.(6.7) we can even get directly:

$$I'(x, y) = \cos \left[\phi(x, y) \right] \tag{6.9}$$

Now we apply real to analytic signal conversion [99] on the Eq.(6.8) or 6.9 to obtain the analytic signal of the form:

$$z(x, y) = a(x, y) \exp \left[j\phi(x, y) \right] \tag{6.10}$$

Now one option could be to calculate phase from $z(x, y)$ using arctan function. However, as is in the case of DHI, phase calculated in this manner is often noisy and on top of it, it is bound to be wrapped. The reason for phase map calculated directly from $z(x, y)$ to be noisy is that the latter contains noise inherited from the fringe pattern. Thus it is appropriate to represent the analytic signal of the fringe pattern as:

$$z(x, y) = a(x, y) \exp \left[j\phi(x, y) \right] + \eta(x, y) \tag{6.11}$$

where η represents the noise term. The above equation is identical in form to that of the reconstructed interference field in DHI (Eq.(6.2)). The interference phase can thus be accurately estimated using the HIM method or the other methods as presented earlier.

Fig. 6.10a shows the comparison of error plots when the phase along a row is estimated with the HIM method by approximating the phase of the fringe pattern with polynomials of different orders (at SNR=30 dB). We have performed error analysis at different SNRs with fourth order polynomial approximation, results of which are shown in Fig. 6.10b. Fig. 6.8a shows the image of a simulated fringe pattern. The discrete time analytic signal of the fringe pattern is computed using the Hilbert transform [99]. Then the HIM method

Tab. 6.1: Performance comparison of HIM and WFR methods

Method	RMSE	Time (in Sec)
WFR	0.0235	399.4
HIM	0.0117	2.8

is used for estimating directly the unwrapped phase distribution. In these simulations, accurate phase estimation is accomplished by using the fourth-order polynomial phase approximation over the entire row. Fig. 6.8b shows the profile of the estimated phase along the middle row, after eliminating the carrier phase. Fig. 6.8c shows the error plot. 3-D plot of the estimated phase over all the rows is shown in Fig. 6.8d. As is clear from the previous figure, phase stitching is needed to obtain a continuous 2-D phase distribution. Fig. 6.8e shows the 3D plot of the interference phase estimated with the HIM method after phase stitching. Error in estimation is shown in Fig. 6.8f.

Note that RPT method [4] also provides directly the unwrapped phase distribution from the normalized fringe pattern (Eq.(6.9)); if Eq.(6.10) is the input, both RPT of Servin [67] and windowed Fourier ridge (WFR) of Kemao [40, 68] will produce accurate phase estimation. In [100] Kemao et al. have provided an elegant comparative analysis of five effective wrapped phase filtering techniques, which included RPT and WFR. Here we compare the results of the HIM method with WFR. Fig. 6.9 shows 3-D mesh plots of error distributions when continuous phase distribution of the pattern shown in Fig. 6.8a is estimated with both the methods. As is evident from Fig. 6.9, WFR method produces results with relatively large errors near the edges of the image. Although the HIM method shows to an extent a similar tendency, it produces relatively small errors. For example, if all pixels of the fringe pattern are considered, the root mean square errors (RMSE) produced by WFR and HIM methods are given by 0.0794 and 0.0206, respectively. For this reason, 10 rows from both top and bottom and 10 columns from both left and right boundaries of the estimated phase are not considered (size of the window used in WFR algorithm is 10×10) either while calculating the RMSE values listed in Table 6.1 or displaying the error plot in Fig. 6.9. The RMSE and computational cost for HAF and WFR methods are listed in Table 6.1. It is evident that the HIM method provides accurate results with relatively less computational time.

The experimental results shown in Fig. 6.11 substantiate the applicability of this method for phase estimation in classical holographic interferometry. For the sake of comparison, Fig. 6.11d and Fig. 6.11e show, respectively, the phase map calculated from the analytic signal using arctan function and the wrapped phase generated from the estimated continuous phase (Fig. 6.11c) obtained using the proposed method.

6.4 Conclusions

This chapter has demonstrated the application of the HIM method for the simultaneous measurement of displacement, slope and curvature in digital holographic interferometry.

With the HIM method, accurate and direct estimation of the unwrapped distributions corresponding to the interference phase and its derivatives are obtained in a computationally efficient manner. By modeling the reconstructed interference field as a piecewise polynomial phase signal, the HIM method has made possible the simultaneous computation of phase and its derivatives within a single interferometric configuration. In addition to providing noise-free results, the propagation/accumulation of errors while calculating higher-order derivatives from the lower-order ones is thus prevented. The method with its advantages with respect to the accuracy of estimation and computational efficiency will find great utility in non-destructive testing. The usefulness of the method in analyzing fringe patterns recorded in classical holographic interferometry is also demonstrated.
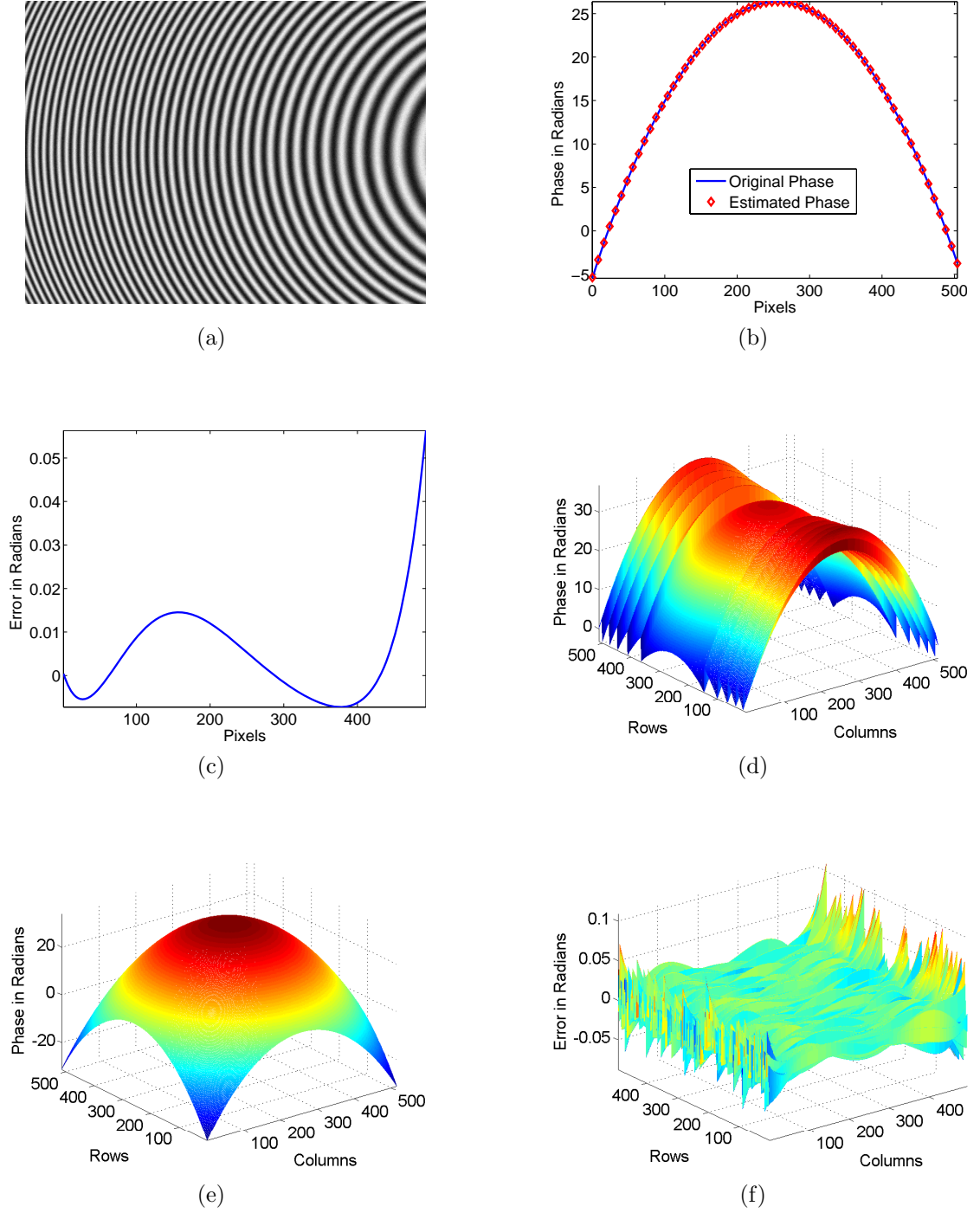
Fig. 6.8: (a) Simulated fringe pattern at SNR of $30\,dB$, (b) Phase estimated using the HIM method along the middle row after subtracting the carrier phase, (c) Error plot, (d) 3-D plot of the estimated phase along all rows (e) 3-D plot of the resulting phase map after phase stitching, (f) 3-D plot of the error distribution.

65
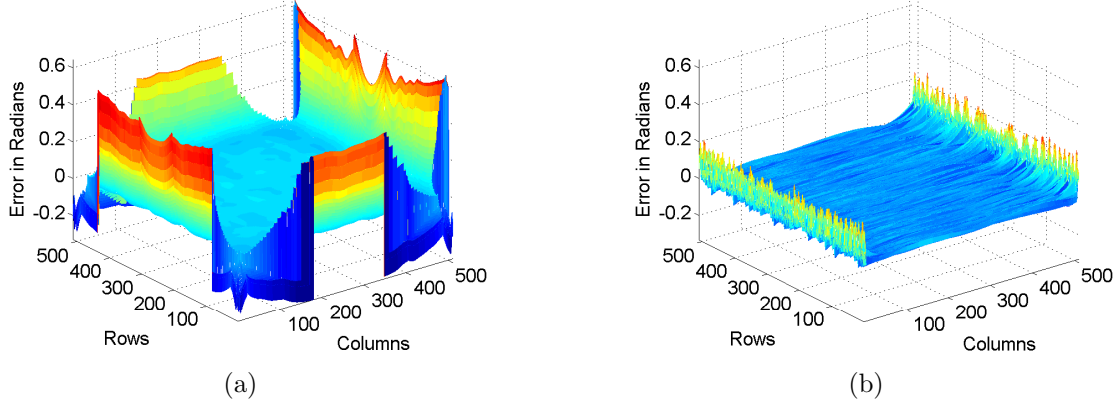
Fig. 6.9: Error plots when continuous phase distribution of Fig. 6.8a is estimated with (a) WFR method (b) HIM method
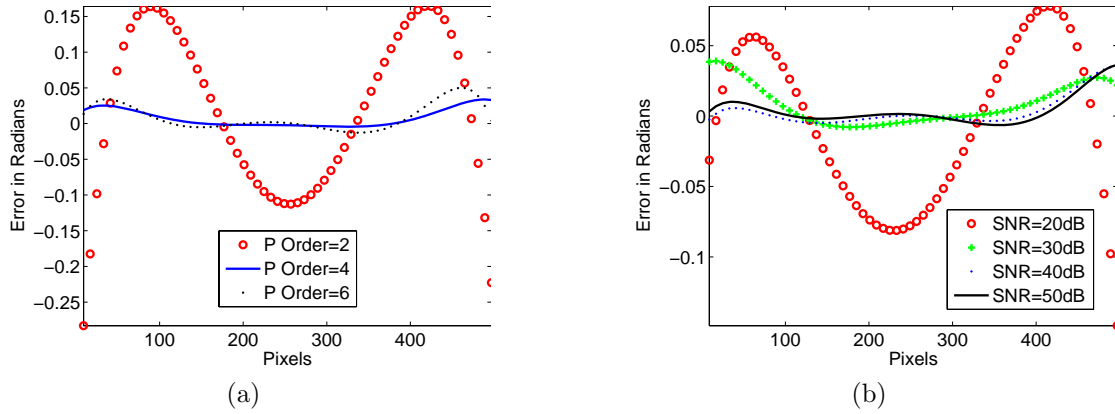
Fig. 6.10: Error plots when (a) Approximated with different orders of polynomials at SNR of 30 dB (b) Approximated with a 4th order polynomial at different levels of SNR
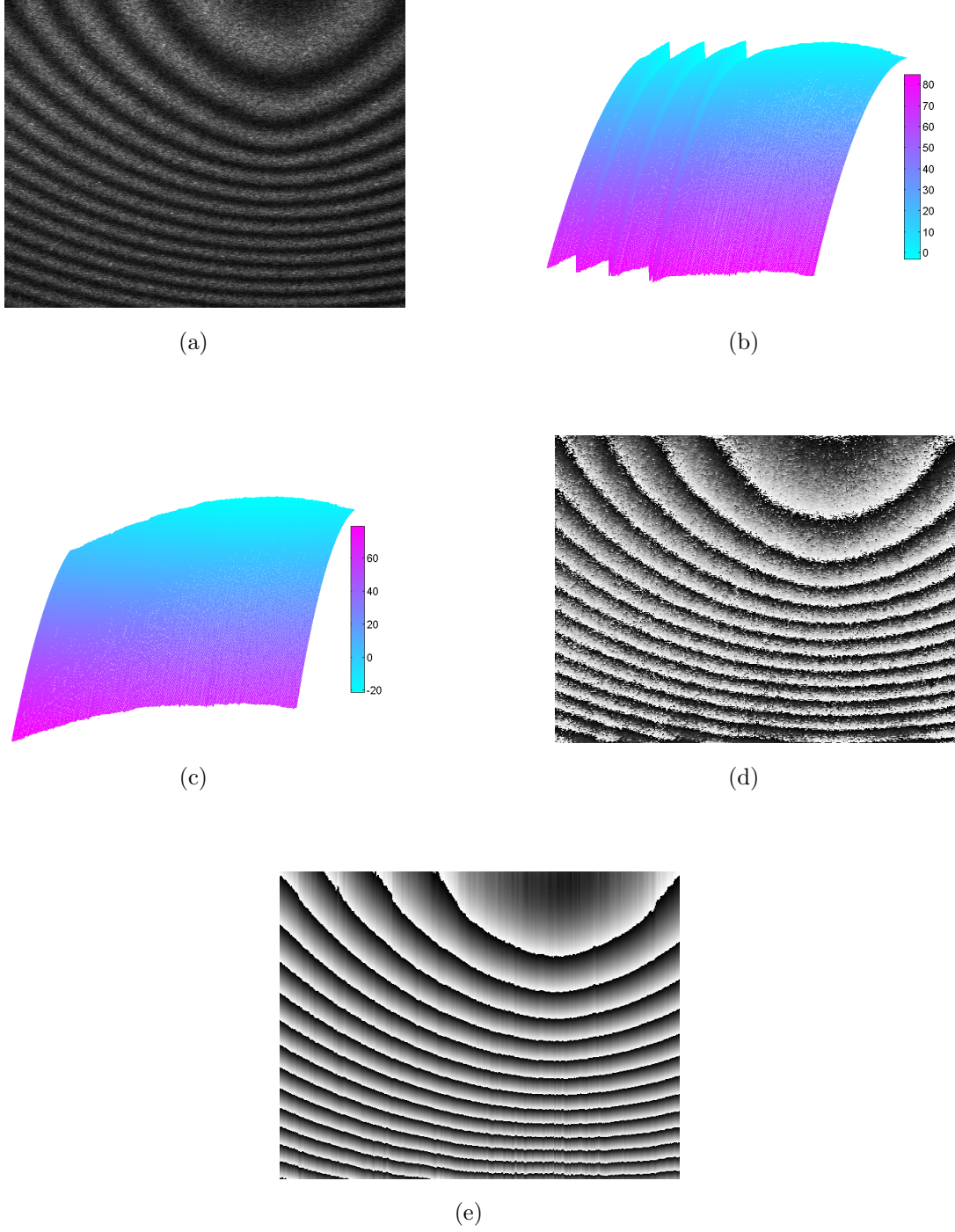
Fig. 6.11: (a) Experimentally recorded holographic fringe pattern, (b) 3-D plot of the estimated phase along all rows using HIM method, (c) 3-D plot of the resulting phase map after phase stitching, (d) Phase calculated directly from the analytic signal using *arctan* function, (e) Generated wrapped phase map from the continuous phase distribution in Fig.4c.

Chapter 7

Applications in Fringe Projection Techniques

7.1 Introduction

This chapter presents few applications of HIM method in fringe projection techniques. In particular, three-dimensional shape measurement of objects, time evolution study of deformations, and strain evolution measurements are performed with the HIM method. A general introduction to the fringe projection techniques and their importance in optical metrology are presented in the next section. In the section 7.3, HIM based profilometry is presented. HIM methods ability to provide directly an accurate and unwrapped estimation of the phase or its derivative in an extremely faster manner has motivated to explore its potential use in performing time evolution studies. Section 7.4 presents the results of time evolution measurement of deformation with the HIM method in fringe projection technique. Results of the strain evolution measurements carried out with the HIM method are presented in section 7.5. The results of these experiments indicate a salient feature of HIM method that it avoids the necessity of using a complex three-dimensional phase unwrapping algorithm in order to get a movie of the measured deformation or strain.

7.2 Fringe Projection Techniques

During recent years, the use of fringe projection techniques for generating three-dimensional (3D) surface information has become one of the most active research areas in optical metrology. Its *applications* range from measuring the 3D shape of MEMS components to the measurement of flatness of large panels ($2.5\ m \times .45\ m$). The technique has found various applications in diverse fields: biomedical applications such as 3D intra-oral dental measurements, non-invasive 3D imaging and monitoring of vascular wall deformations, human body shape measurement for shape guided radiotherapy treatment, lower back deformation measurement, detection and monitoring of scoliosis, inspection of wounds and skin topography measurement for use in cosmetology; industrial and scientific applications such as characterization of MEMS components, vibration analysis, refractometry, global

measurement of free surface deformations, local wall thickness measurement of forced sheet metals, corrosion analysis, measurement of surface roughness, reverse engineering, quality control of printed circuit board manufacturing and heat-flow visualization; kinematics applications such as measuring the shape and position of a moving object/creature and the study of kinematical parameters of dragonfly in free flight; biometric identification applications such as 3D face reconstruction for the development of robust face recognition systems; cultural heritage and preservation etc.

One of the outstanding features of some of the fringe projection techniques is their ability to provide high-resolution, whole-field 3D reconstruction of objects in a non-contact manner at *video frame rates*. This feature has backed the technique to pervade new areas of applications such as security systems, gaming and virtual reality. To gain insights into the series of contributions that have helped in unfolding the technique to acquire this feature, refer to the review articles by Song Zhang [101], and Xianyu Su et al. [102].

A typical *fringe projection profilometry system* is shown in figure 7.1. It consists of a projection unit, an image acquisition unit and a processing/analysis unit. Measurement of shape through fringe projection techniques involves (1) projecting a structured pattern (usually a sinusoidal fringe pattern) onto the object surface, (2) recording the image of the fringe pattern that is phase modulated by the object height distribution, (3) calculating the phase modulation by analyzing the image with one of the fringe analysis techniques (such as Fourier transform method, phase stepping and spatial phase detection methods-most of them generate wrapped phase distribution) (4) using a suitable phase unwrapping algorithm to get continuous phase distribution which is proportional to the object height variations, and finally (5) calibrating the system for mapping the unwrapped phase distribution to real world 3-D co-ordinates. Figure 7.2 shows the flowchart that depicts different steps involved in the measurement of height distribution of an object using the fringe projection technique and the role of each step. A pictorial representation of the same with more details is shown in figure 7.3.

During the last three decades, fringe projection techniques have developed tremendously due to the contribution of large number of researchers and the *developments can be broadly categorized* as follows: design or structure of the pattern used for projection, method of generating and projecting the patterns, study of errors caused by the equipment used and proposing possible corrections, developing new fringe analysis methods to extract underlying phase distribution, improving existing fringe analysis methods, phase unwrapping algorithms, calibration techniques, scale of measurement (micro/medium/large objects), state of the object (static/dynamic) and exploring the use of these techniques in diverse areas (different applications). Though the measurement process with the fringe projection techniques has several steps, and in each step there exists several variants, these techniques are classified mainly depending on the type of fringe analysis method that is employed. For example, based on the particular fringe analysis method used in the measurement, fringe projection techniques are classified as phase stepping profilometry (PSP), Fourier transform profilometry (FTP), wavelet transform profilometry (WTP), spatial filtering profilometry (SFP) etc.

Fringe analysis is a key task and which significantly influences the overall performance of
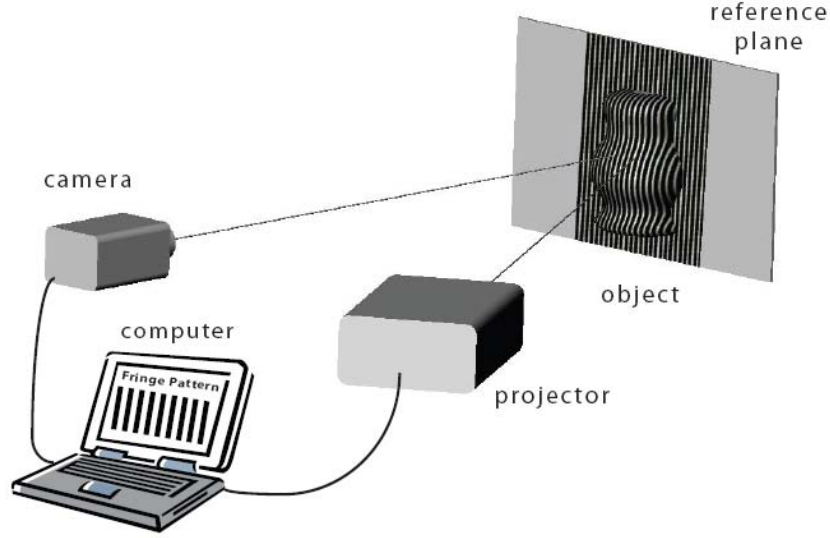
Fig. 7.1: Fringe projection profilometry system

the fringe projection profilometry system in terms of number of images required, resolution and accuracy of measurement, computational requirements etc. Over the last three decades, several fringe analysis methods have been developed. Broadly they can be categorized as spatial and temporal analysis methods. Their efficient and successful application require the presence of a sufficiently high-frequency spatial carrier for spatial methods, and acquisition of a number of images by projecting phase-shifted fringe patterns for temporal methods. Some of the fringe analysis methods introduced in the context of fringe projection profilometry are Fourier transform method and numerous extensions of it [103–108], interpolated Fourier transform [109], regressive Fourier transform [**?**, 111], dilating Gabor transform [41], windowed Fourier transform [3, 40], multi-scale windowed Fourier transform [112, 113], one-dimensional and two-dimensional Wavelet transforms [45–48], S-transform [114], discrete-cosine transform [115], modified Hilbert transform [116], analysis using inverse cosine function [117], neural networks [118, 119], phase locked loop [120–123], regularized phase tracker [124, 125], spatial phase detection [126–128], and phase-shifting methods [129–133]. Article by Lei Huang et al. [134] provides a comparative analysis among some of the most commonly used fringe analysis methods.

The recovered/estimated phase from the the deformed fringe pattern by using most of the aforementioned fringe analysis methods is mathematically limited to the interval $[-\pi, +\pi]$ corresponding to the principal value of arctan function. In general, the true phase may range over an interval greater than 2π in which case the recovered phase contains artificial discontinuities. The process of determining the unknown integral multiple of 2π to be added at each pixel of the wrapped phase map to make it continuous by removing the artificial 2π discontinuities is referred to as *phase unwrapping*. Normal phase unwrapping is carried out by comparing the phase at neighboring pixels and adding or subtracting 2π to bring the relative phase between the two pixels into the range of $-\pi$ to $+\pi$. Thus, phase unwrapping is a trivial task if the wrapped phase map is ideal. However, in real measurements, the presence of shadows, low fringe modulations, non-uniform

71

Projection & Acquisition

Generating and projecting the patterns onto the object & capturing their images

Fringe Analysis

Using some fringe analysis technique to calculate the underlying phase distribution of the acquired fringe images

Phase Unwrapping

Obtaining the continuous phase distribution from the wrapped phase map

Calibration

Conversion from image co-ordinates to real world co-ordinates and conversion from unwrapped phase map to absolute height map

Fig. 7.2: Flow chart

reflectivities of the object surface, fringe discontinuities, noise etc. makes phase unwrapping difficult and path dependent. Several advanced unwrapping algorithms have been developed and some of them are: Goldstein's algorithm [11], ZπM algorithm [135], temporal phase unwrapping algorithm [136], fringe frequency analysis based algorithm [137], Fourier transform profilometry based [138], region growing phase unwrapping [12], local histogram based phase unwrapping [13], improved noise immune phase unwrapping [14], regularized phase tracking [15], flood fill [16], PEARLS (phase estimation using adaptive regularization based on local smoothing) [139], and multilevel quality guided phase unwrapping algorithm [17]. Some review articles on unwrapping include [140–143]. Zappa et al. [144] performed a comparison of the performance of eight unwrapping algorithms (Goldstein's, quality guided path following, Mask cut, Flynn's, multi-grid, weighted multi-grid, preconditioned conjugate gradient and minimum Lp-norm algorithm) in the context of measuring 3D shape information using Fourier transform profilometry. In the case of dynamic/real-time 3D shape measurement, a stack of 2D wrapped phase maps obtained at different time instants needs to be unwrapped, for which a three-dimensional phase
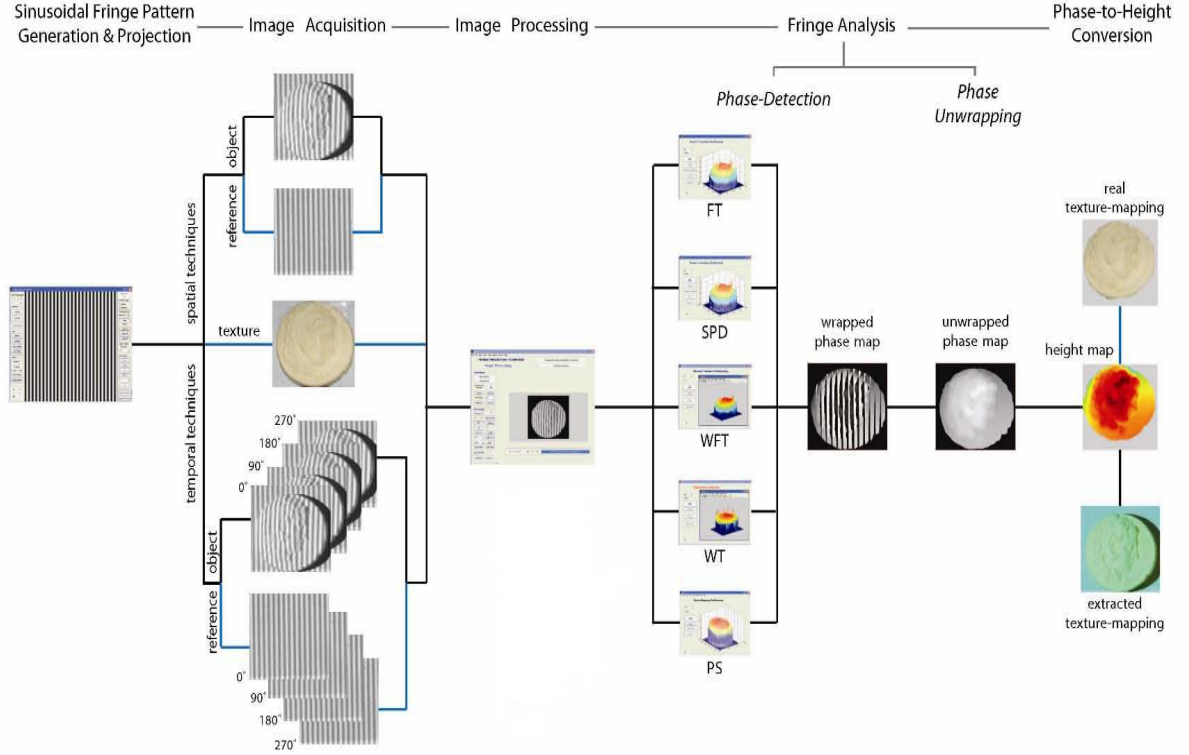
Fig. 7.3: Work-flow in fringe projection profilometry

unwrapping algorithm is required. For a detailed discussion on 3D phase unwrapping, refer to the review article on "Dynamic 3D shape measurement" by Xianyu Su and Qican Zhang [102].

More information about fringe projection techniques and their applications are outlined in [145].

In this chapter, high-order instantaneous moments based profilometry is developed for 3D shape measurement in fringe projection. The HIM method is capable of directly providing the unwrapped phase estimates with good computational efficiency. The theory of the HIM profilometry along with the simulation and experimental results is presented in the next section.

7.3 High-order Instantaneous Moments Profilometry

For a carrier fringe pattern projected on a reference plane or flat surface, the recorded reference fringe pattern by the CCD camera is expressed as

$$I_1(x,y) = a_1(x,y) + b_1(x,y)\cos(\omega_0 x) + \eta_1(x,y) \tag{7.1}$$

where ω_0 is the carrier frequency, $I_1(x,y)$ is the recorded intensity, $a_1(x,y)$ is the background intensity or the d.c. term, $b_1(x,y)$ is the fringe amplitude, $\eta_1(x,y)$ is the noise term

and x and y refer to the pixels along horizontal and vertical directions and are equivalent to columns and rows of the $N \times N$ image. Equation 7.1 can be equivalently written as

$$I_1(x, y) = a_1(x, y) + \frac{1}{2} b_1(x, y) \exp[-j\omega_0 x]$$
$$+ \frac{1}{2} b_1(x, y) \exp[j\omega_0 x] + \eta_1(x, y) \tag{7.2}$$

From equation 7.2, it is clear that the spectrum of $I_1(x, y)$ has contribution from $a_1(x, y)$ around the d.c. or low frequencies and around $-\omega_0$ and ω_0 due to the contribution from the second and third terms in equation 7.2. Similarly, for a carrier fringe pattern projected on an object's surface, the fringe pattern recorded by the CCD camera is expressed as

$$I_2(x, y) = a_2(x, y) + b_2(x, y) \cos[\omega_0 x + \phi(x, y)] + \eta_2(x, y) \tag{7.3}$$

or equivalently,

$$I_2(x, y) = a_2(x, y) + \frac{1}{2} b_2(x, y) \exp[-j(\omega_0 x + \phi(x, y))]$$
$$+ \frac{1}{2} b_2(x, y) \exp[j(\omega_0 x + \phi(x, y))] + \eta_2(x, y) \tag{7.4}$$

where $\phi(x, y)$ is the phase term that contains information about the object's surface profile. Filtering the spectrum of $I_1(x, y)$ and $I_2(x, y)$ around ω_0 thereby removing the contribution of d.c. terms $a_1(x, y)$ and $a_2(x, y)$ and the negative part of the spectrum , we obtain

$$I_1'(x, y) = b_1(x, y) \exp[j\omega_0 x] + \eta_1'(x, y) \tag{7.5}$$

$$I_2'(x, y) = b_2(x, y) \exp[j(\omega_0 x + \phi(x, y))] + \eta_2'(x, y) \tag{7.6}$$

Multiplying the complex conjugate of $I_1'(x, y)$ with $I_2'(x, y)$, we have

$$A(x, y) = I_2'(x, y) I_1'^*(x, y) \tag{7.7}$$

which can be approximated as

$$A(x, y) = b(x, y) \exp[j\phi(x, y)] + \eta(x, y) \tag{7.8}$$

where '*' denotes the complex conjugate, $b(x, y) = b_1(x, y) b_2(x, y)$ and $\eta(x, y)$ is the noise term. The above equation is identical in form to that of the reconstructed interference filed in DHI (equation 6.2). The phase modulation or equivalently the 3D shape information of the object can thus be accurately estimated using the HIM method by following the procedure outlined in chapter 4.

A reference fringe pattern (size 256×256) corresponding to a planar surface was simulated at signal to noise ratio (SNR) of 20 dB as shown in figure 7.4a. 'PEAKS' function of MATLAB (version 7.8.0, R2009a) was used to generate the original phase distribution in radians as shown in figure 7.4b. The fringe pattern phase modulated by the phase distribution is shown in figure 7.4c. The estimated phase in radians obtained by following
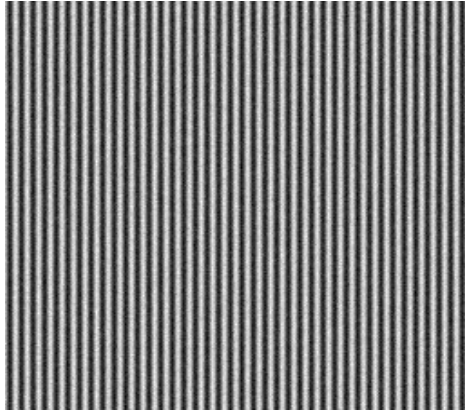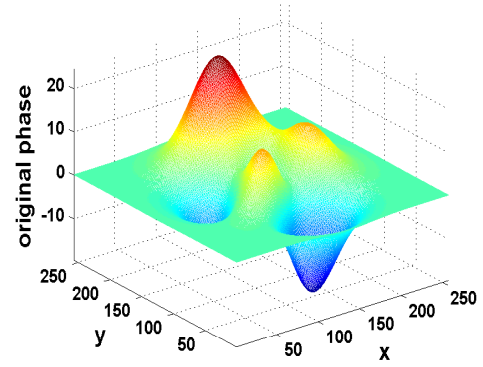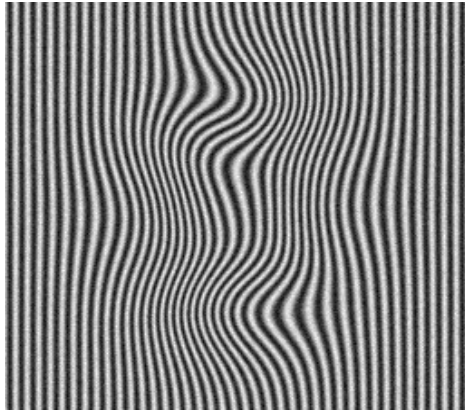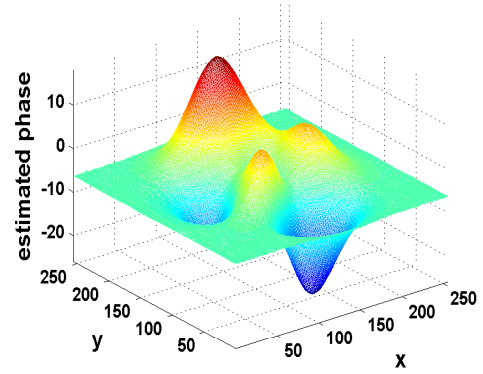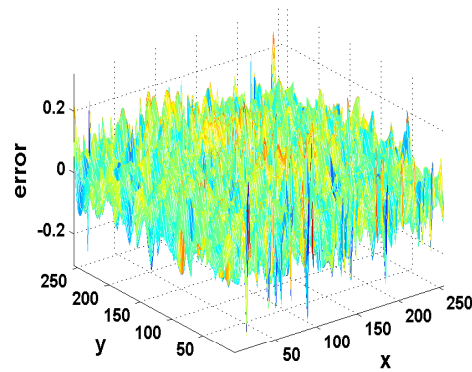
Fig. 7.4: (a) Reference fringe pattern. (b) Original phase as 'peaks' function in radians. (c) Fringe pattern phase modulated by the 'peaks' function. (d) Estimated phase in radians using the proposed method. (e) Error between original and estimated phase in radians.

the procedure mentioned above is shown in figure 7.4d. The error between the original and estimated phase in radians is shown in figure 7.4e. $N_w = 8$ and $M = 3$ were used for the analysis. The RMSE was 0.0553 radians. The computational time taken for the proposed method's implementation in MATLAB was 1.8 seconds on a 2.66 GHz Intel Core 2 Quad Processor machine with 3.23 GB random access memory.

To test the practical applicability of the HIM profilometry, a fringe projection experiment was conducted to measure the surface profile of the test object i.e. a mannequin. An EPSON EMP-710 projector was used to project fringes on a planar surface and the mannequin. An IMAGINGSOURCE DFK 31AF03 Firewire CCD camera was used to record the fringe patterns. The experimental set-up is shown in figure 7.5a. The procedure of generation, projection, recording and processing of the fringe patterns was automated with a MATLAB routine developed using the 'Image Acquisition Toolbox'. The recorded fringe pattern corresponding to the planar surface is shown in figure 7.5b. The recorded fringe pattern phase modulated by the mannequin's surface profile is shown in figure 7.5c. To neglect the regions with shadows, a portion of the recorded fringe pattern was cropped for analysis as shown in figure 7.5d. For the cropped image, the estimated phase distribution in radians using the HIM method is shown in figure 7.5e. The corresponding gray-scale image for the estimated phase is shown in figure 7.5f.

These simulation and experimental results validate the applicability of the HIM method in fringe projection for surface profiling. Simulation results show the method's potential for reliable phase estimation as indicated by low phase estimation errors in presence of noise. The low computational time for the method's implementation allows rapid processing of fringe patterns and makes the method suitable for real time applications. A major advantage of the HIM profilometry is that it avoids the need of the complex and time-consuming unwrapping procedures.

7.4 Time Evolution Study of Deformation

Dynamic 3D shape or deformation measurement is essential in the study of machine vision, hydrodynamics, high-speed rotation, deformation of material, stress analysis, deformation in impact, explosion process, biomedicine and in shape measurement during laser forming.

In this section we show the application of HIM method for the measurement of deformation in dynamic studies.

The following equation represents the intensity distributions of the stack of fringe patterns recorded in a typical fringe projection technique:

$$I(x, y, t) = a(x, y, t) + b(x, y, t) \cos [\omega_0 x + \phi(x, y, t)] + \eta(x, y, t) \tag{7.9}$$

where ω_0 is the carrier frequency, I is the recorded intensity, a is the background intensity or the d.c. term, b is the fringe amplitude, η is the noise term and x and y refer to the pixels along horizontal and vertical directions and are equivalent to columns and rows of the $N \times N$ image; t represents the sequence number of the image, which is associated with
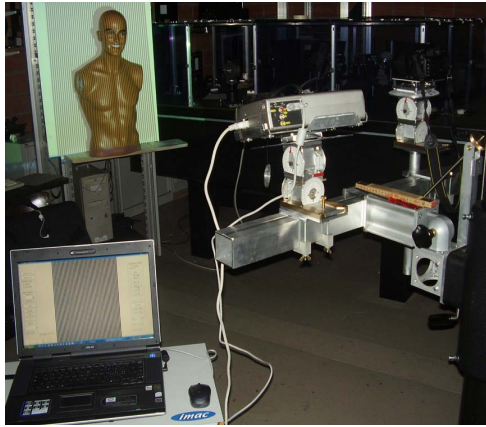
(a)
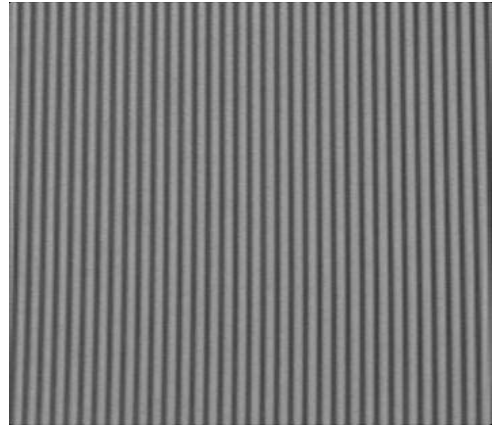
(b)

(c)
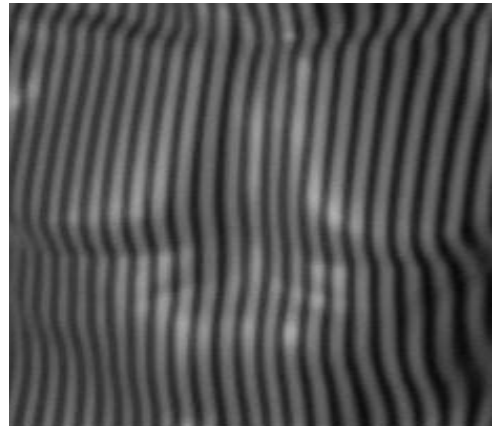
(d)
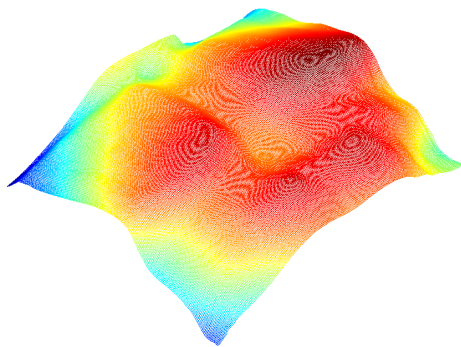
(e)

(f)

Fig. 7.5: (a) Experimental set-up. (b) Reference fringe pattern. (c) Fringe pattern phase modulated by the object's surface. (d) Cropped fringe pattern. (e) Estimated phase in radians using the proposed method. (f) Gray-scale representation of the estimated phase

77

the time instant at which that particular frame has been captured. Here we consider t as varying from 1 to T in steps of unity. $\phi(x, y, t)$ is the phase term that contains information about the object's 3D shape at time instant t. Deformation at any instant of time can thus be obtained by finding the difference between the estimated phases at the present time instant and the initial phase (i.e., $\phi(x, y, 1)$):

$$\Delta\phi_d(x, y, t_i) = \hat{\phi}(x, y, t_{i+1}) - \hat{\phi}(x, y, 1) \tag{7.10}$$

where i varies from 1 to $(T - 1)$. $\Delta\phi_d(x, y, t_i)$ can be estimated using the HIM method in two different ways.

Irrespective of the particular approach that we employ, first we need to filter the fringe patterns as explained in the previous section, and form a stack of complex exponentials as follows:

$$A_i(x, y) = I'(x, y, t_{i+1})I'^*(x, y, 1) \tag{7.11}$$

which is equivalent to

$$A_i(x, y) = b_i(x, y) \exp[j\Delta\phi_d(x, y, t_i)] + \eta(x, y, t_i) \tag{7.12}$$

where $b_i(x, y) = b(x, y, t_{i+1}) \, b(x, y, 1)$, $\Delta\phi_d(x, y, t_i) = \phi(x, y, t_{i+1}) - \phi(x, y, 1)$ and $\eta(x, y, t_i)$ is the noise term.

Now one possible scenario is to apply HIM method to find phase evolution at each pixel by forming $N \times N$ one-dimensional vectors. In this case, for each value of x and y varying from 1 to N, the vector that is formed by varying the time index from 1 to $(T - 1)$ is modeled as a polynomial phase signal:

$$g_{x,y}(t) = b_{x,y}(t) \exp[j\phi_{x,y}(t)] + \eta_{x,y}(t) \tag{7.13}$$

The above equation can be simplified as:

$$g(t) = b(t) \exp\left[j\left(\sum_{q=0}^{M} a_q t^q\right)\right] + \eta(t) \tag{7.14}$$

where q is an integer and M is the degree of the polynomial; the subscripts are dropped for the sake of simplicity. Since in rigid body deformation analysis it is possible to model the deformation/evolution of a particular surface point with a polynomial signal, the use of HIM method facilitates in measuring deformation with respect to time over the whole object surface in a computationally efficient manner.

A movie of fringe patterns is simulated and the aforementioned procedure is followed to measure the evolution of deformation phase. The results indicate the potential of HIM method for the time evolution study of deformations. Figure 7.6 shows the slices/snapshots of fringe patterns taken from the simulated movie of fringe patterns at six different time instants (at $t = 1, 14, 26, 39, 52$ and 64). Each slice of the simulated fringe pattern has the dimensions of 256×256 pixels (i.e. $N = 256$) and 128 such frames are generated
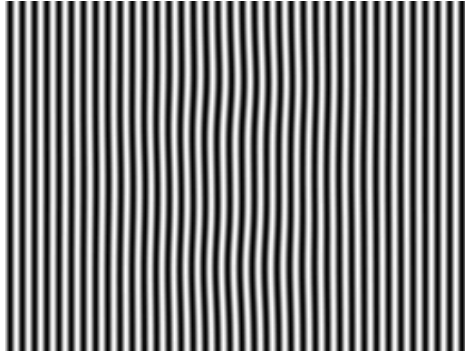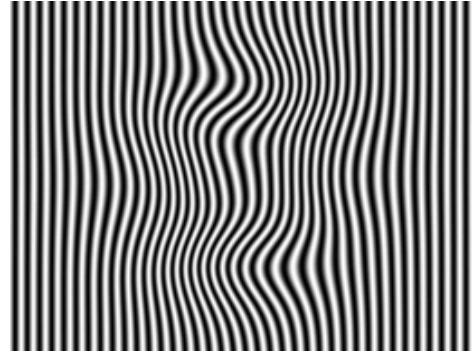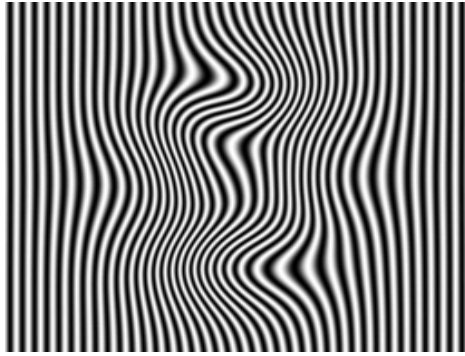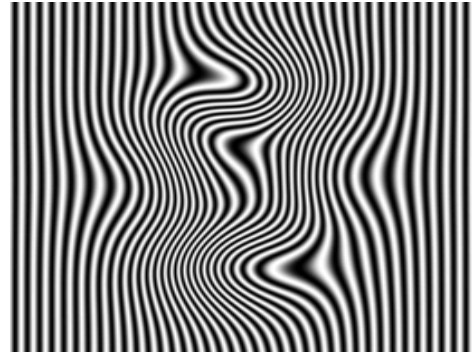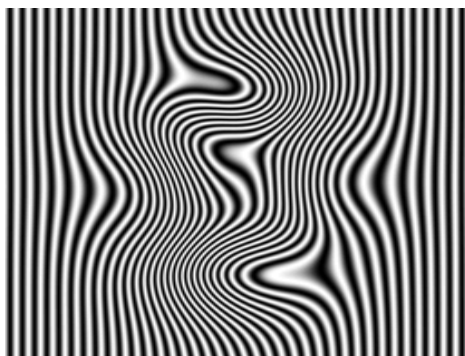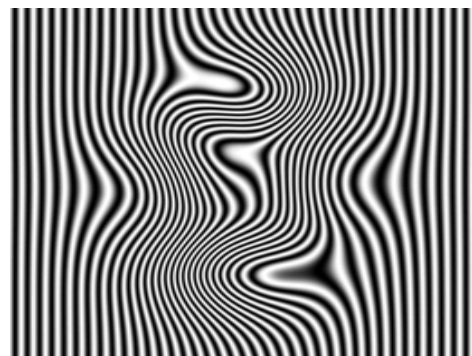
Fig. 7.6: Simulated fringe patterns corresponding to different instances of time; at (a) t=1 (b) t=14 (c) t=26 (d) t=39 (e) t=52 (f) t=64

(i.e. $T = 128$) while sinusoidally modulating the magnitude of the phase of the fringe pattern with respect to time. The HIM method is applied to each of the $256 \times 256 (= 65536)$ vectors of length 128 while modeling the phase evolution w.r.t time at each pixel with a fourth-order polynomial. The deformation estimates obtained with the HIM method at the corresponding time instances are shown in figure 7.7. Error in estimation is shown in figure 7.8. It has taken only 83 seconds to obtain an estimation of the continuous phase/deformation evolution with the HIM method for this example (for the pattern having dimensions of $256 \times 256 \times 128$). Note that with the conventional approaches, after analyzing the fringe patterns to obtain wrapped phase estimates, in order to get the continuous phase distribution, one has to resort to a three-dimensional phase unwrapping algorithm (which is even more complicated than a simple two-dimensional phase unwrapping algorithm). On the contrary, the HIM method directly produces a movie of continuous phase evolution.

Now, the second possible scenario is to consider each slice of I (see equation 7.9) as a two-dimensional fringe pattern and process it using HIM method to estimate the underlying phase distribution at that particular instant of time. In this case the HIM method can be used exactly in the same manner as explained in section 7.3 except that it need to be used $(T - 1)$ times here. Thus, in order to get the evolution of deformation with respect to time, we can apply the HIM method on $A_i(x, y)$ for each i varied from 1 to $(T - 1)$. Phase estimates obtained with this approach for the same example considered above are shown in figure 7.9. Error in estimation is shown in figure 7.10. It has taken 330 seconds to obtain the results through this approach. The reason behind the increase in the computational time when this second approach is followed is that, in estimating the phase distribution from each of the 128 frames, piecewise polynomial phase approximation has to be adopted to get an accurate estimation. $N_w = 8$ and $M = 4$ was used for producing the results shown in figure 7.9.

To perform time evolution studies experimentally, a white leather sheet (membrane) is clamped on its four sides using a rectangular frame as shown in figure 7.11a. The dimensions of the frame are $60cm \times 60cm$. Deformation to the membrane is introduced by pushing it from behind with a finger and the position of the finger is moved continuously. A sequence of images are captured while deforming the membrane with the finger. In the results shown here, a sequence of 64 images were captured while projecting the fringe pattern using the experimental setup shown in figure 7.11b. Figures 7.12a- 7.12f show few snap-shots corresponding to the frame numbers $t = 1$, 10, 20, 30, 40 and 50, respectively. These images are captured at a time interval of 1/14th of a second. The marked regions indicate locations where the the force has been applied with the finger. By processing these images as explained before, deformed phase distribution corresponding to each state of the membrane is estimated. Figure 7.13 shows the 3D mesh plots of the estimated deformation obtained with the HIM method corresponding to the time frames displayed in figure 7.12. Cosine fringes of the estimated phase distribution are shown in figure 7.14 for the purpose of illustration. It can be very well correlated from figures 7.12 and 7.14 that the method is able to successfully track the deformation profile with respect to time.
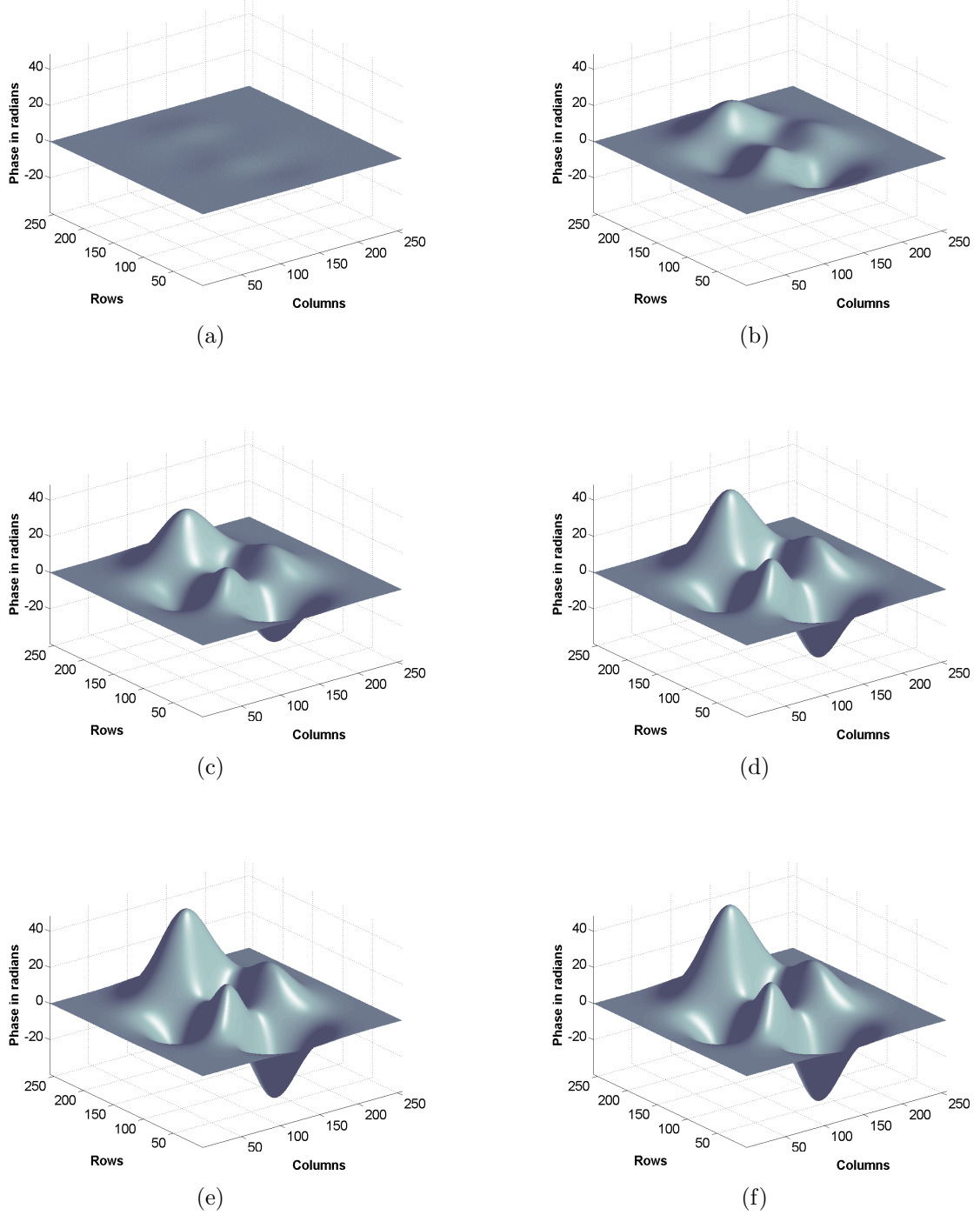
Fig. 7.7: Estimated phase distributions using HIM method at different instances of time; at (a) t=1 (b) t=14 (c) t=26 (d) t=39 (e) t=52 (f) t=64
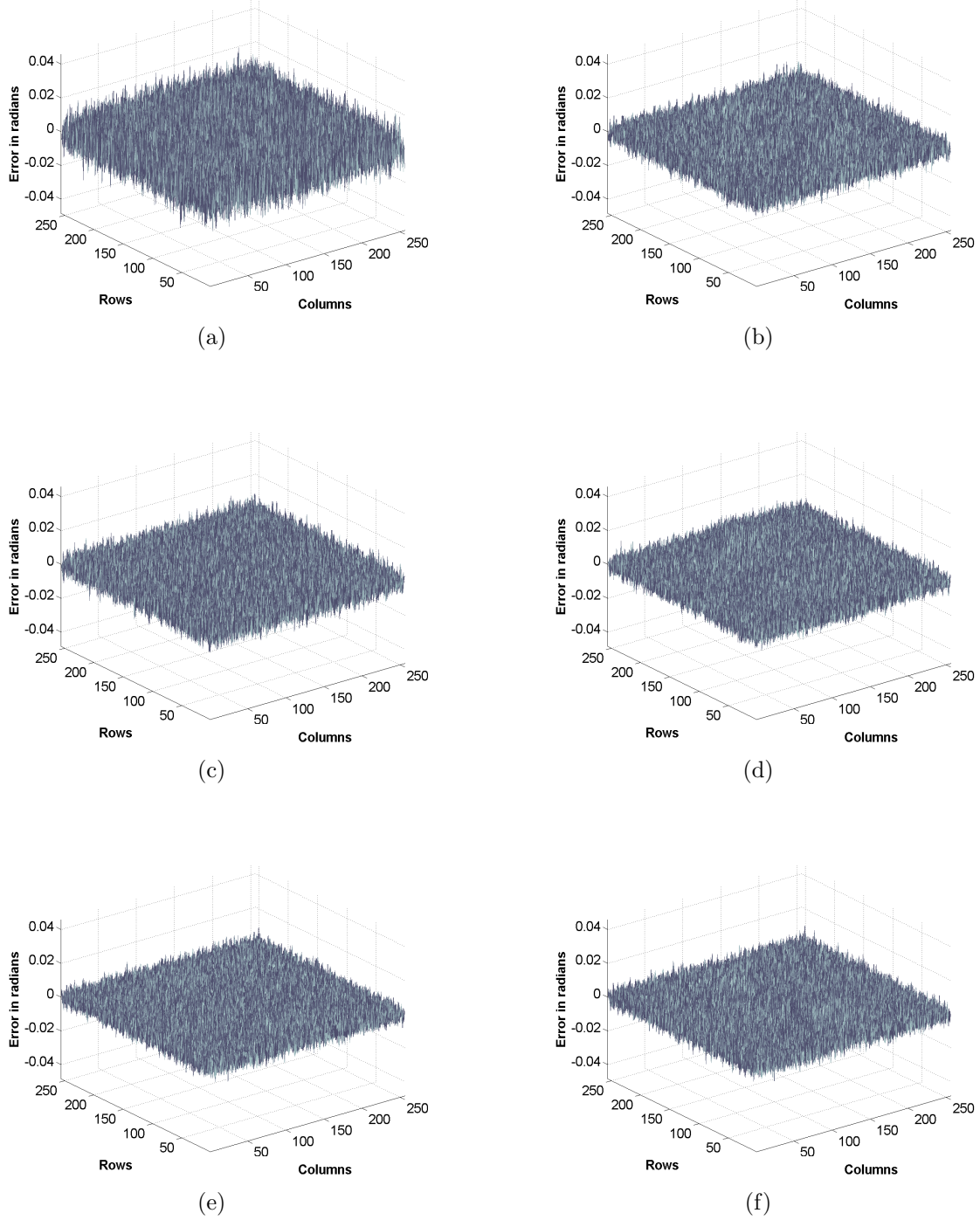
Fig. 7.8: Error in the phase estimation using HIM method at different instances of time; at (a) t=5 (b) t=14 (c) t=26 (d) t=39 (e) t=52 (f) t=64
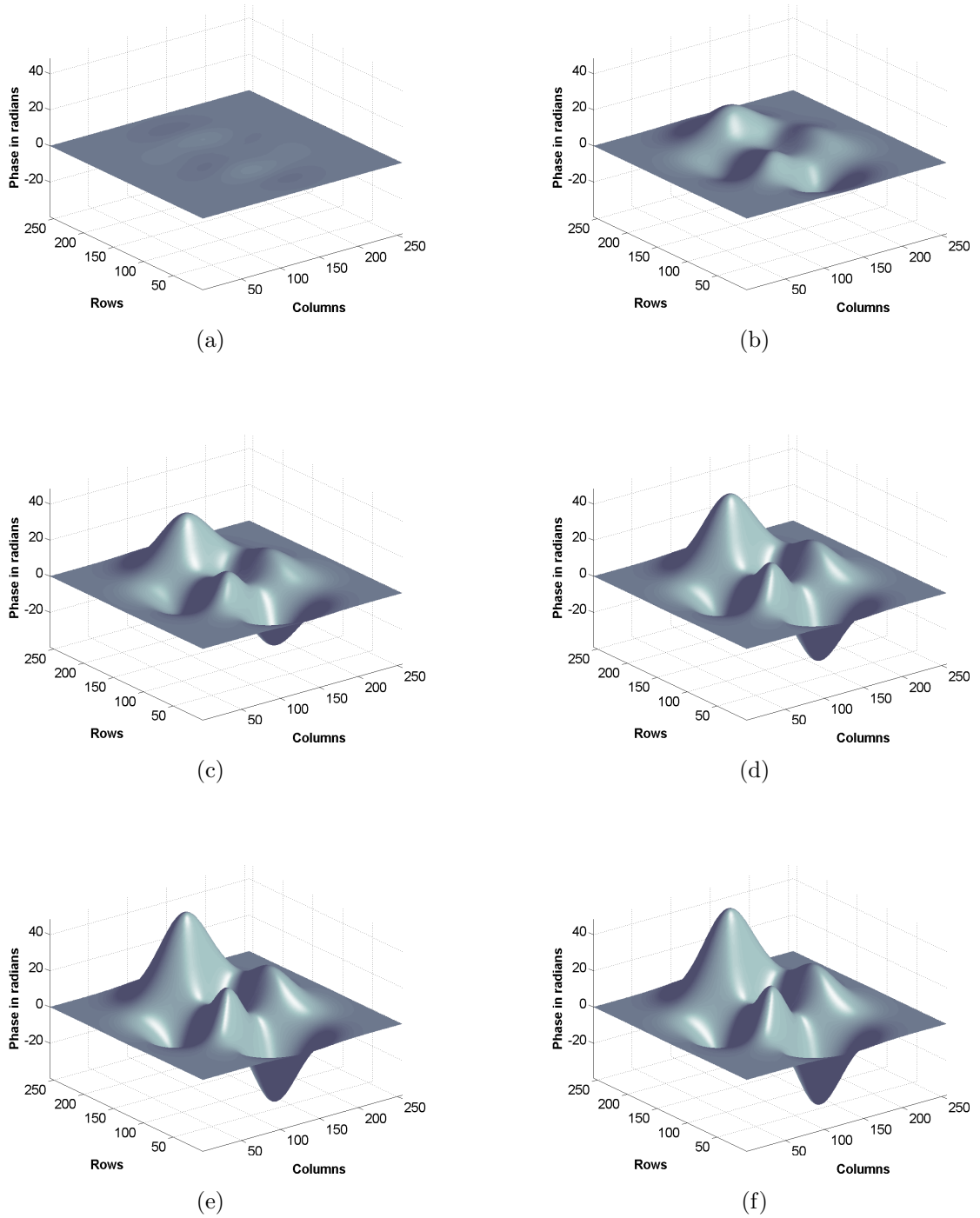
Fig. 7.9: Estimated phase distributions using HIM method (by following the second approach) at different instances of time; at (a) t=1 (b) t=14 (c) t=26 (d) t=39 (e) t=52 (f) t=64
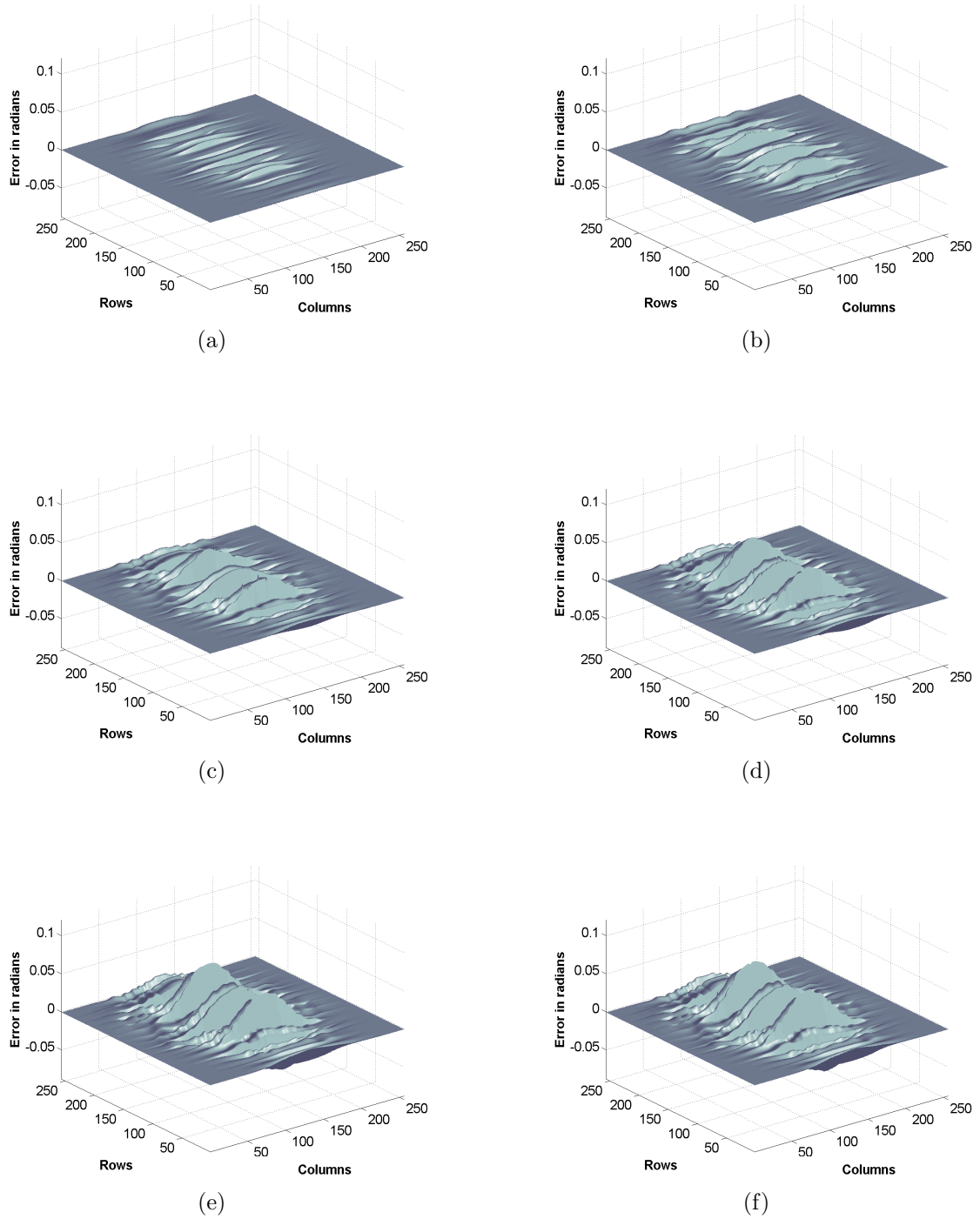
Fig. 7.10: Error in the phase estimation using HIM method (by following the second approach) at different instances of time; at (a) t=5 (b) t=14 (c) t=26 (d) t=39 (e) t=52 (f) t=64
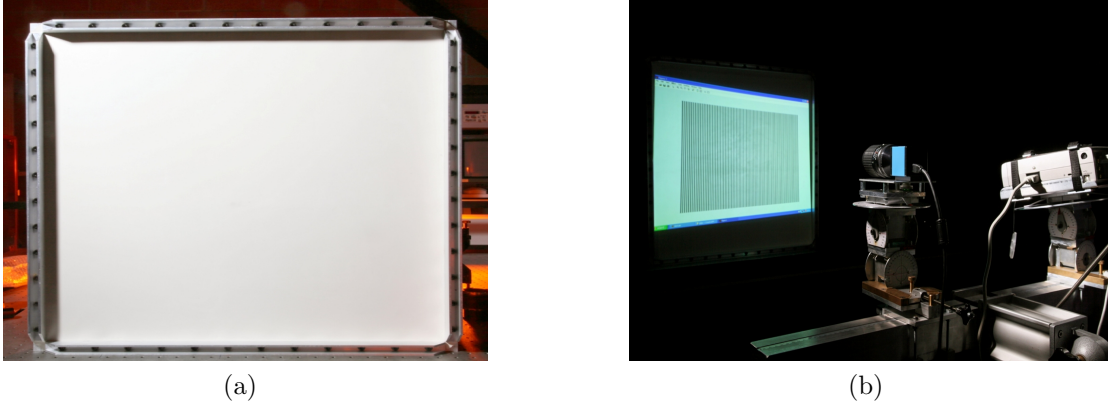
Fig. 7.11: Time evolution studies (a) Leather membrane clamped on its four sides ($60cm \times 60cm$) (b) Experimental setup

7.5 Time Evolution Study of Strain

As mentioned earlier, in several applications involving non-destructive testing and evaluation, such as in the study of fault propagation and material characterization, it is crucial to be able to monitor directly the strain evolution with respect to time [146–150]. This section shows the usefulness of HIM method in the direct measurement of strain distribution in fringe projection technique. As explained in the previous chapter for the case of digital holographic interferometry, strain distribution can be estimated with the HIM method in each state of the object by analyzing $A_i(x, y)$ (see equation 7.12) for each i varied from 1 to $(T - 1)$. Figure 7.15 shows 3D mesh plots of continuous strain distributions estimated using HIM method corresponding to the experimentally recorded fringe patterns shown in figure 7.12. For the purpose of illustration, corresponding cosine fringes are shown in figure 7.16. Note that in this case also, in contrary to the existing methods, the HIM method avoids the necessity of using a three-dimensional phase unwrapping algorithm.

7.6 Conclusions

This chapter demonstrated the effectiveness of HIM method for different applications in fringe projection technique. Measurement of 3D shape of objects using HIM method is presented with both simulation and experimental results. Considering the fact that HIM method is computationally very efficient, its utility in time evolution study of deformation and strain are explored. Simulation and experimental results substantiate the potentiality of HIM method in monitoring the deformation and/or strain by projecting a carrier fringe pattern on to the object which is being subjected to loading.
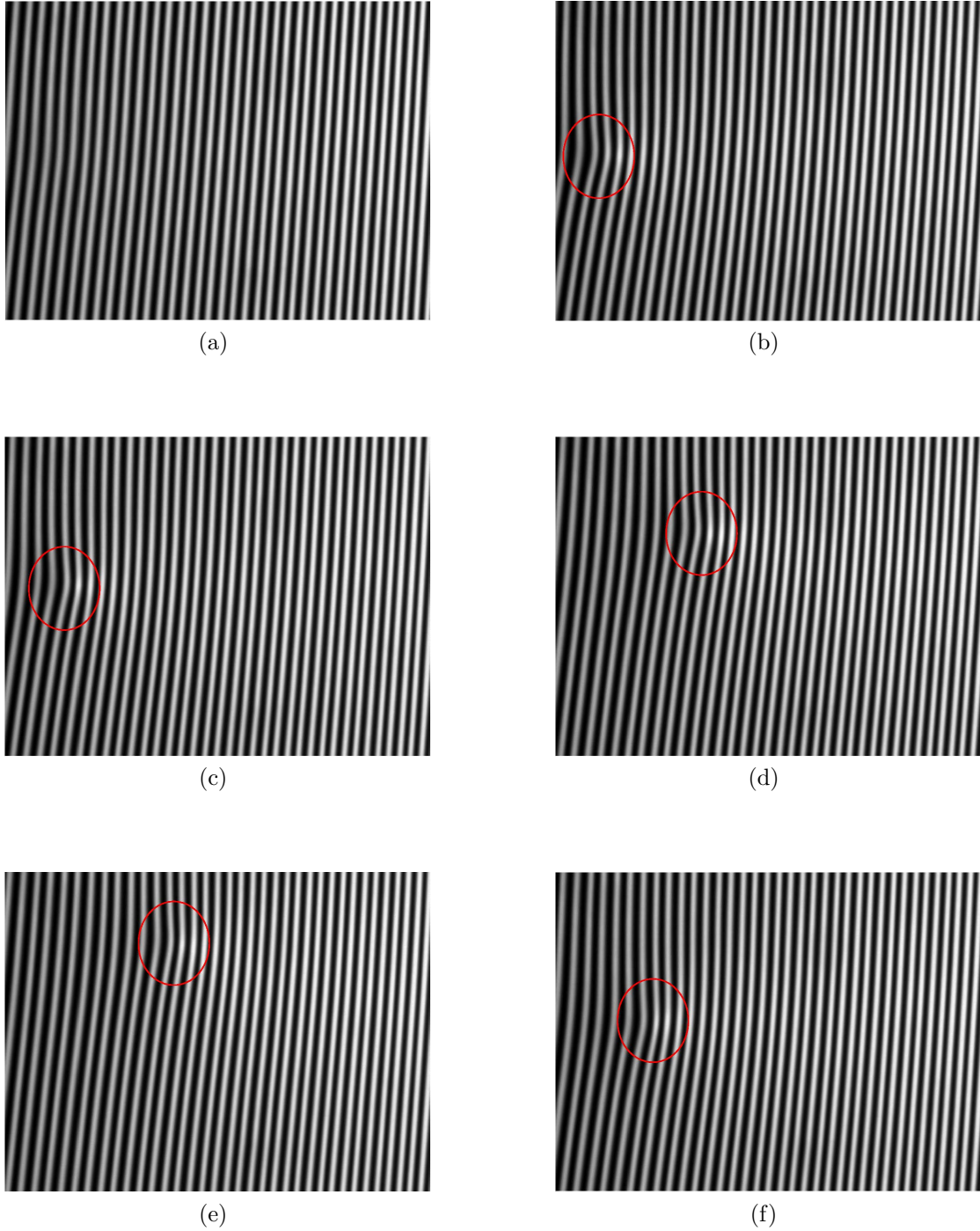
Fig. 7.12: Recorded fringe patterns in a fringe projection technique experiment conducted to study the evolution of deformation w.r.t time (a) t=1 (b) t=10 (c) t=20 (d) t=30 (e) t=40 (f) t=50
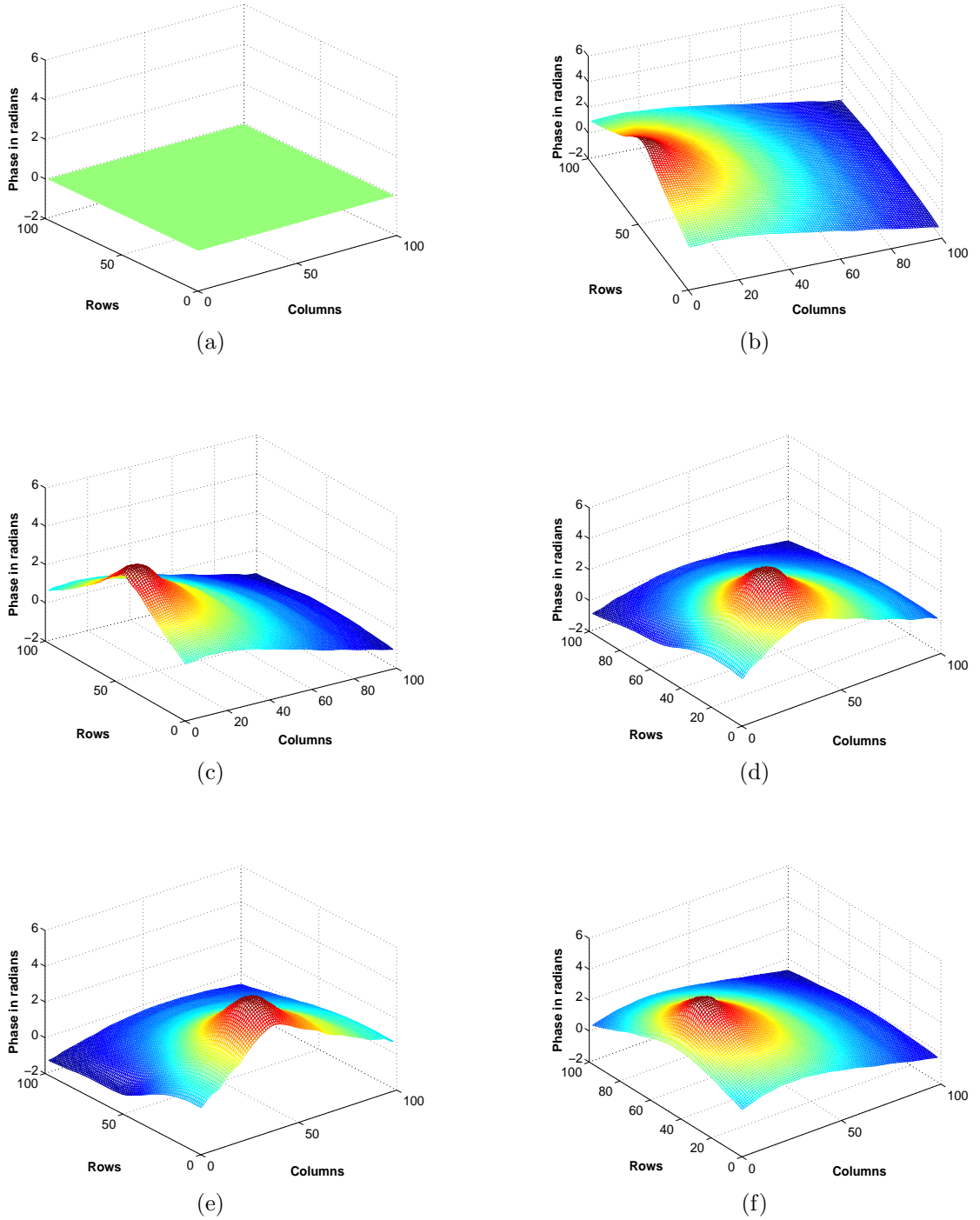
Fig. 7.13: 3D mesh plots of estimated phase distributions using HIM method at different instances of time from the experimentally captured fringe patterns (a) t=1 (b) t=10 (c) t=20 (d) t=30 (e) t=40 (f) t=50
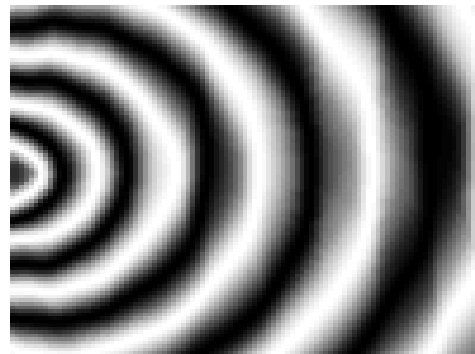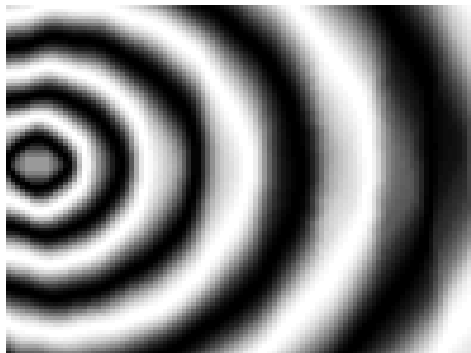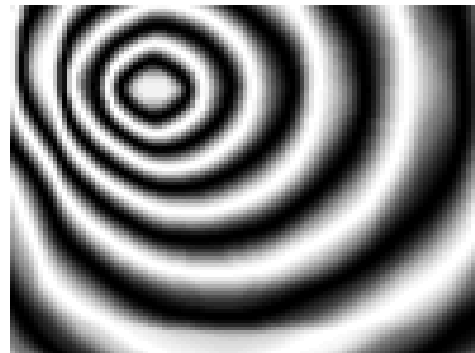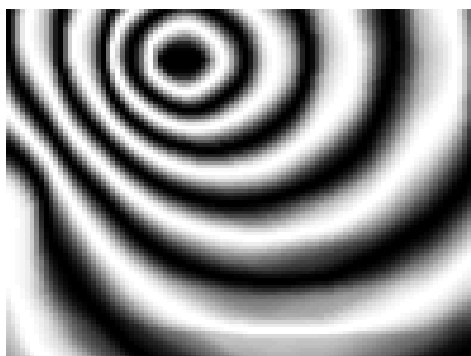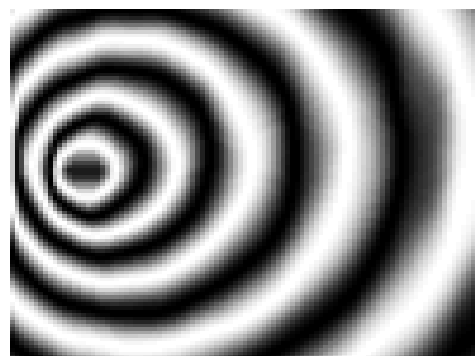
Fig. 7.14: Cosine fringes corresponding to the estimated phase distributions using HIM method at different instances of time (a) t=1 (b) t=10 (c) t=20 (d) t=30 (e) t=40 (f) t=50
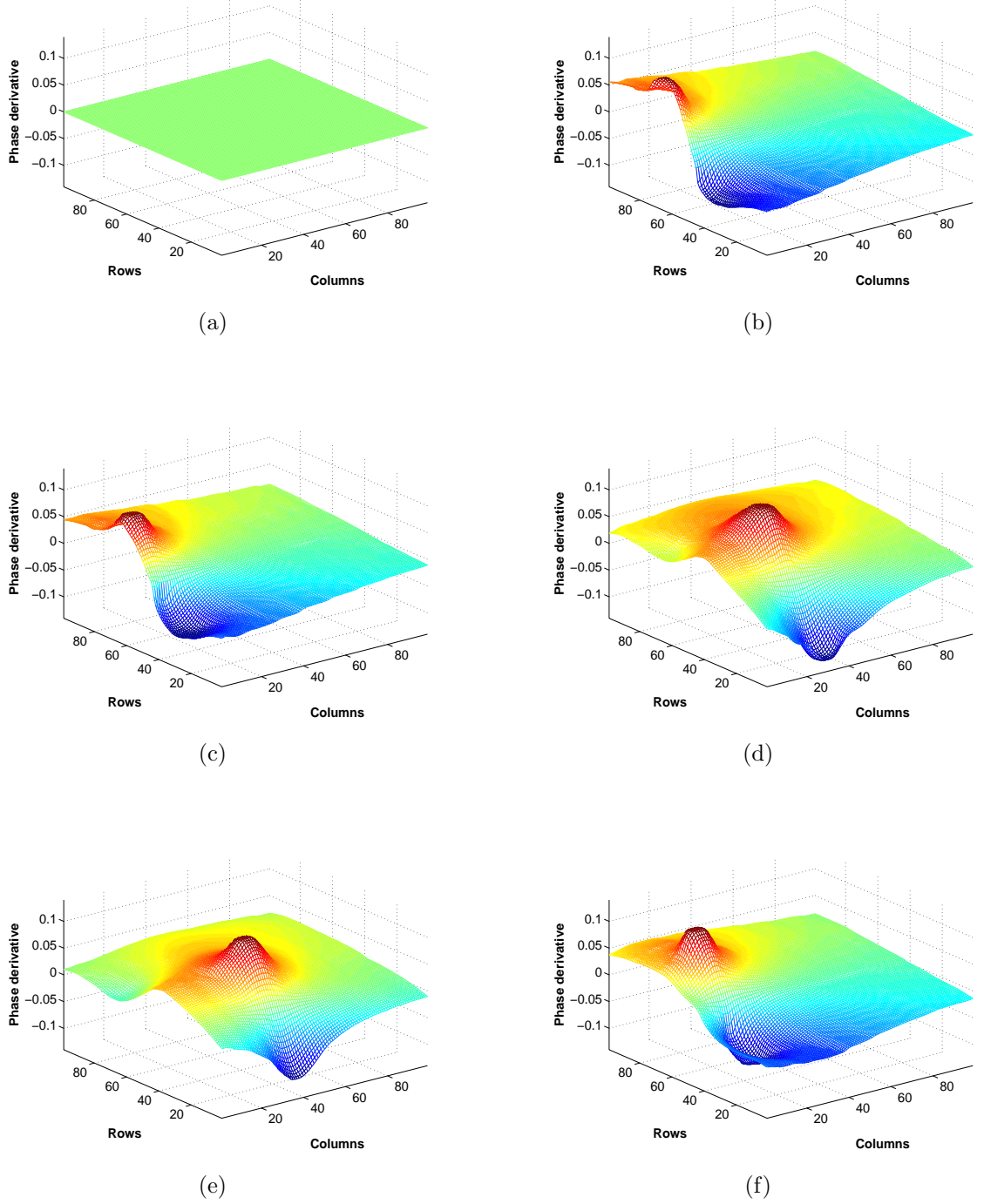
Fig. 7.15: 3D mesh plots of estimated phase derivative distributions using the HIM method at different instances of time for the experimentally captured fringe patterns (a) t=1 (b) t=10 (c) t=20 (d) t=30 (e) t=40 (f) t=50
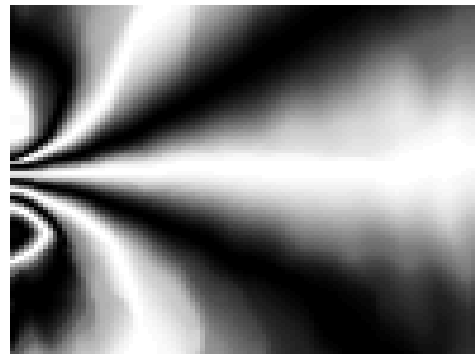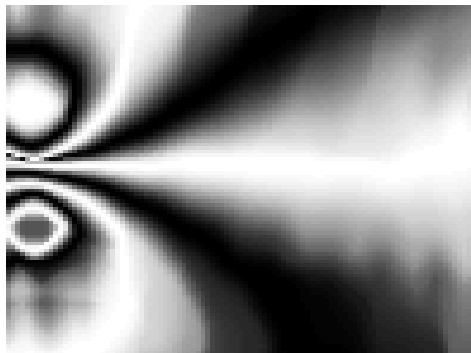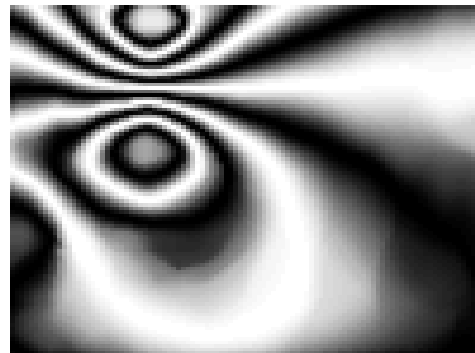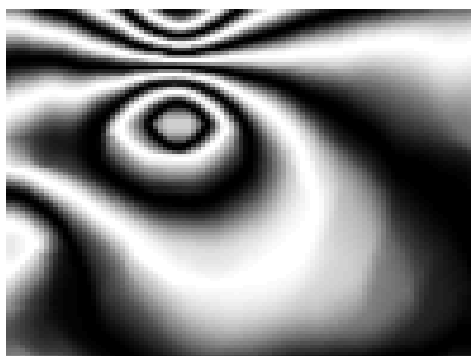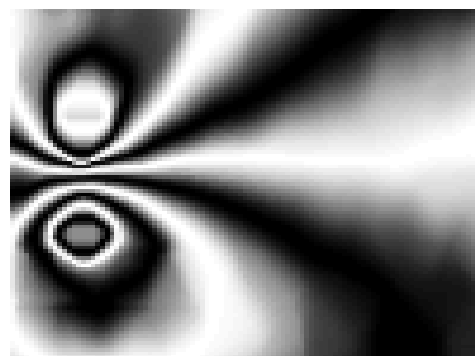
Fig. 7.16: Cosine fringes corresponding to the estimated phase derivative distributions using the HIM method at different instances of time (a) t=1 (b) t=10 (c) t=20 (d) t=30 (e) t=40 (f) t=50

Chapter 8

Conclusions

The research in this thesis is primarily driven by the desire to develop an approach having the capability to provide accurate and direct estimation of the unwrapped phase distribution from a single record of the interference pattern. The approach explored by us has the potential to (1) provide simultaneous estimation of phase and its first and second-order derivatives within the framework of a single interferometric configuration, and (2) render unnecessary the use of any filtering and unwrapping operations. The approach taken is in addition computationally efficient, making it suitable for performing time evolution studies.

Before the advent of the *piecewise polynomial phase approximation approach* (P3A2) presented in this thesis, one had the possibility to use either multiple analysis tools or multiple interferometric configurations, mostly in conjunction with suitable filtering and unwrapping algorithms in order to measure simultaneously the deformation, strain and curvature undergone by a deformed object. The current research, has thus, significantly contributed in overcoming the limitations exhibited by the present crop of spatial analysis methods by equipping the newly developed analysis methods based on P3A2 with the features stated in the preceding paragraph.

P3A2 relies on dividing each row/column of the pattern into several segments and modeling the data in each segment with a *polynomial phase signal*. The polynomial coefficients are then estimated using different techniques such as *maximum likelihood estimation* (MLE), *discrete-chirp-Fourier transform* (DCFT), *high-order instantaneous moments* (HIM) and *cubic-phase-function* (CPF). Constructing appropriate polynomials with the estimated coefficients results in the direct estimation of the unwrapped distribution corresponding to the phase and/or its first and second-order derivatives. Chapters 2 to 5 have shown the development of these new generation fringe analysis methods.

ML method presented in chapter-2 is optimal in terms of estimation accuracy and is robust against noise. However, it is computationally demanding due to the multi-dimensional exhaustive grid search. Chapter-3 introduced the DCFT method as a computationally efficient version of the ML estimation method. Overlapping windowing concept in P3A2 is introduced in this chapter and found to give highly accurate results. Direct estimation of unwrapped distribution corresponding to the first-order derivative of phase using DCFT

has also been accomplished and is included in this chapter. The development of HIM method for higher order polynomial representation of the data in each segment is shown in chapter-4. Investigations carried out to make it computationally highly efficient, and to make it perform exceptionally well in terms of accuracy of estimation are also presented. Comparison of the performance of the HIM method with the bench mark methods is also shown in chapter-4. Chapter-5 presents the development of the CPF method as a highly robust analysis method against noise for the estimation of phase and its derivative, while preserving the unique features of P3A2.

Chapter-6 demonstrates the potential applications of the methods presented in earlier chapters in *both classical and digital holographic interferometry techniques*. Simultaneous measurement of displacement, strain, and curvature in digital holographic interferometric configuration using the HIM method is also presented. Chapter-7 presents the applications of P3A2 in *fringe projection technique*, such as, in the measurement of the three-dimensional shapes of the objects, or for studying the temporal evolution of deformation and/or strain distributions.

Further research needs to be focused on developing adaptive windowing concept in spatial domain so as to make the optimal selection for the window length in an automated manner depending on the nature of local phase variations of the data. The selection of the window length is to be optimal in the sense of making a best trade-off between the computational burden and the accuracy of estimation. More advance selection criteria can be devised to decide on the required order of polynomial approximation, the segment size, and the method that can be used to estimate the polynomial coefficients. Research also needs to be diverted towards examining the applicability of these methods to other important interferometric techniques in optical metrology, such as, digital speckle pattern interferometry.

Bibliography

[1] M. Takeda, H. Ina, and S. Kobayashi, "Fourier-transform method of fringe-pattern analysis for computer-based topography and inteferometry." *J. Opt. Soc. Am.*, vol. 72, no. 1, pp. 156–160, 1982.

[2] L. R. Watkins, S. M. Tan, and T. H. Barnes, "Determination of interferometer phase distributions by use of wavelets," *Opt. Lett.*, vol. 24, no. 13, pp. 905–907, 1999.

[3] Q. Kemao, "Windowed fourier transform for fringe pattern analysis," *Appl. Opt.*, vol. 43, no. 13, pp. 2695–2702, 2004.

[4] M. Servin, J. L. Marroquin, and F. J. Cuevas, "Demodulation of a single interferogram by use of a two-dimensional regularized phase-tracking technique," *Appl. Opt.*, vol. 36, no. 19, pp. 4540–4548, 1997.

[5] A. Patil, R. Langoju, P. Rastogi, and S. Ramani, "Statistical study and experimental verification of high-resolution methods in phase-shifting interferometry," *J. Opt. Soc. Am. A*, vol. 24, no. 3, pp. 794–813, 2007.

[6] G. K. Bhat, "Hybrid fringe analysis technique for the elimination of random noise in interferometric wrapped phase maps," *Opt. Commun.*, vol. 111, no. 3-4, pp. 214–218, 1994.

[7] Z. Wang, J. Zhang, and Z. Zhao, "New methods of the filtering the phase noise in the interferometric sar," in *Int. Geoscience and Remote Sensing Symp.*, vol. 4, 2004, pp. 2622–2625.

[8] F. Palacios, E. Goncalves, J. Ricardo, and J. L. Valin, "Adaptive filter to improve the performance of phase-unwrapping in digital holography," *Opt. Commun.*, vol. 238, no. 4-6, pp. 245–251, 2004.

[9] H. A. Aebischer and S. Waldner, "Simple and effective method for filtering speckle-interferometric phase fringe patterns," *Opt. Commun.*, vol. 162, no. 4, pp. 205–210, 1999.

[10] M. J. Huang and W. Sheu, "Histogram-data-orientated filter for inconsistency removal of interferometric phase maps," *Opt. Eng.*, vol. 44, no. 4, pp. 1–11, 2005.

[11] R. M. Goldstein, H. A. Zebker, and C. L. Werner, "Satellite radar interferometry: two-dimensional phase unwrapping," *Radio Science*, vol. 23, no. 4, pp. 713–720, 1988.

[12] A. Baldi, "Phase unwrapping by region growing," *Appl. Opt.*, vol. 42, no. 14, pp. 2498–2505, 2003.

[13] J. Meneses, T. Gharbi, and P. Humbert, "Phase-unwrapping algorithm for images with high noise content based on a local histogram," *Appl. Opt.*, vol. 44, no. 7, pp. 1207–1215, 2005.

[14] R. Cusack, J. M. Huntley, and H. T. Goldrein, "Improved noise-immune phase-unwrapping algorithm," *Appl. Opt.*, vol. 34, no. 5, pp. 781–789, 1995.

[15] M. Servin, F. J. Cuevas, D. Malacara, J. L. Marroquin, and R. Rodriguez-Vera, "Phase unwrapping through demodulation by use of the regularized phase-tracking technique," *Appl. Opt.*, vol. 38, no. 10, pp. 1934–1941, 1999.

[16] A. Asundi and Z. Wensen, "Fast phase-unwrapping algorithm based on a gray-scale mask and flood fill," *Appl. Opt.*, vol. 37, no. 23, pp. 5416–5420, 1998.

[17] S. Zhang, X. Li, and S. Yau, "Multilevel quality-guided phase unwrapping algorithm for real-time three-dimensional shape reconstruction," *Appl. Opt.*, vol. 46, no. 1, pp. 50–57, 2007.

[18] G. K. Bhat, "A Fourier transform technique to obtain phase derivatives in interferometry," *Opt. Commun.*, vol. 110, no. 3-4, pp. 279–286, 1994.

[19] Q. Kemao, S. H. Soon, and A. Asundi, "Instantaneous frequency and its application to strain extraction in moire interferometry," *Appl. Opt.*, vol. 42, no. 32, pp. 6504–6513, 2003.

[20] C. A. Sciammarella and T. Kim, "Frequency modulation interpretation of fringes and computation of strains," *Exp. Mech.*, vol. 45, no. 5, pp. 393–403, 2005.

[21] F. P. Chiang and T. Y. Kao, "An optical method of generating slope and curvature contours of bent plates," *Int. J. Solids Struct.*, vol. 15, no. 3, pp. 251–260, 1979.

[22] Y. Y. Hung, "Shearography: A new optical method for strain measurement and nondestructive testing." *Opt. Eng.*, vol. 21, no. 3, pp. 391–395, 1982.

[23] D. K. Sharma, R. S. Sirohi, and M. P. Kothiyal, "Simultaneous measurement of slope and curvature with a three-aperture speckle shearing interferometr." *Appl. Opt.*, vol. 23, no. 10, pp. 1542–1546, 1984.

[24] P. K. Rastogi, "Visualization and measurement of slope and curvature fields using holographic interferometry: an application to flaw detection," *J. Mod. Opt.*, vol. 38, no. 7, pp. 1251–1263, 1991.

[25] S. K. Bhadra, S. K. Sarkar, R. N. Chakraborty, and A. Basuray, "Coherent moire technique for obtaining slope and curvature of stress patterns," *Opt. Eng.*, vol. 33, no. 10, pp. 3359–3363, 1994.

[26] G. Subramanian and A. Subramanian, "Curvature contours of flexed plates by a multiple illumination moire shearing interferometer," *Strain*, vol. 32, no. 2, pp. 59–62, 1996.

[27] B. Chen and C. Basaran, "Automatic full strain field moiré interferometry measurement with nano-scale resolution," *Exp. Mech.*, vol. 48, no. 5, pp. 665–673, 2008.

[28] C. J. Tay, S. L. Toh, H. M. Shang, and Q. Y. Lin, "Direct determination of second-order derivatives in plate bending using multiple-exposure shearography," *Opt. Laser Technol.*, vol. 26, no. 2, pp. 91–98, 1994.

[29] P. K. Rastogi, "Measurement of curvature and twist of a deformed object by electronic speckle-shearing pattern interferometry," *Opt. Lett.*, vol. 21, no. 12, pp. 905–907, 1996.

[30] K. F. Wang, A. Kiet Tieu, and E. B. Li, "Simultaneous measurement of pure curvature and twist distribution fields by a five-aperture shearing and two-Fourier filtering technique," *Appl. Opt.*, vol. 39, no. 16, pp. 2577–2583, 2000.

[31] F. S. Chau and J. Zhou, "Direct measurement of curvature and twist of plates using digital shearography," *Opt. Laser Eng.*, vol. 39, no. 4, pp. 431–440, 2003.

[32] K. F. Wang, A. K. Tieu, and M. H. Gao, "Measurement of curvature distribution using digital speckle three-shearing aperture interferometry," *Opt. Laser Technol.*, vol. 39, no. 5, pp. 926–928, 2007.

[33] U. Schnars and W. P. O. Juptner, "Digital recording and reconstruction of holograms in hologram interferometry and shearography," *Appl. Opt.*, vol. 33, no. 20, pp. 4373–4377, 1994.

[34] Y. Zou, G. Pedrini, and H. Tiziani, "Derivatives obtained directly from displacement data," *Opt. Commun.*, vol. 111, no. 5-6, pp. 427–432, 1994.

[35] M. Y. Y. Hung, L. Lin, and H. M. Shang, "Simple method for direct determination of bending strains by use of digital holography," *Appl. Opt.*, vol. 40, no. 25, pp. 4514–4518, 2001.

[36] C. Liu, "Simultaneous measurement of displacement and its spatial derivatives with a digital holographic method," *Opt. Eng.*, vol. 42, no. 12, pp. 3443–3446, 2003.

[37] W. Chen, C. Quan, and C. J. Tay, "Measurement of curvature and twist of a deformed object using digital holography," *Appl. Opt.*, vol. 47, no. 15, pp. 2874–2881, 2008.

[38] C. Quan, C. J. Tay, and W. Chen, "Determination of displacement derivative in digital holographic interferometry," *Opt. Commun.*, vol. 282, no. 5, pp. 809–815, 2009.

[39] K. Qian, Y. Fu, Q. Liu, H. S. Seah, and A. Asundi, "Generalized three-dimensional windowed Fourier transform for fringe analysis," *Opt. Lett.*, vol. 31, no. 14, pp. 2121–2123, 2006.

[40] Q. Kemao, "Two-dimensional windowed Fourier transform for fringe pattern analysis: Principles, applications and implementations," *Opt. Laser Eng.*, vol. 45, no. 2, pp. 304–317, 2007.

[41] J. Zhong and J. Weng, "Dilating gabor transform for the fringe analysis of 3-d shape measurement," *Opt. Eng.*, vol. 43, no. 4, pp. 895–899, 2004.

[42] C. de Lega, "Continuous deformation measurement using dynamic phase-shifting and wavelet reansforms," in *Applied optics and optoelectronics.* IOP, 1996, pp. 261–267.

[43] P. D. M. Carrez and G. Tribillon, "Application of fringe projection and wavelet analysis to the identification of a finite element model- study of the influence of ripening on the mechanical properties of a biologic material," p. 614 to 622, 2001.

[44] C. Shakher, R. Kumar, S. K. Singh, and S. A. Kazmi, "Application of wavelet filtering for vibration analysis using digital speckle pattern interferometry," *Opt. Eng.*, vol. 41, no. 1, pp. 176–180, 2002.

[45] M. Afifi, A. Fassi-Fihri, M. Marjane, K. Nassim, M. Sidki, and S. Rachafi, "Paul wavelet-based algorithm for optical phase distribution evaluation," *Opt. Commun.*, vol. 211, no. 1-6, pp. 47–51, 2002.

[46] A. Dursun, S. Ozder, and F. N. Ecevit, "Continuous wavelet transform analysis of projected fringe patterns," *Meas. Sci. Technol.*, vol. 15, no. 9, pp. 1768–1772, 2004.

[47] J. Zhong and J. Weng, "Spatial carrier-fringe pattern analysis by means of wavelet transform: Wavelet transform profilometry," *Appl. Opt.*, vol. 43, no. 26, pp. 4993–4998, 2004.

[48] M. A. Gdeisat, D. R. Burton, and M. J. Lalor, "Spatial carrier fringe pattern demodulation by use of a two-dimensional continuous wavelet transform," *Appl. Opt.*, vol. 45, no. 34, pp. 8722–8732, 2006.

[49] A. Federico and G. H. Kaufmann, "Evaluation of the continuous wavelet transform method for the phase measurement of electronic speckle pattern interferometry fringes," *Opt. Eng.*, vol. 41, no. 12, pp. 3209–3216, 2002.

[50] A. Federico and G. H. Kaufmann, "Phase retrieval in digital speckle pattern interferometry by use of a smoothed space-frequency distribution," *Appl. Opt.*, vol. 42, no. 35, pp. 7066–7071, 2003.

[51] B.Porat, *Digital processing of random signals.* Prentice-Hall, 1994.

[52] R. R. Cordero, J. Molimard, F. Labbe, and A. Martinez, "Strain maps obtained by phase-shifting interferometry: An uncertainty analysis," *Opt. Commun.*, vol. 281, no. 8, pp. 2195–2206, 2008.

[53] Q. Kemao, S. H. Soon, and A. Asundi, "Instantaneous frequency and its application to strain extraction in moire interferometry," *Appl. Opt.*, vol. 42, no. 32, pp. 6504–6513, 2003.

[54] C. A. Sciammarella and T. Kim, "Determination of strains from fringe patterns using space-frequency representations," *Opt. Eng.*, vol. 42, no. 11, pp. 3182–3193, 2003.

[55] K. Qian, S. H. Soon, and A. Asundi, "Phase-shifting windowed Fourier ridges for determination of phase derivatives," *Opt. Lett.*, vol. 28, no. 18, pp. 1657–1659, 2003.

[56] A. T. Andonian and S. Danyluk, "Residual stresses of thin, short rectangular plates," *J. Material Sci.*, vol. 20, no. 12, pp. 4459–4464, 1985.

[57] Y. Kwon, S. Danyluk, L. Bucciarelli, and J. P. Kalejs, "Residual stress measurement in silicon sheet by shadow moiré interferometry," *J. Cryst. Growth*, vol. 82, no. 1-2, pp. 221–227, 1987.

[58] F. S. Chau, S. L. Toh, C. J. Tay, and H. M. Shang, "Some examples of nondestructive flaw detection by shearography," *J. Nondestruct. Eval.*, vol. 8, no. 4, pp. 225–234, 1989.

[59] B. Ovryn, "Holographic interferometry," *Critical Reviews in Biomedical Engineering*, vol. 16, no. 4, pp. 269–322, 1989.

[60] A. Twitto, J. Shamir, A. Bekker, and A. Notea, "Detection of internal defects using phase shifting holographic interferometry," *NDT and E International*, vol. 29, no. 3, pp. 163–173, 1996.

[61] T. J. Mackin, K. E. Perry, J. S. Epstein, C. Cady, and A. G. Evans, "Strain fields and damage around notches in ceramic-matrix composites," *J. Am. Ceram. Soc.*, vol. 79, no. 1, pp. 65–73, 1996.

[62] M. R. Miller, I. Mohammed, P. S. Ho, and X. Dai, "Study of thermal deformation in underfilled flip-chip packages using high-resolution moire interferometry," *American Society of Mechanical Engineers, EEP*, vol. 26 3, pp. 787–793, 1999.

[63] H. Xie, S. Kishimoto, J. Li, D. Zou, F. Dai, and N. Shinya, "Deformation analysis of laser processed grain oriented silicon steel sheet using moire interferometry," *Materials Science Research International*, vol. 5, no. 4, pp. 291–295, 1999.

[64] J. S. Ibrahim, J. N. Petzing, and J. R. Tyrer, "Deformation analysis of aircraft wheels using a speckle shearing interferometer," *Proc. Inst. Mech. Eng., Part G: J. Aerospace Engg.*, vol. 218, no. 4, pp. 287–295, 2004.

[65] U. Schnars and W. P. O. Juptner, "Digital recording and numerical reconstruction of holograms," *Meas. Sci. Technol.*, vol. 13, no. 9, pp. R85–R101, 2002.

[66] Y. Morimoto, T. Matui, M. Fujigaki, and N. Kawagishi, "Subnanometer displacement measurement by averaging of phase difference in windowed digital holographic interferometry," *Opt. Eng.*, vol. 46, no. 2, 2007.

[67] M. Servin, F. J. Cuevas, D. Malacara, J. L. Marroquin, and R. Rodriguez-Vera, "Phase unwrapping through demodulation by use of the regularized phase-tracking technique," *Appl. Opt.*, vol. 38, no. 10, pp. 1934–1941, 1999.

[68] K. Qian, H. S. Seah, and A. Asundi, "Filtering the complex field in phase shifting interferometry," *Opt. Eng.*, vol. 42, no. 10, pp. 2792–2793, 2003.

[69] W. Rudin, *Principles of mathematical analysis.* McGraw-Hill, 1976.

[70] T. J. Abatzoglou, "Fast maximum likelihood joint estimation of frequency and frequency rate." *IEEE Trans. Aero. and Elect. Sys.*, vol. AES-22, no. 6, pp. 708–715, 1986.

[71] J. C. Lagarias, J. A. Reeds, M. H. Wright, and P. E. Wright, "Convergence properties of the nelder-mead simplex method in low dimensions," *SIAM Journal on Optimization*, vol. 9, no. 1, pp. 112–147, 1999.

[72] Q. Kemao, L. T. H. Nam, L. Feng, and S. H. Soon, "Comparative analysis on some filters for wrapped phase maps," *Appl. Opt.*, vol. 46, no. 30, pp. 7412–7418, 2007.

[73] M. P. Rimmer, C. M. King, and D. G. Fox, "Computer program for the analysis of interferometric test data," *Appl. Opt.*, vol. 11, no. 12, pp. 2790–2796, 1972.

[74] J. Y. Wang and D. E. Silva, "Wave-front interpretation with zernike polynomials," *Appl. Opt.*, vol. 19, no. 9, pp. 1510–1518, 1980.

[75] C. J. Kim, "Polynomial fit of interferograms," *Appl. Opt.*, vol. 21, no. 24, pp. 4521–4525, 1982.

[76] A. Cordero-Davila, A. Cornejo-Rodriguez, and O. Cardona-Nunez, "Polynomial fitting of interferograms with gaussian errors on fringe coordinates. i: Computer simulations," *Appl. Opt.*, vol. 33, no. 31, pp. 7339–7342, 1994.

[77] J. Novak and A. Miks, "Least-squares fitting of wavefront using rational function," *Opt. Laser Eng.*, vol. 43, no. 7, pp. 40–51, 2005.

[78] X. Xia, "Discrete chirp-Fourier transform and its application to chirp rate estimation," *IEEE Trans. Sig. Proc.*, vol. 48, no. 11, pp. 3122–3133, 2000.

[79] X. Guo, H. Sun, S. Wang, and G. Liu, "Comments on discrete chirp-Fourier transform and its application to chirp rate estimation," *IEEE Trans. Sig. Proc.*, vol. 50, no. 12, p. 3115, 2002.

[80] S. Peleg and B. Porat, "Estimation and classification of polynomial-phase signals," *IEEE Trans. Info. Theory*, vol. 37, no. 2, pp. 422–430, 1991.

[81] S. Peleg and B. Friedlander, "The discrete polynomial-phase transform," *IEEE Trans. Sig. Proc.*, vol. 43, no. 8, pp. 1901–1914, 1995.

[82] D. C. Ghiglia and M. D. Pritt, *Two-Dimensional Phase Unwrapping: Theory, Algorithms, and Software.* Wiley-Interscience, 1998.

[83] J. M. B. Dias and J. M. N. Leitao, "The zpim algorithm: A method for interferometric image reconstruction in sar/sas," *IEEE Trans. Image Proc.*, vol. 11, no. 4, pp. 408–422, 2002.

[84] "http://www.mathworks.com/matlabcentral/fileexchange/22504."

[85] "http://www.lx.it.pt/ bioucas/code.htm."

[86] S. Golden and B. Friedlander, "A modification of the discrete polynomial transform," *IEEE Trans. Sig. Proc.*, vol. 46, no. 5, pp. 1452–1455, 1998.

[87] R. Roy and T. Kailath, "Esprit - estimation of signal parameters via rotational invariance techniques," *IEEE Trans. Acoustics, Speech, and Signal Proc.*, vol. 37, no. 7, pp. 984–995, 1989.

[88] R. O. Schmidt, "Multiple emitter location and signal parameter estimation." *IEEE Trans. Antennas and Propagation*, vol. AP-34, no. 3, pp. 276–280, 1986.

[89] E. Aboutanios and B. Mulgrew, "Iterative frequency estimation by interpolation on Fourier coefficients," *IEEE Trans. Sig. Proc.*, vol. 53, no. 4, pp. 1237–1242, 2005.

[90] P. Stoica and R. L. Moses, *Introduction to Spectral Analysis.* Prentice Hall, 1997.

[91] P. O'Shea, "A new technique for instantaneous frequency rate estimation," *IEEE Sig. Proc. Let.*, vol. 9, no. 8, pp. 251–252, 2002.

[92] P. O Shea, "A fast algorithm for estimating the parameters of a quadratic fm signal," *IEEE Trans. Sig. Proc.*, vol. 52, no. 2, pp. 385–393, 2004.

[93] U. Schnars, "Direct phase determination in hologram interferometry with use of digitally recorded holograms," *J. Opt. Soc. Am. A*, vol. 11, no. 7, pp. 2011–2015, 1994.

[94] J. Weng, J. Zhong, and C. Hu, "Digital reconstruction based on angular spectrum diffraction with the ridge of wavelet transform in holographic phase-contrast microscopy," *Opt. Express*, vol. 16, no. 26, pp. 21 971–21 981, 2008.

[95] M. Liebling, T. Blu, and M. Unser, "Fresnelets: New multiresolution wavelet bases for digital holography," *IEEE Trans. Image Proce.*, vol. 12, no. 1, pp. 29–43, 2003.

[96] N. A. Ochoa and A. A. Silva-Moreno, "Normalization and noise-reduction algorithm for fringe patterns," *Opt. Commun.*, vol. 270, no. 2, pp. 161–168, 2007.

[97] J. A. Guerrero, J. L. Marroquin, M. Rivera, and J. A. Quiroga, "Adaptive monogenic filtering and normalization of espi fringe patterns," *Opt. Lett.*, vol. 30, no. 22, pp. 3018–3020, 2005.

[98] J. A. Quiroga and M. Servin, "Isotropic n-dimensional fringe pattern normalization," *Opt. Commun.*, vol. 224, no. 4-6, pp. 221–227, 2003.

[99] S. Lawrence Marple Jr., "Computing the discrete-time analytic signal via fft," *IEEE Trans. Sig. Proc.*, vol. 47, no. 9, pp. 2600–2603, 1999.

[100] Q. Kemao, L. T. H. Nam, L. Feng, and S. H. Soon, "Comparative analysis on some filters for wrapped phase maps," *Appl. Opt.*, vol. 46, no. 30, pp. 7412–7418, 2007.

[101] S. Zhang, "Recent progresses on real-time 3d shape measurement using digital fringe projection techniques," *Opt. Laser Eng.*, vol. 48, no. 2, pp. 149–158, 2010.

[102] X. Su and Q. Zhang, "Dynamic 3-d shape measurement method: A review," *Opt. Laser Eng.*, vol. 48, no. 2, pp. 191–204, 2010.

[103] M. Takeda and K. Mutoh, "Fourier transform profilometry for the automatic measurement of 3-d object shapes." *Appl. Opt.*, vol. 22, no. 24, pp. 3977–3982, 1983.

[104] J.-F. Lin and X.-Y. Su, "Two-dimensional Fourier transform profilometry for the automatic measurement of three-dimensional object shapes," *Opt. Eng.*, vol. 34, no. 11, pp. 3297–3302, 1995.

[105] M. A. Gdeisat, D. R. Burton, and M. J. Lalor, "Eliminating the zero spectrum in Fourier transform profilometry using a two-dimensional continuous wavelet transform," *Opt. Commun.*, vol. 266, no. 2, pp. 482–489, 2006.

[106] P. J. Tavares and M. A. Vaz, "Orthogonal projection technique for resolution enhancement of the Fourier transform fringe analysis method," *Opt. Commun.*, vol. 266, no. 2, pp. 465–468, 2006.

[107] S. Li, X. Su, W. Chen, and L. Xiang, "Eliminating the zero spectrum in Fourier transform profilometry using empirical mode decomposition," *J. Opt. Soc. Am. A*, vol. 26, no. 5, pp. 1195–1201, 2009.

[108] M. Dai and Y. Wang, "Fringe extrapolation technique based on Fourier transform for interferogram analysis with the definition," *Opt. Lett.*, vol. 34, no. 7, pp. 956–958, 2009.

[109] S. Vanlanduit, J. Vanherzeele, P. Guillaume, B. Cauberghe, and P. Verboven, "Fourier fringe processing by use of an interpolated Fourier-transform technique," *Appl. Opt.*, vol. 43, no. 27, pp. 5206–5213, 2004.

[110] J. Vanherzeele, S. Vanlanduit, and P. Guillaume, "Processing optical measurements using a regressive Fourier series: A review," *Opt. Laser Eng.*, vol. 47, no. 3-4, pp. 461–472, 2009.

[111] J. Vanherzeele, P. Guillaume, and S. Vanlanduit, "Fourier fringe processing using a regressive Fourier-transform technique," *Opt. Laser Eng.*, vol. 43, no. 6, pp. 645–658, 2005.

[112] S. Zheng, W. Chen, and X. Su, "Adaptive windowed Fourier transform in 3-d shape measurement," *Opt. Eng.*, vol. 45, no. 6, p. 063601, 2006.

[113] J. Zhong and H. Zeng, "Multiscale windowed Fourier transform for phase extraction of fringe patterns," *Appl. Opt.*, vol. 46, no. 14, pp. 2670–2675, 2007.

[114] S. Ozder, O. Kocahan, E. Coskun, and H. Goktas, "Optical phase distribution evaluation by using an s-transform," *Opt. Lett.*, vol. 32, no. 6, pp. 591–593, 2007.

[115] Y. Hu, J. Xi, J. Chicharo, E. Li, and Z. Yang, "Discrete cosine transform-based shift estimation for fringe pattern profilometry using a generalized analysis model," *Appl. Opt.*, vol. 45, no. 25, pp. 6560–6567, 2006.

[116] M. A. Sutton, W. Zhao, S. R. McNeill, H. W. Schreier, and Y. J. Chao, "Development and assessment of a single-image fringe projection method for dynamic applications," *Experimental Mechanics*, vol. 41, no. 3, pp. 205–217, 2001.

[117] K. Okada, E. Yokoyama, and H. Miike, "Interference fringe pattern analysis using inverse cosine function," *Electronics and Communications in Japan, Part II: Electronics*, vol. 90, no. 1, pp. 61–73, 2007.

[118] Y. Tangy, W. Chen, X. Su, and L. Xiang, "Neural network applied to reconstruction of complex objects based on fringe projection," *Opt. Commun.*, vol. 278, no. 2, pp. 274–278, 2007.

[119] T. Yan, C. Wen-Jing, Z. Qiang, S. Xian-Yu, and X. Li-Qun, "Bp neural network applied to 3d object measurement based on fringe pattern projection," *Optik*, vol. 120, no. 7, pp. 347–350, 2009.

[120] R. Rodríguez-Vera and M. Servín, "Phase locked loop profilometry," *Opt. Laser Technol.*, vol. 26, no. 6, pp. 393–398, 1994.

[121] J. Kozlowski and G. Serra, "New modified phase locked loop method for fringe pattern demodulation," *Opt. Eng.*, vol. 36, no. 7, pp. 2025–2030, 1997.

[122] D. Ganotra, J. Joseph, and K. Singh, "Second- and first-order phase-locked loops in fringe profilometry and application of neural networks for phase-to-depth conversion," *Opt. Commun.*, vol. 217, no. 1-6, pp. 85–96, 2003.

[123] M. A. Gdeisat, D. R. Burton, and M. J. Lalor, "Fringe-pattern demodulation using an iterative linear digital phase locked loop algorithm," *Opt. Laser Eng.*, vol. 43, no. 7, pp. 31–39, 2005.

[124] J. Villa and M. Servin, "Robust profilometer for the measurement of 3-d object shapes based on a regularized phase tracker," *Opt. Laser Eng.*, vol. 31, no. 4, pp. 279–288, 1999.

[125] J. Villa, M. Servin, and L. Castillo, "Profilometry for the measurement of 3-d object shapes based on regularized filters," *Opt. Commun.*, vol. 161, no. 1-3, pp. 13–18, 1999.

[126] S. Toyooka and Y. Iwaasa, "Automatic profilometry of 3-d diffuse objects by spatial phase detection," *Appl. Opt.*, vol. 25, no. 10, pp. 1630–1633, 1986.

[127] M. R. Sajan, C. J. Tay, H. M. Shang, and A. Asundi, "Improved spatial phase detection for profilometry using a tdi imager," *Opt. Commun.*, vol. 150, no. 1-6, pp. 66–70, 1998.

[128] F. Berryman, P. Pynsent, and J. Cubillo, "A theoretical comparison of three fringe analysis methods for determining the three-dimensional shape of an object in the presence of noise," *Opt. Laser Eng.*, vol. 39, no. 1, pp. 35–50, 2003.

[129] V. Srinivasan, H. C. Liu, and M. Halioua, "Automated phase-measuring profilometry of 3-d diffuse objects." *Appl. Opt.*, vol. 23, no. 18, pp. 3105–3108, 1984.

[130] M. Chang and D. Wan, "On-line automated phase-measuring profilometry," *Opt. Laser Eng.*, vol. 15, no. 2, pp. 127–139, 1991.

[131] X. Su, W. Zhou, G. von Bally, and D. Vukicevic, "Automated phase-measuring profilometry using defocused projection of a ronchi grating," *Opt. Commun.*, vol. 94, no. 6, pp. 561–573, 1992.

[132] X. Su, G. von Bally, and D. Vukicevic, "Phase-stepping grating profilometry: utilization of intensity modulation analysis in complex objects evaluation," *Opt. Commun.*, vol. 98, no. 1-3, pp. 141–150, 1993.

[133] X. F. Meng, X. Peng, L. Z. Cai, A. M. Li, J. P. Guo, and Y. R. Wang, "Wavefront reconstruction and three-dimensional shape measurement by two-step dc-term-suppressed phase-shifted intensities," *Opt. Lett.*, vol. 34, no. 8, pp. 1210–1212, 2009.

[134] L. Huang, Q. Kemao, B. Pan, and A. K. Asundi, "Comparison of Fourier transform, windowed Fourier transform, and wavelet transform methods for phase extraction from a single fringe pattern in fringe projection profilometry," *Opt. Laser Eng.*, vol. 48, no. 2, pp. 141–148, 2010.

[135] J. M. B. Dias and J. M. N. Leitao, "The zpim algorithm: A method for interferometric image reconstruction in sar/sas," *IEEE Trans. Image Processing*, vol. 11, no. 4, pp. 408–422, 2002.

[136] H. O. Saldner and J. M. Huntley, "Temporal phase unwrapping: Application to surface profiling of discontinuous objects," *Appl. Opt.*, vol. 36, no. 13, pp. 2770–2775, 1997.

[137] S. Su and X. Lian, "Phase unwrapping algorithm based on fringe frequency analysis in Fourier-transform profilometry," *Opt. Eng.*, vol. 40, no. 4, pp. 637–643, 2001.

[138] C. Yu and Q. Peng, "A correlation-based phase unwrapping method for Fourier-transform profilometry," *Opt. Laser Eng.*, vol. 45, no. 6, pp. 730–736, 2007.

[139] B. Jose, V. Katkovnik, J. Astola, and K. Egiazarian, "Absolute phase estimation: adaptive local denoising and global unwrapping," *Appl. Opt.*, vol. 47, no. 29, pp. 5358–5369, 2008.

[140] T. R. Judge and P. J. Bryanston-Cross, "A review of phase unwrapping techniques in fringe analysis," *Opt. Laser Eng.*, vol. 21, no. 4, pp. 199–239, 1994.

[141] J. M. Huntley and C. R. Coggrave, "Progress in phase unwrapping," *Proc. SPIE*, vol. 3407, pp. 86–93, 1998.

[142] D. C. Ghiglia and M. D. Pritt, *Two-Dimensional Phase Unwrapping: Theory, Algorithms, and Software.* Wiley-Interscience, 1998.

[143] X. Su and W. Chen, "Reliability-guided phase unwrapping algorithm: A review," *Opt. Laser Eng.*, vol. 42, no. 3, pp. 245–261, 2004.

[144] E. Zappa and G. Busca, "Comparison of eight unwrapping algorithms applied to Fourier-transform profilometry," *Opt. Laser Eng.*, vol. 46, no. 2, pp. 106–116, 2008.

[145] S. S. Gorthi and P. Rastogi, "Fringe projection techniques: Whither we are?" *Opt. Laser Eng.*, vol. 48, no. 2, pp. 133–140, 2010.

[146] K. . Kim, K. . Kim, and C. . Shim, "A study on the measurement of plastic zone and crack growth length at the crack tip under cyclic loading using espi system," *Structural Engineering and Mechanics*, vol. 15, no. 3, pp. 367–378, 2003.

[147] B. Guelorget, M. François, C. Vial-Edwards, G. Montay, L. Daniel, and J. Lu, "Strain rate measurement by electronic speckle pattern interferometry: A new look at the strain localization onset," *Materials Science and Engineering A*, vol. 415, no. 1-2, pp. 234–241, 2006.

[148] G. Montay, M. Francois, M. Tourneix, B. Guelorget, C. Vial-Edwards, and I. Lira, "Strain and strain rate measurement during the bulge test by electronic speckle pattern interferometry," *Journal of Materials Processing Technology*, vol. 184, no. 1-3, pp. 428–435, 2007.

[149] F. Labbe, "Strain-rate measurements by electronic speckle-pattern interferometry (ESPI)," *Opt. Laser Eng.*, vol. 45, no. 8, pp. 827–833, 2007.

[150] G. B. Broggiato, L. Casarotto, Z. Del Prete, and D. Maccarrone, "Full-field strain rate measurement by white-light speckle image correlation," *Strain*, vol. 45, no. 4, pp. 364–372, 2009.

Curriculum Vitae

SAI SIVA GORTHI

S/o G. Sri Rama Sastry
Dammapeta
Khammam Dist.
Andhra Pradesh
INDIA
Email: saisiva.gorthi@gmail.com
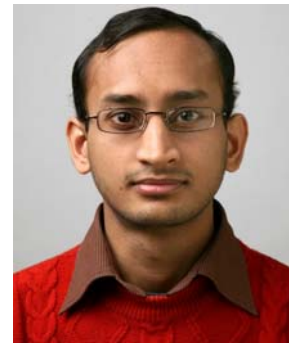
Education

2007-2010 : Ph.D., Swiss Federal Institute of Technology, Lausanne,
SWITZERLAND

2003-2005 : Master of Science in Optical Metrology, Department of Instrumentation,
Indian Institute of Science, Bangalore, INDIA

1999-2003 : B.Tech. in Electronics and Communications Engineering from Jawaharlal
Nehru Technological University, Hyderabad, INDIA

Professional Experience

2007-2010 : Research Assistant, Swiss Federal Institute of Technology

2006-2007 : R & D Engineer, IBM Bangalore, India

2003-2006 : Research Assistant, Indian Institute of Science

Areas of Interest

- Fringe analysis
- 3-D shape measurements
- Time evolution studies
- Applied signal processing
- Interferometry
- Non-destructive testing

Professional Activities

- ❖ Served as a Guest Editor for a special issue on Fringe Projection Techniques in Optics and Lasers in Engineering.

- ❖ Serving as a reviewer for the following journals: Optics Letters, Applied Optics, Journal of Optics A: Pure and Applied Optics, Measurement Science and Technology, Optics and Lasers in Engineering, and Optical Engineering.

Guest Editorials

❖ Gorthi, S. S. and Rastogi, P. "Fringe projection techniques: Whither we are?" *Optics and Lasers in Engiering*, 48(2):133-140, 2010.

Publications in Peer-Reviewed Journals

1. Gorthi, S. S., Rajshekhar, G. and Rastogi, P. "Strain estimation in digital holographic interferometry using piecewise polynomial phase approximation based method" *Optics Express*, 18(2):560-565, 2010.

2. Gorthi, S. S., Rajshekhar, G. and Rastogi, P. "Three-dimensional shape measurement using high-order instantaneous moments based fringe projection method" *Optics and Laser Technology,* 43(1):40-44, 2011.

3. Gorthi, S. S., Rajshekhar, G. and Rastogi, P. "Investigations to realize a computationally efficient implementation of the high-order instantaneous moments based fringe analysis method" *Optical Engineering,* 49(065802): 1-4, 2010.

4. Rajshekhar, G., Gorthi, S. S. and P. Rastogi, "Estimation of the phase derivative using an adaptive window spectrogram," *Journal of Optical Society of America: A*, 27(1):69-75, 2010.

5. Gorthi, S. S. and Rastogi, P. "Phase estimation in digital holographic interferometry using cubic phase function based method" *Journal of Modern Optics,* 57(7):595-600, 2010.

6. Rajshekhar, G., Gorthi, S. S. and Rastogi, P. "Estimation of displacement derivatives in digital holographic interferometry using a two-dimensional space-frequency distribution" *Optics Express,* 18(17):18041-18046, 2010.

7. Gorthi, S. S. and Rastogi, P. "Simultaneous measurement of displacement strain and curvature in digital holographic interferometry using high- orderinstantaneous moments" *Optics Express*, 17(20):17784-91, 2009.

8. Rajshekhar, G., Gorthi, S. S. and Rastogi, P. "An adaptive window Wigner-Ville distribution based method to estimate phase derivative from optical fringes" *Optics Letters*, 34(20):3151-3153, 2009.

9. Gorthi, S. S. and Rastogi, P. "Improved high-order ambiguity function method for the estimation of phase from interferometric fringes" *Optics Letters*, 34(17):2575-2577, 2009.

10. Gorthi, S. S. and Rastogi, P. "Windowed high-order ambiguity function method for fringe analysis" *Review of Scientific Instruments,* 80(7):073109, 2009.

11. Rajshekhar, G., Gorthi, S. S. and Rastogi, P. "Strain, curvature and twist measurements in digital holographic interferometry using pseudo Wigner-Ville distribution based method" *Review of Scientific Instruments*, 80(093107), 2009.

12. Gorthi, S. S. and Rastogi, P. "Estimation of phase derivatives using discrete chirp-Fourier transform based method" *Optics Letters*, 34(16):2396-2398, 2009.

13. Rajshekhar, G., Gorthi, S. S. and Rastogi, P. "Polynomial Wigner-Ville distribution based method for direct phase derivative estimation from optical fringes" *Journal of Optics A: Pure and Applied Optics,* 11(125402), 2009.

14. Gorthi, S. S. and Rastogi, P. "Discrete chirp Fourier transform based analysis of reconstructed interference fields in digital holographic interferometry" *Journal of Modern Optics*, 56(12):1317-1322, 2009.

15. Gorthi, S. S. and Rastogi, P. "Analysis of reconstructed interference fields in digital holographic interferometry using polynomial phase transform" *Measurement Science and Technology,* 20(075307):1-6, 2009.

16. Gorthi, S. S. and Rastogi, P. "Piecewise polynomial phase approximation approach for the analysis of reconstructed interference fields in digital holographic interferometry" *Journal of Optics A: Pure and Applied Optics,* 11(065405):1-6, 2009.

17. Gorthi, S. S. and Rastogi, P. "Numerical analysis of fringe patterns recorded in holographic interferometry using high-order ambiguity function" *Journal of Modern Optics,* 56(8):949-954, 2009.

Publications in Peer-Reviewed Journals (submitted)

1. Rajshekhar, G., Gorthi, S. S. and Rastogi, P. "Estimation of dynamically varying displacement derivatives using fringe projection technique" *Applied Optics,* 2010.

Publications in Conferences

1. Gorthi, S. S., Rajshekhar, G. and Rastogi, P. "Estimation of phase in fringe projection technique using high-order instantaneous moments based method" International Conference on Advanced Phase Measurement Methods in Optics and Imaging, *AIP Proc.* 1236, 359-362, 2010.

2. Rajshekhar, G., Gorthi, S. S. and Rastogi, P. "Comparative analysis of various single-tone frequency estimation techniques in high-order instantaneous moments based phase estimation method" International Conference on Advanced Phase Measurement Methods in Optics and Imaging, *AIP Proc.* 1236, 355-358, 2010.

3. Ambrosini, D., Gorthi, S. S. and Rastogi, P. "Enhancing accuracy and sensitivity of temperature gradient measurements in DOE Schardin Schlieren #2 using windowed Fourier transform method" International Conference on Advanced Phase Measurement Methods in Optics and Imaging, *AIP Proc.* 1236, 124-128, 2010.

4. Yagnik, J., Gorthi, S. S., K. R. R., and Lolla, K. R., "3-D shape extraction of human face in presence of facial hair: A profilometric approach" In IEEE Region 10 Annual International Conference, *TENCON*, 2007.

5. Nukala, S. S., Gorthi, S. S. and Lolla, K. R., "Novel composite coded pattern for small angle measurement using imaging method" In Novel Optical Systems Design and Optimization IX., *Proc. of SPIE* vol.6289, 2006.

6. Gorthi, S. S., and Lolla, K. R., "Novel single-shot structured light technique for accurate, reliable and dense 3-D shape measurement" *Proc. Of the International Conference on Optics & Optoelectronics*, Dehradun, India, Dec 2005.

7. Gorthi, S. S., and Lolla, K. R., "New phase unwrapping strategy for rapid and dense 3-D data acquisition in structured light approach" *Proc. of the 5th Int. Workshop on Automatic Processing of Fringe Patterns*, Stuttgart, Germany, pp. 242-246, Sept 2005.

8. Gorthi, S. S., and Lolla, K. R., "Wavelet transform analysis of truncated fringe patterns in 3-D surface profilometry" Optical Measurement Systems for Industrial Inspection IV, *Proc. of SPIE* vol.5856 (SPIE, Bellingham, WA, 2005) 265-273.

9. Gorthi, S. S., and Lolla, K. R., "New approach for simple and rapid shape measurement of objects with surface discontinuities" Optical Measurement Systems for Industrial Inspection IV, *Proc. of SPIE,* vol.5856 (SPIE, Bellingham, WA, 2005) pp. 184-194.

10. Gorthi, S. S. and Lolla, K. R., "A new approach for phase unwrapping in profiling objects with surface discontinuitie" *Proc. of the 7th International Conference on Optoelectronics, Fiber Optics and Photonics* (Paper: DIS P20), Dec 2004, Cochin, India.

Personal Details

Date of Birth : Aug. 05th, 1981.
Citizenship   : Indian.

References

Prof. Pramod Rastogi
Applied Computing and Mechanics Laboratory (IMAC),
EPFL, 1015 Lausanne, Switzerland. Email: pramod.rastogi@epfl.ch

Prof. Dario Ambrosini
DIMEG, University of L'Aquila, Via G. Gronchi 18, 67100 L'Aquila, Italy,
Email: dario.ambrosini@ing.univaq.it

Prof. L. Kameswara Rao,
Department of Instrumentation,
Indian Institute of Science, Bangalore, India,
Email: lkrao@isu.iisc.ernet.in